Spin and Charge transport in Dirac Materials

Alexander Hoyer

EPFL
ÉCOLE POLYTECHNIQUE
FÉDÉRALE DE LAUSANNE

Success consists of going from failure
to failure
without loss of enthusiasm
Winston Churchill

To my family **K. F. A. M. . . .**

Acknowledgements

This thesis is the condensate of four years of struggle, ecstasy, headache and hard work. I am grateful for all the people that join on the way and help me to understand and master this little part of science.

First of all I would like to thank my thesis advisor Prof. Klaus Kern for the possibility to work on such a physical subject as a chemist. Thank you for giving me the opportunity, for including me in your group and for keeping up this special environment with all those fine people.

Secondly I want to thank my day to day supervisor Dr. Marko Burghard for his guidance and confidence in me. Thank you for your patience with me and my topic and for bringing Dr. Christian Cervetti in my life.

I want to thank Dr. Eberhard Ulrich Stützel, Dr. Eva Carmen Peters and Dr. Thomas Dufaux for giving me such a nice and kind introduction to the institute and all the processes.

For all the help with setting up the big refrigerator in 5 C 11 I would like to thank a bunch of people. Dr. Markus Ternes and Dr. Jürgen Weis for discussing everything concerning measurement instrumentation with me and introducing me to the basics of electrical engineering. I would like to thank Martin Siemers, Rafail Chaikevitch, Peter Gorzellik and Holger Neuhauß for helping me with all the soldering and electrical construction work. Dr. Markus Etzkorn and Dr. Stephan Rauschenbach I thank for discussing all the issues concerning UHV and cryogenics in the last four years.

The whole setting up could not have been down without Wolfgang Stiepany, Peter Andler and Marko Memmler with their meticulous plans, craftsmanship and construction knowledge. Everything was made so much easier with the quality and precision of the people working at the *mechanical*, *fine mechanical* and *electrical* workshop. They make this place so much more precious.

I like to thank the staff of the clean room Thomas Reindl, Ulrike Waizmann, Achim Güth and Marion Hagel for all the support in the device fabrication and processing, extra time slots and facility improvements. Not to mentions those numerous samples which needed to be glue bonded.

I am grateful for the experimental help of Dr. Hagen Klauk and Dr. Ute Zschieschang and their time to discuss everything with me.

Acknowledgements

For their expertise with the electron beam I would like to thank Viola Duppel and Bernhard Fenk. They gave me the proof that I contacted the right stuff.

Thank you Dr. Christian Cervetti for struggling with me through all that *spining*. For all those discussions we had, your input and output for my never ending questions.

For introducing me to topological insulators and CVD growth I thank Dr. Pascal Gehring. For the continuing fruitful cooperation on that topic I would like to thank Kristina Andreeva Vaklinova.

I thank my office mates Dr. Ivan Pentegov and Sabine Abb for the pleasant and uncomplicated time. For improving the language of this thesis and the time on the balcony I would like to thank Dr. Thomas White.

To all the actual and former members of the *molecular electronics/ quantum materials group* who created this fruitful environment.

At last to the people who paved the way from all the beginning. To my family who supported me with their patience, time and love. To Kathrin for all the encouragement in the toughest moments, for your love and the three children. To my children for enlightening the dark moments, cheering me up and for showing me infantile enthusiasm.

Stuttgart, 12. Januar 2016   Alexander Hoyer

Abstract

The digitalization of our world is proceeding with every new technical product placed on the market. By making them smarter, e.g. linking them together and equipping them with sensors, a vast mass of data is collected. Processing and storing this information is particularly challenging as it should be done in real time and, ideally with a handheld device. This requires logic devices to be very fast, low on power consumption and rather small. The latter requirement is leading towards a transition from the classical physics domain to a domain where quantum effects like tunneling and interference start to dominate the behavior. Thus for miniaturization to continue, it is necessary to adapt new techniques that work in the quantum regime.

One promising approach to achieve all of this is to exploit the spin degree of freedom an electron possesses, opening up the field of spin electronics (spintronics). As first principle operation of such devices has been demonstrated with silicon, new materials may possess attributes that better suite the requirements of spintronics devices. Graphene, a two dimensional carbon allotrope, is such a candidate as it shows low spin orbit coupling, which theoretical allows high spin life times to be achieved. Furthermore the 2 D nature of graphene allows to control and tailor the electronic and spin properties by external means such as proximity and chemical functionalization.

On this basis low temperature magnetotransport measurements are performed to explore the effect of functionalization of graphene with 4-nitrophenyl diazonium tetrafluoroborate[1] within this thesis. Basic measurements in Hall bar geometry show an introduction of disorder due to the functionalization. Additional weak localization, a quantum effect that gives information on the phase coherence length of the electrons, is observed after functionalization and used to explore the electronic properties of the tailored graphene.

To address the spin properties of graphene its spin bath needs to be controlled and manipulated. This is done within this thesis by all electrical means and requires the fabrication of spin valve structures on graphene. Two strategies to inject spin polarized currents into graphene are pursued within this framework. First spin valve

---

[1]CAS: 456-27-9

Abstract

measurements on functionalized graphene are promising regarding the manipulation of spin properties.

The generation of the spin polarized currents is still a big issue. Traditionally, ferromagnets are used as leads to fulfill this task. Latest studies show that *topological insulators* (TI), a new class of materials, could be better suited to fulfill this task as they give rise to fully spin polarized currents. Conceptually these materials possess a band gap that is crossed by spin polarized bands. Crystals of nanometer size of Tin(II)telluride, a potential TI, are grown in a PVD process and electrically contacted to look for fingerprints of these unusual states. Charge and spin transport experiments show the presence of two types of charge carriers and a high intrinsic p-doping.

Finally, a new ^{3}He system is set up within this thesis and a concept for low noise measurements is implemented that integrates a home build signal generation and amplification stage.

Key words: Graphene, Topological Insulators, Spintronics

Zusammenfassung

Die Digitalisierung unserer Welt schreitet mit großen Schritten voran. Unsere Umgebung wird durch miteinander kommunizierende Geräte, die mit einer Vielzahl von Sensoren ausgestattet sind, intelligent und soll so unser Leben vereinfachen. Die Menge an Daten, welche gesammelt und verarbeitet werden müssen, wächst im selben Atemzug. Dabei sollte die Auswertung der Daten in Echtzeit erfolgen - möglichst in einem mobilen Gerät. Die Anforderungen an die logischen Bauteile sind dabei extrem hinsichtlich Taktfrequenz, Leistungsaufnahme und Platzverbrauch. Kleinstbauteile stoßen dabei an die Grenzen der klassischen Physik und zeigen zunehmend Eigenschaften aus der Quantenwelt. Dies verlangt nach neuen Konzepten in der Miniaturisierung der Bauteile.

Ein hoffnungsvoller Ansatz ist das Nutzen der Spin-Eigenschaften des Elektrons für logische Operationen. Dies öffnet das Feld der Spin-Elektronik (Spintronik). Erste prinzipielle Funktionen wurden auf Siliziumbasis demonstriert. Nichtsdestotrotz können andere Materialien bessere Eigenschaften besitzen, welche für spintronische Bauelemente von Vorteil wären. Graphen, ein zwei-dimensionales Gitter aus Kohlenstoff, könnte eine Alternative darstellen. Aufgrund seiner schwachen Spin-Bahn-Wechselwirkung sollten Spinzustände von hoher Lebensdauer realisierbar sein. Darüber hinaus bietet die Zwei-Dimensionalität einzigartige Möglichkeiten, die elektronischen Eigenschaften von außen durch z.B. chemische Funktionalisierung zu steuern.

Im Rahmen dieser Arbeit wird die Funktionalisierung von Graphen mit 4-Nitrophenyldiazoniumtetrafluoroborate hinsichtlich der Auswirkung auf elektronische Eigenschaften untersucht. Dafür werden Graphen-Flocken in der Hall-Struktur kontaktiert und bei tiefen Temperaturen unter dem Einfluss eines externen magnetischen Feldes untersucht. Die Funktionalisierung bringt Unordnung in das System und lässt den Quanteneffekt der schwachen Lokalisierung erscheinen. Dieser Effekt lässt Rückschlüsse auf die Phasenkohärenz der Elektronen zu und wird daher näher untersucht.

Um Spineigenschaften untersuchen zu können, muss das Spin-Bad manipuliert werden können. In der vorliegenden Arbeit wird dies rein elektrisch realisiert und erfordert die Fabrikation von Spin-Ventilen mit Graphen. Es werden zwei Strategien

Zusammenfassung

für die Injektionen von Spin polarisierten Strömen in Graphen untersucht. Erste Messungen an nachträglich funktionalisierten Strukturen lassen hoffen, dass die Spineigenschaften positiv beeinflusst werden können.

Ein großes Problem stellt immer noch das Generieren von Spin-polarisierten elektrischen Strömen dar. Typischerweise wird ein unpolarisierter Strom mit Hilfe eines Ferromagneten polarisiert. Kürzlich erschienene Publikationen lassen hoffen, dass topologische Isolatoren (TI), eine neuartige Materialklasse, höhere Polarisierungsgrade erreichen können. Konzeptuell besitzen diese Materialien eine Bandlücke, sind daher Halbleiter oder im Extremfall Isolatoren, welche durch Spin-polarisierte Zustände überbrückt werden. Winzige Kristalle von Zinn(II)tellurid, ein potentieller TI, werden in einen PVD Prozess gewachsen und elektrisch kontaktiert um nach Hinweisen für diese Zustände zu suchen. Ladungs- und Spintransport-Experimente zeigen, dass das Material hoch p-dotiert ist und zwei Ladungsträger vorhanden sind.

Um diese Experimente durchführen zu können, wird im Rahmen dieser Arbeit ein ^{3}He-Kryostat aufgebaut. Ein Konzept zur rauscharmen Messung wird implementiert.

Contents

Contents

List of Figures

List of Tables

Introduction

Since the invention of the transistor in 1948[2] immense effort has been directed toward the further development of the concept. While the first transistor utilized germanium as channel material and was of the size of a hand, the first commercialized silicon transistors already had the size of a stamp [3]. The idea on miniaturization of device components arose with the development of *integrated circuits*, resulting in a doubling of the number of transistors per unit area nearly every one-and-a-half years[3] [4]. Today's microelectronic industry is able to produce $1.3 \cdot 10^9$ transistors on an area of $82 \, \mathrm{mm}^2$ of silicon with a gate pitch of $70 \, \mathrm{nm}$[4] [5].
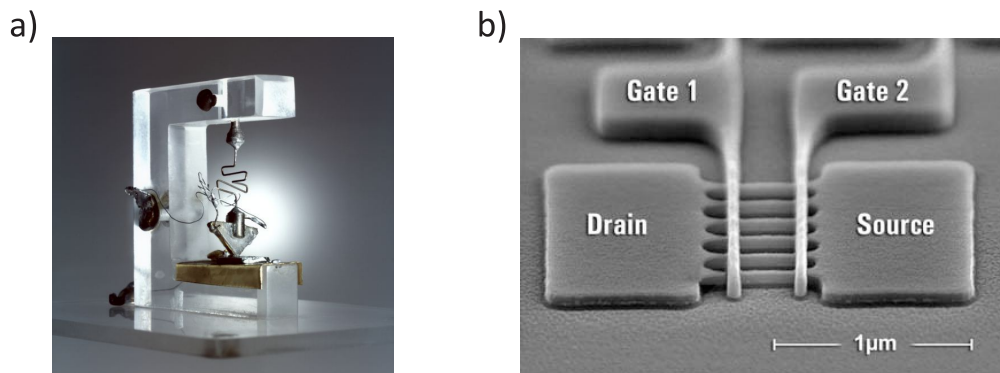
Fig. *1: a) Replica of the first electronic transistor developed at Bell Labs. b) Demonstration device of a state-of-the-art FinFET (a double gate transistor). Images taken from [1, 2].*

Transistors of these size dimensions start to show quantum effects, including interference and tunneling, which limit their performance. To increase the performance and reduce the power consumption, alternative materials to silicon and different device concepts need to be explored. One alternative concept relies upon the intrinsic spin of electrons, which can be regarded as the internal magnetic moment of the electron. It allows for two distinct configurations, i.e., up and down. The emerging field of spin electronics (spintronics) aims to exploit this small magnetic moment to perform logic

---

[2]Nobel prize 1956 to W. B. Shockley, J. Bardeen and W. H. Brattain
[3]This is commonly known as Moore's law
[4]Intel trigate with 14 nm production techniques

operations. This idea dates back to 1856, when the anisotropic magnetoresistance (AMR), as entanglement of charge transport and magnetization, was first observed [6]. Thus far, the magnetic moment of the electron has only been used to read and store information rather than process it. While the first commercial magnetic tape from IBM in 1952 had a storage density of 100 bits per inch squared (bpi), state-of-the-art hard disks reach 1.32 Tbit/in^2 [7, 8], reflecting a similar miniaturization trend as for the transistors. However, the technological breakthrough for the spin transistor proposed in 1990 by DATTA and DAS has not yet occurred [9].

The main obstacle in spintronics is to achieve efficient spin injection from a spin filter into a nonmagnetic material. Spin filters are able to transform charge currents into spin currents due to their unique band structure comprising spin-split bands at the Fermi energy. Most often, ferromagnetic materials are used to this end. However, several theoretical works have shown that efficient spin injection is difficult to attain with Ohmic contacts because the electrical conductivities of the two materials do not match, leading to a depolarization of the spin current at the interface [10]. Tunneling contacts have been proposed and successfully implemented as a solution to this problem [11].

With the experimental realization of graphene in 2004, massless Dirac particles became easily accessible to experimental physics [12]. This opened the opportunity to study relativistic effects in condensed matter systems up to room temperature, a task which had been restricted to high energy physics before. While conventional materials have a parabolic energy dispersion, Dirac materials have a linear dispersion around the Fermi energy. Depending on the properties of the linear bands, Dirac semimetals and topological insulators can be distinguished. The latter have a bulk band gap accompanied by a band inversion due to strong spin-orbit coupling (SOC), which leads to topologically protected surface states within the bulk band gap.

The rise of graphene, a Dirac semimetal, has stimulated spintronic research in various respects. As graphene has a relatively low electrical conductivity normal to the basal plane, and it is only atom thick, it represents a promising replacement for oxide barriers in standard tunneling devices. The latter typically have a high resistance area product (RAP), which results in a high power consumption in a real device. This could be lowered by two orders of magnitude with the aid of graphene [14].

Furthermore to its low spin-orbit coupling (SOC), graphene is predicted to have long spin lifetimes (τ_s), which in combination with its high carrier mobility (μ) should give rise to long spin diffusion lengths (λ_s) [15]. The reason why mobilities as high as $3 \cdot 10^6 \, \text{m}^2 / \text{V s}$ can be realized with graphene is intimately related to its band structure [16]. Specifically, graphene's linear bands at the Fermi energy lead to massless Dirac particles. Thus, graphene constitutes a valuable alternative platform for spin transport. However, toward practical application, it faces the same obstacles as

$E_F \sim k^2$ $E_F \sim k$ $E_F \sim k$
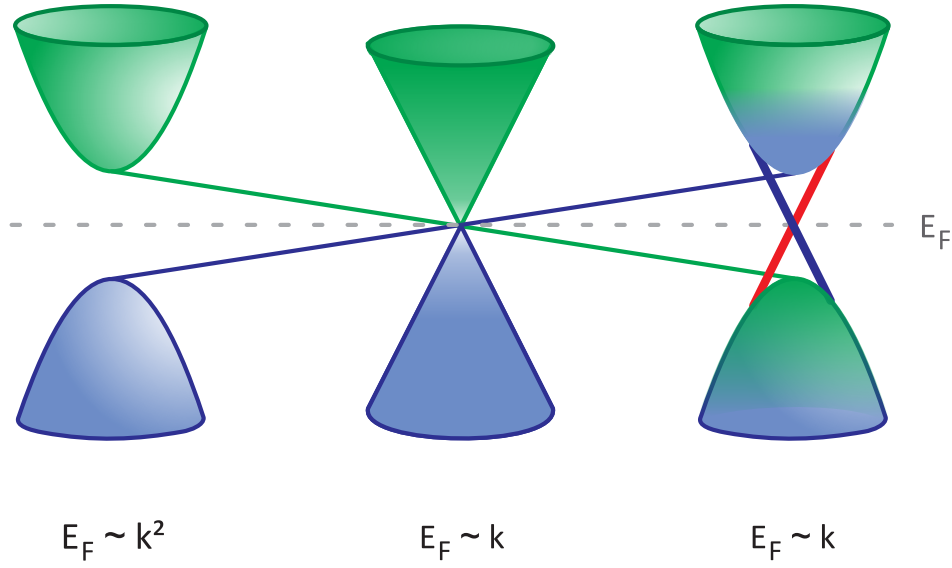
Fig. 2: *Electronic band structure evolution from a trivial semiconductor with parabolic bands (left) to a topological insulator (right). Touching bands with linear band dispersion define a Dirac semimetal (middle). In the topological insulator, the strong SOC causes band inversion along with the opening of a bulk bandgap that is crossed by spin-polarized surface states. Adapted from [13].*

silicon concerning spin injection. It was only during the past few years that significant progress has been made along this direction [17]. The initial value of $\lambda_s = 1.5\,\mu$m reported in 2007 could recently be improved to $24\,\mu$m [18]. The prediction and realization of magnetic order in chemically functionalized graphene [19–21] together with the possibility to enhance the SOC in graphene [22] opens up the opportunity to generate, manipulate and detect spin currents in one-and-the-same nanostructured material, such that the number of delicate material interfaces can be reduced.

Shortly after the experimental realization of graphene in 2004, the concept of topological insulators (TIs) was introduced in 2005, and their existence experimentally verified first for mercury telluride (HgTe) [23, 24]. Since then, the class of TI has gained 34 confirmed members and is still expanding as the concept is refined [25]. Similar to graphene, TIs possess linearly dispersing bands that give rise to massless Dirac fermions. Ideally, TIs are insulating in the bulk and conducting on the surface, so that they can be compared to a piece of marble wrapped in aluminum foil. These so-called surface states lie within the band gap and their existence depends on which material they are in contact with. The main hurdle for using TIs as electronic device components is that their Fermi level lies either in the valence or conduction band, which results in a high bulk conductivity which often dominates over the surface state-associated conductivity. As a consequence, significant effort has been made to reduce the bulk doping of the TIs, for instance through improved growth techniques to minimize the concentration of anion deficiencies [26]. In TIs, the spin of the electron is

locked to the carrier momentum (direction of motion), which renders them promising as spin generators in spintronics [27]. The spin-momentum locking ensures that, when an electron moves from A to B, its spin points in one direction, whereas upon moving backward from B to A it points in opposite direction. It originates from the strong SOC in these materials, which represents a key requirement for the formation of topological states [28].

This thesis deals with the charge and spin transport properties of two different types of quantum materials, namely chemically functionalized graphene and tin(II)telluride (SnTe). The latter compound is a topological crystalline insulator, a special type of TI which has only recently been identified. The first chapter introduces the basic physical and material properties of Dirac materials, followed by the properties of the two investigated materials. The second chapter describes the charge transport phenomena that are relevant for the understanding of the experimental work. Details of sample preparation and characterization together with a description of the electrical measurement setup are provided in chapter three. The fourth chapter summarizes the results obtained for covalently functionalized graphene. It starts with basic charge transport experiments, followed by contrasting the spin transport behavior of the pristine and functionalized graphene. The last chapter describes the charge and spin transport experiments performed on SnTe nanostructures.

1 Dirac Materials

1.1 What are Dirac Materials

Condensed matter can be classified according to different aspects. One is the symmetry of the atomic arrangement in the crystal. This classification is based upon real space and hence cannot account for physical properties like electrical and thermal conductance, which may significantly differ between the seven crystal symmetry classes. Alternatively, materials can be classified with respect to the electronic material properties, which requires a transition from real space to k-space. Depending on the band structure and filling, two major material classes emerge, namely insulators and metals [29].
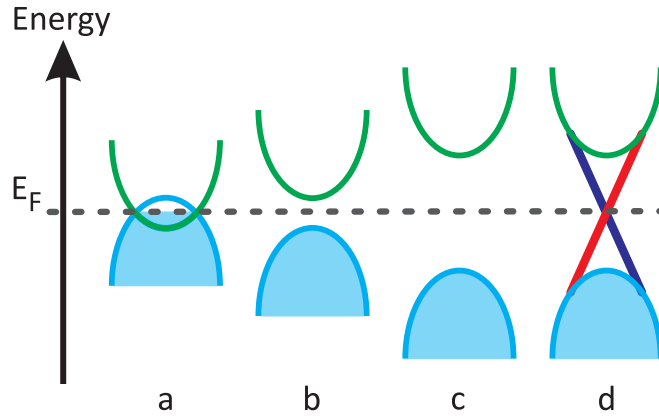
Fig. 1.1: *Schematic representation of the band structure and typical Fermi level position for different material classes: a) metal, b) intrinsic semiconductor, c) insulator, and d) Dirac material, where the crossing point of the two linear bands is at the Fermi level (E_F).*

Within the framework of Fermi liquid theory, the system is classified according to its zero energy or low-energy excitations ($E_{\text{exc.}} \propto k_B T$), which also determine the response to external perturbations. Only partially filled bands or overlapping bands at the Fermi level (Figure 1.1 a) are characteristic for metals. In this case, only little energy is required to lift an electron from an occupied to an unoccupied state. Accordingly, metals exhibit a broad low or zero energy excitation spectrum. In contrast, insulators have a completely filled lower band, which is well separated in energy from the unoccupied band, as depicted in Figure 1.1 b-c). At zero temperature, excitations appear above the energy of the band gap. In small gap insulators (semiconductors), electronic band transitions can be thermally excited to a significant extent ($k_B T \propto E_{gap}$) [30–32]. The Fermi level position in semiconductors can be shifted upon doping, which allows for excitations from donor states near the valence band to the valence band (n-doping) e.g. from the conduction band to acceptor states near the conduction band (p-doping).

Metals and semiconductors in a nonrelativistic condensed matter setting have in

common that their electron states close to the Fermi level can be described by the Schrödinger Hamiltonian

$$H_s = \frac{-\hbar^2 \mathbf{p}^2}{2m^*}.$$

The electrons thus behave as massive fermions with parabolic energy dispersion $E \propto k^2$ and the mass defined as

$$\frac{\partial^2 E}{\partial k^2} = \frac{\hbar^2}{m^*}.$$

Semiconductors can have bands with different curvatures in k-space, corresponding to different effective charge carrier masses. This leads to light and heavy holes (or electrons with different masses m^*), which can be detected in electrical transport measurements [33].

In certain materials, crossing of electronic bands can occur (see Fig. 1.1 f). Some of these nodal points have the unique property that the band dispersion is linear and cannot be described by the Schrödinger Hamiltonian anymore. Instead, these linear bands, at least in the vicinity of the nodal point, are well described by the Dirac Hamiltonian

$$H_D = c\boldsymbol{\sigma} \cdot \mathbf{p} \tag{1.1}$$

and satisfy the relativistic dispersion relation

$$E^2 = \mathbf{p}^2 c^2 + m^2 c^4.$$

The mass is coupeld to $\boldsymbol{\sigma}_z$ and for condensed matter systems the speed of light c in equation 1.4 is replaced by the Fermi velocity v_F

$$H_D = v_\mathrm{F} \hbar \boldsymbol{\sigma} \cdot \mathbf{k},$$

where $\mathbf{k}$ is defined with respect to the Dirac point. The existence of these gapless nodal points with linear band dispersion is intimately connected to protection by either time reversal symmetry or lattice/crystal symmetry. The kinetic energy ($c \cdot |\mathbf{p}|$) of the particles associated with the nodal points largely exceeds the rest mass ($m \cdot c^2$) and the particles are said to be in the ultrarelativistic limit. This implies that the chirality

$$\Lambda = \frac{\sigma \mathbf{p}}{|\mathbf{p}|},$$

with values of ± 1, becomes a conserved quantity. As a consequence one degree of freedom becomes locked to the momentum of the particle.

Although Dirac fermions in different Dirac materials share common features, they display various flavors. The Dirac particles in the materials relevant for the present thesis are of two-dimensional (2 D) nature. In the case of graphene, the 2 D character originates from the physical dimensionality of the material. In the second type of material, three-dimensional (3 D) topological insulators (TIs), the Dirac particles occur on the surface and thus are also 2 D. A common feature of the 2 D Dirac particles in graphene and 3 D TIs is their zero mass, imparting high carrier velocity. Likewise, in both cases they exhibit the already mentioned (pseudo) spin-momentum locking, which renders them chiral. These two features have direct consequences for the charge transport behavior. In particular, the time reversal symmetry suppresses backscattering, as any scattering event must not only change the momentum of the particle but also the locked spin degree. This reduces the phase space of possible scattering trajectories. A further common feature is the quantization (N) of the Landau levels[1] (LL). While Schrödinger fermions follow

$$E(N) = \hbar \omega_c \left(N + \frac{1}{2} \right) \quad = \frac{e\hbar B}{m_c c} \left(N + \frac{1}{2} \right),$$

which corresponds to a linear energy level spacing in dependence of the B-Field (B), Dirac fermions follow

$$E_{\pm}(N) = \sqrt{\frac{2e\hbar v_F^2 B}{c} N},$$

representing a square root dependency with respect to B. The resulting larger spacing of the levels makes them observable even at room temperature [25, 31, 34].

The Berry phase, a geometrical phase explained further below, is also different for Schrödinger and Dirac fermions. While parabolic energy dispersions (Schrödinger fermions) are characterized by a Berry phase of 0, linear energy dispersions (Dirac fermions) have a phase of π. As a consequence, in the latter case time-reversed scattering paths destructively interfere with each other, giving rise to weak anti-localization (WAL) instead of weak localization (WL) [25].

On this basis, a new material class based on the low energy excitations spectrum is defined. In the following section, the family of topological (crystalline) insulators will be introduced, along with Tin(II)telluride (SnTe) as prototype example. Graphene, as a member of the class of Dirac semimetals, will be described afterwards.

---

[1]Landau levels will be explained in section 2.2.4

1.2 Topological (Crystalline) Insulators

Insulators are characterized by the presence of an energy gap between the conduction and valence bands in the entire Brillouin zone [29].

In a simple picture, a TI behaves like an insulator wrapped in a metal foil. In this ideal case they are insulating in the bulk and possess conducting states on the surface [25, 31]. To explain the origin of the conducting surface states, two relevant factors are to be considered. The first one is strong spin-orbit coupling (SOC), which leads to band inversion of the conduction and valence bands. The second one relates to the interface to the surrounding. Specifically, upon bringing an insulator with band inversion in contact with a normal insulator (even, for like vacuum), the change of topology induces a gap-closing and -reopening, thereby creating the Dirac surface states [25, 31]. The physical-mathematical operation defining a topologically non-
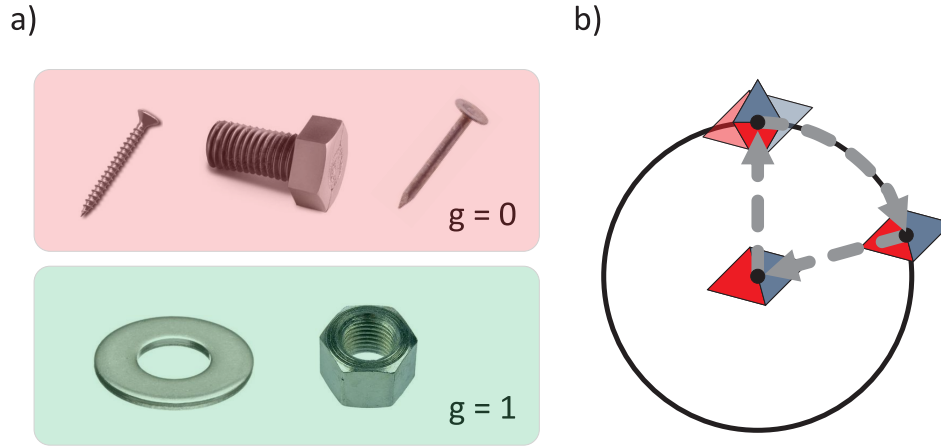
Fig. *1.2: a) Screws and nuts belong to two different topology classes. The surface of a screw can be smoothly transformed into a nail. In order to transform into a nut, however, the surface of the screw has to be pierced. b) The Berry phase can be illustrated by moving a compass needle on a sector of a circle. Parallel transport in this case means that the orientation of the needle with respect to the translation vector is fixed. After moving in this manner back to the starting point, the needle has rotated by a certain angle [35].*

trivial phase is the transformation of the Hamiltonian. If the Hamiltonian of insulator A can be adiabatically deformed to describe insulator B without closing the gap, these systems are said to be equivalent. An analogy is a screw that by smoothing of its surface can be transformed into a nail without breaking the surface (Fig. 1.2 a). By contrast, transforming a screw into a nut requires breaking the surface in order to create a hole. The concept behind such transformations can be used to define topological classes. Examples are surfaces with no hole, like screws or nails, and surfaces with

one hole, such as nuts and washers. Each class is characterized by an invariant $\nu \in \mathbb{Z}_2 \, [0, 1]$ [36, 37].

For topological and normal insulators, the classification is based upon the band structure. Group theory helps to distinguish different bands and assigns them specific notations [38]. For PbTe, a trivial insulator, the conduction (valance) band is a L_6^- (L_6^+) state, as shown in Figure 1.4. For topological (crystalline) insulators, like SnTe, the band inversion due to strong SOC yields L_6^+ (L_6^-) states.

1.2.1 Berry phase, Chern numbers and time reversal symmetry

In order to establish the connection between Chern numbers and TIs, the concepts of the Berry phase and time reversal symmetry of the Brillouin zone needs to be explained.

The Berry phase describes the phase picked up by electronic states while moving on a closed loop. In quantum mechanics this is described by a Hamiltonian that has a time dependent parameter $\mathbf{R}(t)$ (like an electric or magnetic field). The Schrödinger equation for the system in the n-th state assumes the form

$$H\left[\mathbf{R}(t)\right] | n, \mathbf{R}(t)\rangle = E_n\left[\mathbf{R}(t)\right] | n, \mathbf{R}(t)\rangle.$$

If the parameter $\mathbf{R}$ slowly and adiabatically changes from $\mathbf{R}_0(t = 0)$ along a closed path C to return to its original position $\mathbf{R}(T) = \mathbf{R}_0$, the phase picked up by the quantum state n is

$$\gamma_n = \oint_C i\langle n, \mathbf{R} | \nabla_R | n, \mathbf{R}\rangle d\mathbf{R}. \tag{1.2}$$

For 2 D massless Dirac fermions with the Fermi velocity v_{F}, the Dirac equation has the form

$$E\psi(\mathbf{r}) = \hbar v_{\mathrm{F}}\boldsymbol{\sigma} \cdot \mathbf{k}\psi(\mathbf{r}) = -i\hbar v_{\mathrm{F}}\boldsymbol{\sigma} \cdot \nabla\psi(\mathbf{r}) = -i\hbar v_{\mathrm{F}}\boldsymbol{\sigma} \cdot \nabla u(\mathbf{k})e^{i\mathbf{k}\cdot\mathbf{r}}$$

with the eigenfunctions written in terms of Bloch functions. The energy eigenvalues are

$$E_{\pm} = \pm \hbar v_{\mathrm{F}}\mathbf{k}.$$

If the wave vector $\mathbf{k}$ orbits around the origin on a closed path C counterclockwise equation 1.2 becomes

$$\gamma_n = \oint_C i\langle u(\mathbf{k}) | \nabla_k | u(\mathbf{k})\rangle d\mathbf{k} = \pi$$

and the picked-up phase is π [25].

In a more illustrative way, the Berry phase can be explained by moving a compass needle around a sector on a sphere [39]. In case of parallel transport the needle moves on the sector while keeping its orientation locked to the translation vector as depicted in Figure 1.2 b). After passing through all corners and returning back to the initial point, the needle will be rotated with respect to its initial state [35]. The Berry phase is connected to a topological invariant (Chern number) $n \in \mathbb{Z}$ by the integral

$$n = \sum_{m=1}^{N} \frac{1}{2\pi} \int \nabla \times \underbrace{i \langle u_m(\mathbf{k}) \,|\, \nabla_k \,|\, u_m(\mathbf{k}) \rangle}_{\mathcal{A}_m} d^2\mathbf{k}. \tag{1.3}$$

This integral represents the total Berry flux ($\nabla \times \mathcal{A}_m$) in the Brillouin zone and has to be summed over all occupied bands m to give the total Chern number. As the number n cannot change, when the Hamiltonian varies smoothly, it is a topology invariant of the system. Coming back to the nuts and screws analogy, equation 1.3 can be understood as a mapping from two to three dimensions. The 2 D surface of nuts and screws as 3 D objects can be classified by the number of holes g. For screws with no hole, $g = 0$, while for nuts with one hole, $g = 1$. Owing to the different g values, these two objects cannot be transformed smoothly into each other. Here, g assumes a similar role to the Chern number n for the Brillouin zone.

GAUSS and BONNET demonstrated that the integral of a Gaussian curvature over a closed surface is a topological invariant with quantized values and is related to g. Equation 1.3 describes an integral of a related curvature [37].

The connection to time reversal symmetry $\mathcal{T}$ becomes clear since it can be expressed by an anti-unitary operator

$$\mathcal{T} = exp\left(\frac{i\pi S_y}{\hbar}\right)\mathbf{K}$$

with the spin operator S_y and the complex conjugation $\mathbf{K}$. If time reversal symmetry $\mathcal{T}$ holds for a system this has intriguing consequences. Specifically, the momentum $\mathbf{p}$ and the spin state $\mathbf{S}$ of the system change sign under time inversion

$$\mathcal{T}\mathbf{p}\mathcal{T}^{-1} = -\mathbf{p},$$

whereas the position operator $\mathbf{x}$ remains unaffected. The result of applying $\mathcal{T}$ twice on the system depends on the system's spin state. A zero spin system returns to its original position, while for finite spin systems

$$\mathcal{T}^2 = (-1)^{2S},$$

where S is the spin state. For a Hamiltonian preserving time reversal symmetry

$$\mathcal{T} H(\mathbf{k}, S)\mathcal{T} = H(-\mathbf{k}, -S)$$

is satisfied. Hence there exist states at $\mathbf{k}$ and $-\mathbf{k}$ that have the same energy for such systems.

The Brillouin zone contains eight points $\mathbf{G}$ that satisfy the condition

$$\mathcal{T} H(\mathbf{G})\mathcal{T} = H(\mathbf{G}),$$

thus $\mathbf{k} = -\mathbf{k}$. These points are called time reversal invariant momentum (TRIM) points and originate from the periodicity of the Brillouin zone. If the system in addition has inversion symmetry, the parity $\xi_m(\mathbf{G}_i)$ of the occupied bands at the eight TRIM points defines

$$\delta(\mathbf{G}_i) = \prod_n \xi_{2n}(\mathbf{G}_i),$$

the so-called parity invariants. For systems with time reversal symmetry, there are four combinations of $\delta(\mathbf{G}_i)$, which remain robust and give rise to four invariants $(\nu_0; \nu_1, \nu_2, \nu_3 \in \mathbb{Z}_2)$. These invariants specify if a system is trivial (0;000) or not. The invariant ν_0 is given by

$$(-1)^{\nu_0} = \prod_i^8 \delta(G_i),$$

and defines if the system is a weak or strong TI ($\nu_0 = 0/1$ for $\sum_i \nu_i \neq 0$). In this context, strong refers to the robustness of the surface states with respect to perturbation and disorder. The other three invariants are determined by the projection of the parity of the eight TRIM points along one direction as depicted in Figure 1.3 [25, 37, 40–43].

To date, all experimentally confirmed TIs are inverted narrow bandgap semiconductors. The bandgap inversion occurs an odd number of times at the TRIM points. With exception of the Bi-Sb alloy system, all TIs have only one band inversion at the Γ-point in the Brillouin zone.

The concept of symmetry protected Hamiltonians has been extended from time reversal symmetry to crystal symmetries. Here, mirror symmetry $\mathcal{M}$ has a similar effect as time reversal symmetry [41].

Mirror or reflection symmetry involves spatial inversion P and a C_2-rotation around the axis orthogonal to the reflection plane. The effect of $\mathcal{M}$ on the electrons in systems with SOC is a rotation of the spatial coordinates and spin. Similar to $\mathcal{T}$, for fermions $\mathcal{M}^2 = -1$ with the eigenvalues $\pm i$. The Bloch states of a system with mirror symmetry
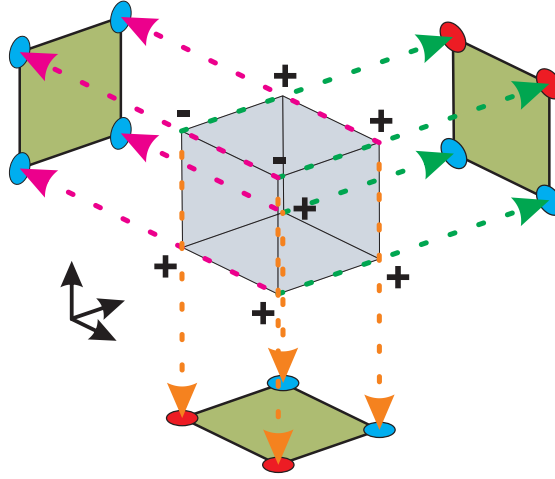
Fig. *1.3: Eight time reversal invariant momentum (TRIM) points with their specified parity lead to the phase (0;0,0,1). The value of sign(δ_i) is indicated by $\pm$. The projection along the three easy axes onto the orthogonal plane defines the invariants ν_i ($0 < i < 4$) [41].*

can be chosen such that they are eigenstates of $\mathcal{M}$. This establishes two classes with eigenvalues $\eta = \pm i$ and a corresponding Chern number N_η. A non-zero mirror Chern number

$$N_M = \frac{N_{+i} - N_{-i}}{2}$$

defines membership to the class of topological crystalline insulators. Here, the topological nature stems from the crystal symmetries [36, 44].

For both TIs as well as topological crystalline insulators, the degree of freedom locked to momentum is the electron spin. Such locking generates spin-polarized surface currents with strongly suppressed backscattering.

1.2.2 Tin(II)telluride as a Topological Crystalline Insulator

Tin(II)telluride is a well-known narrow gap IV-VI semiconductor. It exists in two crystalline forms. The NaCl structure is the thermodynamically stable modification at room temperature with a fundamental band gap of 0.3 eV (12 K) at the four equivalent L points in the face-centered-cubic Brillouin zone [44].

Early studies were motivated by the possibility to incorporate Lead ($Pb_{1-X}Sn_xTe$) or Germanium ($Ge_{1-X}Sn_xTe$) and thereby to tune the band gap. Both Lead(II)telluride and Germanium(II)telluride form a solid solution with Tin(II)telluride, where the metal atoms are randomly distributed over the sub-lattice. Their narrow band gap makes these materials interesting as the active component of infrared detectors and infrared diode lasers operating in the $10 - 15\,\mu$m wavelength range [45, 46].

The investigation of PbSnTe alloys of varying composition revealed a closing and
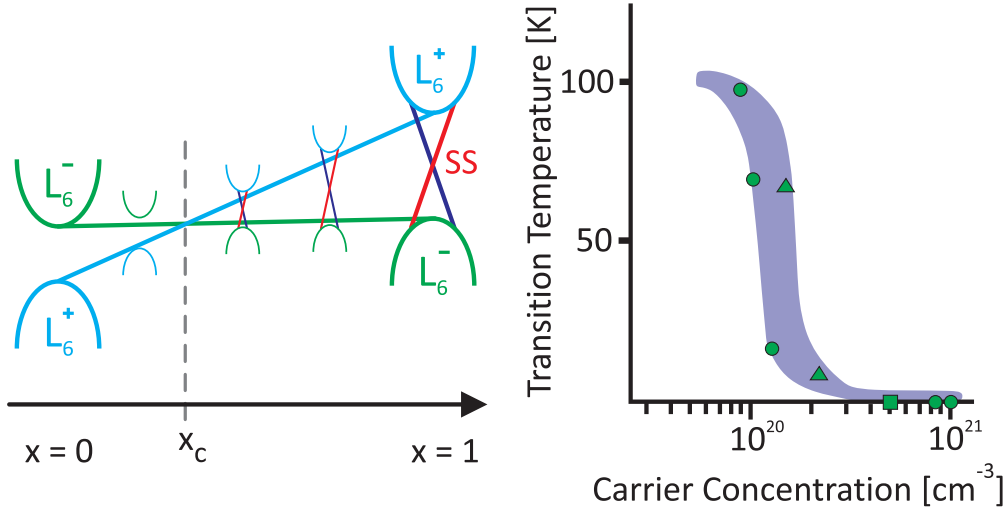
Fig. *1.4: left panel) Schematic representation of the valence and conduction band change upon alloying Tin to Lead telluride ($Pb_{1-X}Sn_xTe$). The phase transition from a trivial ($x = 0$) to a topological crystalline insulator ($x = 1$) occurs upon band inversion at $x_c \sim 0.25$ [47, 48]. right panel) The phase transition temperature of the SnTe crystal structure from cubic to rhombic strongly depends on the carrier concentration (Adapted from [49]).*

re-opening of the band gap, which is accompanied by a band inversion. The pure PbTe phase ($x = 0$ in $Pb_{1-x}Sn_xTe$) has a bandgap of 0.18 eV (12 K). Upon alloying Tin, the valence and conduction bands move closer to each other until they touch at the L-point for $x_c \sim 0.25$. At x_c the L_6^- and L_6^+ bands invert and the bandgap is reopened upon increasing x. This band inversion arises from different energy shifts of the L_6^- and L_6^+ bands due to the different relativistic corrections introduced by the different masses of Lead and Tin[2]. When going from PbTe to SnTe the L_6^- shifts upwards by 0.23 eV and the L_6^+ by 0.99 eV. In both of these compounds, the band labeled with L_6^+ is predominantly composed of the cation orbitals, while L_6^- results from the anions. Thus, the conduction band of SnTe has an unusual anionic character [36, 45, 46, 50, 51].

The band gap closing and re-opening together with the band inversion has been documented at the end of the 1970s. In 1987, three Russian scientists theoretically proposed that the band inversion is accompanied with the formation of Weyl-bands that connect the L_6^- and L_6^+ bands [47]. However, it took until 2012 to define the new material class of *Topological Crystalline Insulators* based on the formalism of TIs. In this framework, it became apparent that SnTe hosts an even number of Dirac-cones on the {001}, {111} and {110} crystal surfaces. This characteristic constitutes the main difference to $\mathbb{Z}_2$ TIs that host an odd number of Dirac points. The presence of Dirac particles has been experimentally proven in $Pb_{1-X}Sn_xTe$ by angle resolved

---

[2] $m_a(Pb) = 207.2$ u, $m_a(Sn) = 118.7$ u

photoemission (ARPES) measurements [48, 52]. Thus far, however, no signature of the surface states could be gained by electrical transport measurements.

As mentioned above, SnTe comes in two crystal structures. In the high temperature sodium chloride structure every atom is a center of inversion, such that the excitation of Raman modes is forbidden due to symmetry. The situation is different for the low temperature phase of SnTe which has a rhombohedral structure. The lifted inversion symmetry renders the three optical vibration modes Raman and IR active [53]. A transverse optical (TO) phonon appears at $\approx 21\,\text{cm}^{-1}$ at ^{4}He-temperature. This mode disappears above the phase transition temperature [54]. Likewise, the temperature dependent peak at $\approx 130\,\text{cm}^{-1}$ has been used for monitoring the phase transition [53]. The dependence of transition temperature on stoichiometry and charge carrier concentration in Figure 1.4 has been determined from neutron diffraction and Raman experiments.

The inverse scaling of phase transition temperature with charge carrier concentration has been attributed to a stabilization of the crystal phase by the charge carriers. For high carrier concentrations (high Sn-vacancy concentration) the phase transition can even be entirely suppressed. The highest phase transition temperature reported for SnTe is 98 K [49]. Raman spectroscopy has been successfully used to investigate the chemical composition of nanostructured TIs like $\text{Bi}_2\text{Te}_{2-x}\text{Se}_x$ [55]. In contrast, the lack of Raman signals for the NaCl-structure of SnTe prevents this possibility. The only other compositional analysis tool suitable for such nanostructures would be energy dispersive X-ray (EDX) spectroscopy. However, this technique allows for a rough estimation of the chemical composition which is a major drawback.

1.3 Graphene

Carbon exists in the form of different allotropes ranging from the 3 D crystalline diamond to the 2 D layered graphene, the 1D carbon nanotubes and finally the 0 D fullerenes. Among these, the planar allotrope graphene is the most recently discovered one. In all of the allotropes with dimensionality smaller than three, the carbon atoms are arranged into a 2 D lattice. In the case of graphene and carbon nanotubes, this is a hexagonal lattice comprised of two types of atoms per unit cell, denoted as A (red) and B (green) in Figure 1.5 a). Thus, the lattice consists of two interpenetrating triangular lattices formed by the A and B atoms, respectively [56].

1.3.1 Electronic properties

The 2 D lattice arrangement can only be realized by mixing the orbitals of each individual carbon atom. The six electrons of a carbon atom are distributed between five orbitals (1 s, 2 s, 2 p_x, 2 p_y, and 2 p_z). Two electrons are bound in the inner shell (1 s) and do not participate in the "chemistry". The 2 s orbital combines with the 2 p_x and 2 p_y orbitals to form three sp^2 hybrid orbitals. Each of the latter partakes in the formation of an in-plane, covalent σ-bond. The resulting three σ-bonds are highly directional with a carbon-carbon distance of 1.42 Å [56, 57]. The strength of these bonds is responsible for the high mechanical stability and strength of the carbon lattice [58]. As depicted in Figure 1.5, the electronic bands formed by the σ-bonds are well separated by approximately 12 eV at the Γ-Point in reciprocal space. Correspondingly, the σ-bands are not relevant for the major optical and electronic properties of carbon nanostructures.

The remaining electron is located in the 2 p_z orbital, which overlaps with neighboring
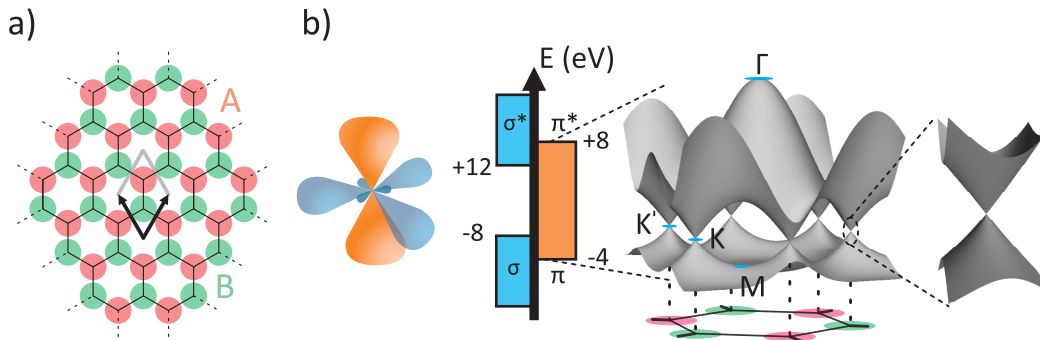
Fig. 1.5: a) Honeycomb lattice of graphene, with the two interpenetrating lattices colored in red (A) and green (B). The unit cell is depicted. b) sp^2-hybridized carbon atom. The sp^2-orbitals in blue form the well-separated σ bonding/antibonding bands. The p_z-orbital in orange forms the π-bands, which close the gap. Numbers correspond to band edges in eV. The π-bands can be described by equation 1.4 and touch at the K and K' points in reciprocal space. In vicinity of these points, the π-bands show linear dispersion. Adapted from [56, 57].

$2p_z$-orbitals to form delocalized π-bonds. These are orthogonal to the σ-bonds and the overlap of π and σ bonds is zero due to their orthogonal character. The bonding and anti-bonding π-bands form the conduction and valence band of graphene, respectively, and allow for a full description of the low energy excitations [57, 59].

The essence of the π-bands can be described by a simple tight binding Hamiltonian, as has been reported already in 1947 by WALLACE [59]. In second quantization it takes the form

$$\hat{H} = -t \sum_{\langle i,j \rangle, \sigma} \left(a^\dagger b + c.c \right) - t' \sum_{\langle\langle i,j \rangle\rangle, \sigma} \left(a^\dagger a + b^\dagger b + c.c. \right).$$

and involves electron hopping to nearest neighbors ($t \approx 2.8\,\text{eV}$), i.e., from A- to B-site atoms, as well as next-nearest t' ($0.02t < t' < 0.2t$) neighbor hopping from A- to A-site atoms [56].

The energy bands are obtained as

$$E_\pm(\mathbf{k}) = \pm t \sqrt{6\cos\left(\sqrt{3}k_y a\right) + 12\cos\left(\frac{\sqrt{3}}{2}k_y a\right)\cos\left(\frac{3}{2}k_x a\right)}$$
$$- t' 2\cos\left(\sqrt{3}k_y a\right) + 4\cos\left(\frac{\sqrt{3}}{2}k_y a\right)\cos\left(\frac{3}{2}k_x a\right), \tag{1.4}$$

where the plus (minus) holds for the valence (conduction) band. Equation 1.4 reveals that finite values of t' introduce an asymmetry to the valence and conduction band. In Figure 1.5, equation 1.4 is plotted for $t = 2.8\,\text{eV}$ and $t' = 0.1t$.

At the invariant points K and K' in reciprocal space, the conduction and valence bands touch each other rendering graphene a semi metal. Close to these points, the band dispersion is linear and accordingly, the particles of the Dirac cone can be described by the 2 D equivalent of equation 1.1, i.e.,

$$H_D = c\boldsymbol{\sigma} \cdot \mathbf{p} + m \cdot c^2 \cdot \sigma_z \tag{1.5}$$
$$\text{with} \quad \sigma = \left(\sigma_x, \sigma_y\right).$$

The Dirac nodes in graphene are protected by time-reversal symmetry

$$\mathcal{T} H(\mathbf{k}) \mathcal{T}^{-1} = H(-\mathbf{k})$$

$$\tag{1.6}$$

and inversion symmetry originating from lattice symmetry

$$\mathcal{P} H(\mathbf{k}) \mathcal{P}^{-1} = H(-\mathbf{k})$$
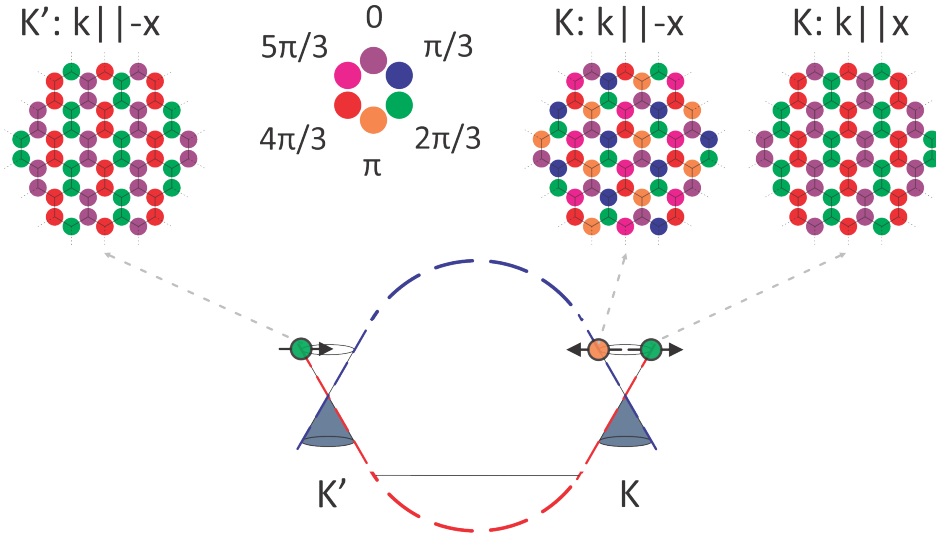
Fig. *1.6: Phase distribution of the electronic wavefunction at the K and K′ point for the bonding and antibonding case. Phase is coded according to the color scale. Bonding (red) and anti-bonding (blue) contributions to the nodal points give rise to the phase differences. Adapted from [63].*

$$\mathcal{P} h_z(\mathbf{k})\mathcal{P}^{-1} = -h_z(-\mathbf{k}),$$

which maps sublattice A on B and changes the momentum $\mathbf{k}$ to $-\mathbf{k}$. Both operations applied together require $h_z(\mathbf{k}) = 0$, such that the mass term in equation 1.5 vanishes [60].

As described in section 1.1, the spin-momentum-locking has different flavors. In graphene, it is implemented by the pseudospin. The pseudospin is described by a two component vector containing the phase factor of the electronic wavefunction on each sublattice. It points either in the direction of $\mathbf{k}$ or is antiparallel to it [61]. As a consequence, the character of the wavefunction (bonding or anti-bonding) changes with the carrier propagation direction. As sketched in Figure 1.6, the Dirac cones at K and $K′$ are antisymmetric with respect to the phase of the electronic wavefunction (red and blue line). This means that a state with $\mathbf{k}\| - x$ at the K-point has antibonding character, while at $K′$ it has bonding character. In this manner, a handiness is introduced that differs for the two cones (left vs right-handed). The weak backscattering in graphene is a direct consequence of pseudospin conservation [32, 61–63].

1.3.2 Electronic transport properties

For non-doped (pristine) graphene at $T \approx 0$, the Fermi level (E_F) lies at the intersection of the Dirac cones, classifying graphene as a semimetal. Doping shifts E_F into either the conduction or valence band, giving rise to an ambipolar charge transport behavior, as illustrated in Figure 1.7.
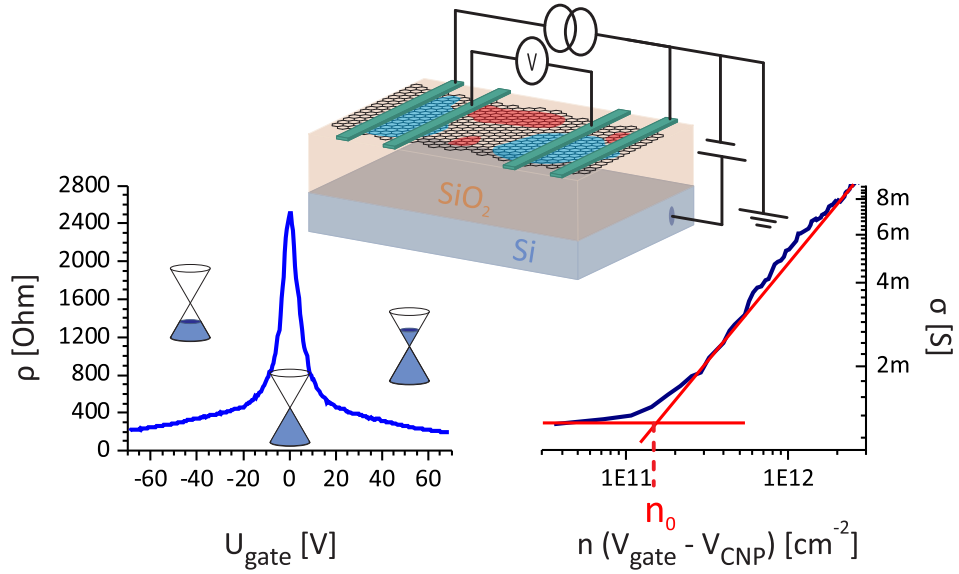
Fig. *1.7: The inset in the middle is a schematic depiction of a graphene field-effect to measure the ambipolar transport properties by applying a gate potential to the underlying substrate (back-gating) (left panel). Doping by adsorbates and/or inhomogeneous substrate surface charges create electron-hole puddles (depicted in red and blue) which decrease the resistivity at the charge neutrality point (CNP). The decrease of the resistivity at the CNP is accompanied with a residual charge carrier density n_0. The right panel illustrates the procedure to extract this quantity from a double logarithmic plot.*

Doping can be realized by chemical means or electrostatically in a field-effect configuration. For graphene on a Si/SiO$_2$ substrate, a gate voltage (V_{gate}) can be applied, where upon the conductivity

$$\sigma = \frac{1}{\rho} \quad = \frac{w}{l \cdot R} \quad = e \cdot n \cdot \mu \quad = \underbrace{\frac{\epsilon_0 \epsilon_r}{ed}}_{\alpha} \left(V_{\text{gate}} - V_{CNP}\right) \cdot e \cdot \mu \tag{1.7}$$

of the sheet is modulated via the charge carrier density n [12].

The modulation of charge carrier density can be described by a simple capacitor model. The induced carrier density depends linearly on the applied voltage with a proportionality factor α. This factor includes the thickness of the oxide ($d = 300\,\text{nm}$) and the electric permittivity of the gate insulator ϵ_r (SiO$_2$) = 3.9. For the Si/SiO$_2$ (300 nm thickness) substrates used in this thesis, the gate coupling factor is $\approx 7 \cdot 10^{14}\,\text{m}^{-2}\text{V}^{-1}$, which permits tuning of the carrier density up to $\approx \pm 5 \cdot 10^{16}\,\text{m}^{-2}$ before the oxide breaks down. Higher carrier concentrations can be achieved by polymer electrolyte gating.

As the charge carriers are depleted by the field effect, the resistance of graphene increases. When the Fermi level reaches the Dirac point, the resistance should

in principle become infinitely large, because essentially all carriers have vanished. However, doping from device fabrication residues on top of the graphene and/or trapped charges in the gate oxide induce charges on the local scale, resulting in positive and negative charge puddles over the whole flake [64]. As a result there remains a finite conductivity due to charge transport between these puddles. Unintentional doping by surface contaminations leads to a shift of the CNP away from zero gate voltage ($U_g = 0$ V). This can be taken into account by expanding equation 1.7 to

$$\sigma = 0\mu \cdot e \cdot \sqrt{n_0^2 + \alpha \left(V_g - V_{CNP}\right)^2}$$

which includes the residual charge carrier concentration n_0. The latter quantity can be extracted from a $\ln(\sigma)$ [S] vs $\ln\left(\alpha|V_{\text{gate}} - V_{CNP}|\right)$ [cm^{-2}] plot. As can be seen from Figure 1.7, with decreasing carrier concentration the conductivity decreases approximately linearly until it reaches a plateau. The intercept of the two straight lines yields n_0 [65]. The determined charge carrier density then provides access to E_F of the graphene [66]. In vicinity of the K and K' points E_F is given by

$$E_F(\mathbf{k}) = \hbar v_F |\mathbf{k}| = \sqrt{\pi n}\,\hbar v_F. \tag{1.8}$$

1.3.3 Raman modes

Raman spectroscopy is a powerful, non-destructive technique to evaluate material properties by probing the vibrational modes of the lattice. In the case of graphene, Raman spectroscopy can provide valuable information like the number of layers [67, 68], defect concentration and grain size [69], as well as the doping level and thus an estimate of the charge carrier concentration [70]. This has established Raman spectroscopy as a major characterization technique for graphene devices. Moreover, with the aid of a confocal Raman microscope it is possible to detect spatial variations of the Raman modes of graphene sheets[3].

Vibrational modes are distinguished by the type of movement of the carbon atoms with respect to their nearest neighbors. The acoustic (optical) mode comprises the coherent (out-of-phase) movement of the carbon atoms. In addition longitudinal (L) and transverse (T) modes depending on the relative orientation between the phonon wave vector and the atomic displacement direction can be distinguished [29]. Since the unit cell of graphene contains two atoms, six phonon dispersion bands emerge consisting of three acoustic (A) and three optical (O) modes [71]. For both types, there exists one out-of-plane mode, while the four remaining ones are in-plane modes (i).

---

[3]For $\lambda_{exc} = 534$ nm, the probed area is on the order of $\pi \cdot \left(\frac{\lambda_{exc}}{2}\right)^2 \approx 0.8 \, \mu\text{m}^2$.
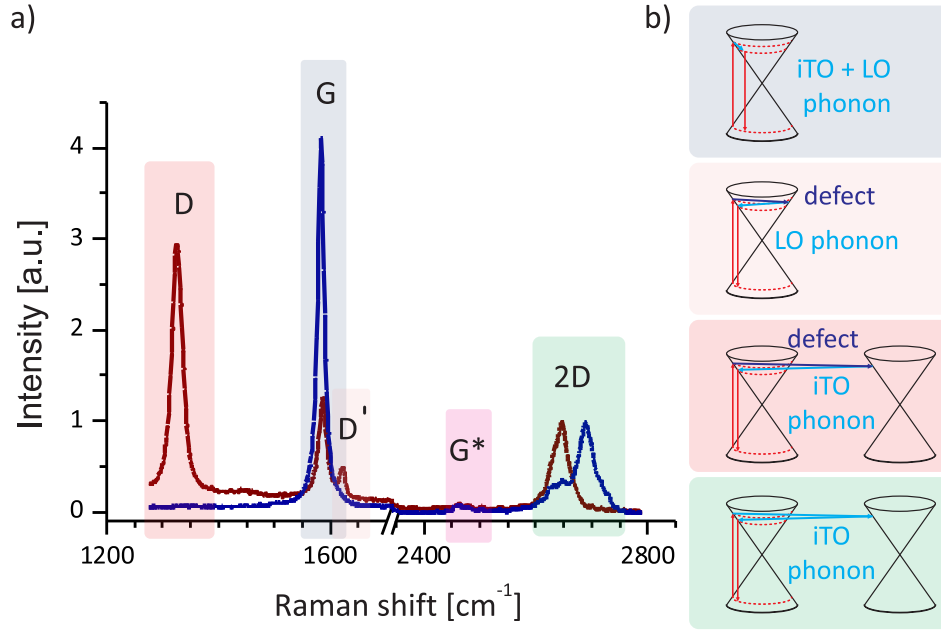
Fig. *1.8: a) Raman spectrum of defective graphene (red) and HOPG (blue) taken with an excitation wavelength of 633 nm. (b) The four main scattering mechanisms that give rise to the G-mode, the D′-mode, the D-mode and 2D-mode, respectively (from top to bottom) [71].*

The six vibrational modes give rise to four characteristic peaks (G, D, D′, 2D) with high intensity, as exemplified by the Raman spectrum in Figure 1.8 a).

- The G peak ($\approx 1580\,\mathrm{cm^{-1}}$), which originates from first order scattering, is associated with two degenerated iTO and LO phonon modes. In the molecular picture, this mode involves stretching of the carbon-carbon sp^2-bonds. The G peak position is sensitive to doping of the sheet. Both n- and p-type doping result in an upward shift of the peak position [67, 70, 71].

- The D-peak ($\approx 1320 - 1350\,\mathrm{cm^{-1}}$) and D′-peak ($\approx 1620\,\mathrm{cm^{-1}}$) are fourth order double resonance processes, where the wave vector of the phonon is coupled to the electronic band structure. As this requires energy conservation in all steps, the energy of these modes depends on the laser excitation energy. As depicted in Figure 1.8, the overall process starts with the creation of an electron-hole-pair by the incoming photon, which is followed by two scattering events and finally electron-hole recombination with the creation of a photon. The two scattering events are inelastic electron-phonon scattering with the creation of a phonon and subsequent elastic scattering with a defect. As both processes need a defect, they can be used to probe the crystal quality and defect density. Depending on the momentum transferred this way, inter-valley (D-peak) and intra-valley (D′-peak) scattering can be observed [67, 71]. While the D-peak is only sensitive to the amount of defects, the D′-peak is influenced by the defect nature [72].
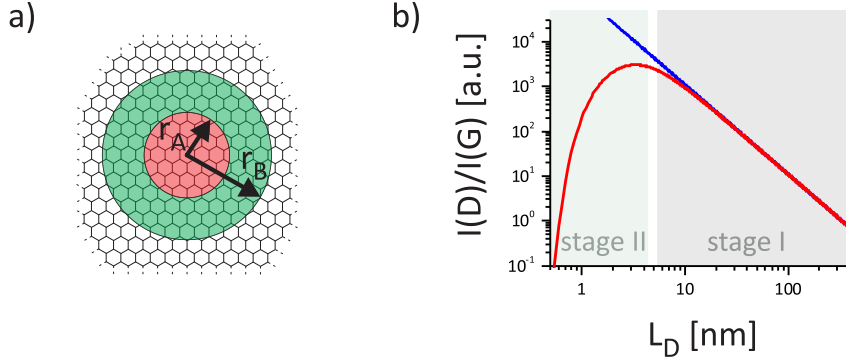
Fig. *1.9: a) Illustration of the two radii r_A and r_B, which are defined from the defective site [67]. b) Plot of eq. 1.11 for $C_A = 160$, $r_A = 3.1$ nm and $r_B = 1$ nm. The two stages (I+II) are highlighted. The blue line is a plot using eq. 1.9 which is valid for stage I.*

- The 2 D peak ($\approx 2700\,\mathrm{cm}^{-1}$) is the second order of the D-peak. Here, scattering by a defect is replaced by the creation of a second iTO phonon with opposite momentum to the first, such that the 2 D-peak is also present in pristine graphene. The shape and position of the peak can be used to evaluate the number of layers. For monolayer graphene it consists of a single Lorentzian, while for a few layers the peak is composed of several Lorentzians [67, 68].
- The G^* ($\approx 2450\,\mathrm{cm}^{-1}$), similar to the 2 D-peak, is based upon an inter-valley scattering mechanism, although its intensity is much lower. In contrast to the 2 D-peak, it involves one iTO and one LA-phonon [67].
- Higher harmonic peaks like $2\,D'$ ($\approx 3250\,\mathrm{cm}^{-1}$) have only weak intensity for graphene. Higher peak intensities have been observed for other higher harmonics like $G + D$ and $D + D'$ in narrow graphene ribbons or strongly damaged graphene [73].

The intensity ratio between certain peaks yields additional useful information. In particular, the intensity ratio between the D or D'-peak with respect to the G-peak can provide hints about the defect nature as well as the crystal grain size. This possibility is enabled by the specific scattering process of the D/D'-peak [67, 68].

The effect of disorder in graphitic samples on their Raman spectrum has first been studied by TUINSTRA and KOENIG [67]. They demonstrated that the D- to G-peak intensity ratio obeys the following relation

$$\frac{I(D - peak)}{I(G - Peak)} = \frac{C(\lambda)}{l_D}. \tag{1.9}$$

Here $C(\lambda)$ is an excitation wavelength dependent factor and l_D is the distance between two defects. The factor $C(\lambda)$ has been experimentally determined to be

$$C(\lambda) \approx 2.4 \cdot 10^{-10} \cdot \lambda^4. \tag{1.10}$$

The Tuinstra-Koenig relation is valid in the so-called stage I disorder regime of graphitic samples, which marks the transition from extended sp^2 carbon to nanocrystallites. The stage II regime involves the transition to low amorphous sp^3 carbon, followed by state III, which is highly amorphous carbon. In stage II the D to G-peak ratio is related to the amount of order rings, for which a modified equation is obtained as follows

$$\frac{I(D)}{I(G)} = C^0(\lambda) \cdot l_D^2.$$

In graphene research, stages I and II are most relevant [67]. Several studies have addressed the D to G-peak ratio in graphene with intentionally introduced defects. This has led to the development of a refined model that takes into account both stage I and II:

$$\frac{I(D)}{I(G)} = C_A \frac{\left(r_B^2 - r_A^2\right)}{\left(r_B^2 - 2 \cdot r_A^2\right)} \left[e^{\left(-\pi \frac{r_A^2}{l_D^2}\right)} - e^{\left(-\pi \frac{r_B^2 - r_A^2}{l_D^2}\right)} \right] \tag{1.11}$$

$$\text{with} \quad n_D = \frac{10^{14}}{l_D^2} \quad \text{and} \quad C_A = \frac{160 \pm 48}{E_L^4}.$$

The length travelled by the excited electron-hole pair is assumed to be $r_B - r_A = l_x$, with r_A being the region where the defective site causes structural lattice disorder. Within the radius r_B the lattice is restored. An exemplary plot is shown in Figure 1.9 for $r_A = 3.1$ nm and $r_B = 1$ nm. The Bloch waves near K and K' may still mix within r_B due to the vicinity of the defective site, which would lift the selection rules and thereby enhance the D-peak. The two radii are expected to strongly depend on the nature of the defect. The pre-factor C_A depends on the excitation energy. The peak ratio can be used to estimate the defect density n_D [74, 75].

As stated above, the D'-peak provides information on the defect nature. It has been reported that a D to D' peak ratio above 10 is indicative of sp^3-hybridization, a value of 7 reflects the presence of vacancy-like defects, while grain boundaries lead to a ratio of around 3 [75, 76].

1.3.4 Tailoring of electronic properties

Intense effort has been put into tailoring the electronic properties of graphene. The main issue is the semi-metallic nature of graphene, resulting in low on/off ratios for graphene-based transistors due to the lack of a band gap. Advantage has been taken of the 2 D nature of graphene for chemical sensing applications, as it basically consists only of surface and therefore is highly sensitive to environmental changes. Enhanced sensitivity towards certain molecules has been achieved by linking functional groups

to graphene. Thus mediated molecular interactions can lead to doping or enhanced scattering, which both alter the conductivity of the graphene sheet.

Band gap opening in graphene requires lifting of one of the protecting symmetries $\mathcal{P}$ or $\mathcal{T}$. As a consequence of such symmetry breaking, the z-component of the Dirac equation becomes relevant: $(h_z(\mathbf{k}) \neq 0)$. As long as $h_z(\mathbf{k})$ remains small, equation 1.5 is still valid and the massless Dirac particles become massive Dirac particles. The energy gap is then of the order of $2|m|$, where m is the mass of the particle. In order to lift the $\mathcal{P}$ symmetry, the two atoms in the unit cell must be rendered inequivalent. The remaining $\mathcal{T}$ symmetry imposes the same sign and magnitude of mass at K and K'. As a result, graphene becomes a trivial insulator. Introducing a magnetic distortion that has the symmetry of the lattice and a total magnetic moment of zero breaks the $\mathcal{T}$ symmetry. In this case, the masses at K and K' are numerically identical, but differ in sign, which results in a quantum Hall state ,[37, 77].

Lifting inversion symmetry by perturbing the lattice symmetry has been achieved by laterally restricting graphene. Patterning graphene into stripes or hole (antidot) lattices has been shown to open up a transport gap [78, 79]. As in practice such structuring is not selective for one specific sublattice, the observed effect is rather due to confinement and breaking of translation symmetry.

Selective modification of one of the two graphene sublattices by chemical functionalization has been attempted. Here, one has to differentiate between covalent and non-covalent modification as well as proximity-induced effects. Adsorption of transition metal atoms, a non-covalent modification, has been predicted by theory to partially turn the sp^2 into sp^3 carbon, thereby increasing the spin-orbit coupling (SOC). The enhanced SOC is expected to introduce ferromagnetic character along with band gap opening [80–82], such that graphene might be transformed into a spin Hall insulator. An increase of SOC in graphene by three orders of magnitude has been experimentally realized by placing WS$_2$ on top [22, 83, 84].

Covalent functionalization has been experimentally performed with fluorine or hydrogen with the aim of opening a band gap [86]. Covalent graphene chemistry has been inspired by the chemistry of aromatic molecules, especially benzene [87, 88]. Although graphene is chemically quite inert due to the delocalization of the π-electrons, covalent functionalization with sufficiently reactive species can nonetheless take place, provided that E$_F$ is in the vicinity of the Dirac point. One example is the linkage of phenyl radicals derived from diazonium salts, as pioneered by HADDON and co-workers [89]. It has been observed that monolayers display a higher reaction rate than bilayer graphene. The phenyl group coupling preferentially starts at the sheet edges rather than the basal plane. The proposed mechanism involves adsorption of a benzene diazonium ion on graphene, followed by an electron transfer from graphene to the ion. The latter step renders the reaction rate dependent on the position of E$_F$
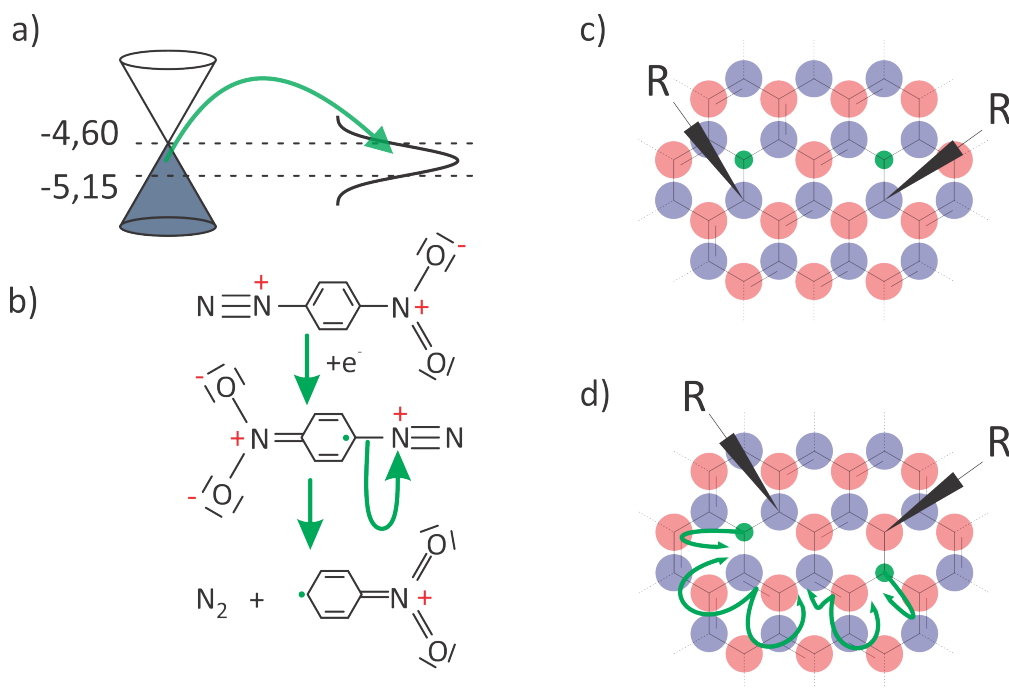
Fig. *1.10: a) For electron transfer to occur from graphene to the aromatic diazonium cation, E_F of graphene needs to be higher than the LUMO of the diazonium cation. For pristine (undoped) graphene, E_F is located at the CNP (-4.6 eV vs. vacuum level). The LUMO of the nitro- substituted benzene diazonium cation is located at -5.15 eV [85]. b) The transferred electron causes a release of molecular nitrogen. Two phenyl radicals can attach either to the same sublattice (panel c), or the two different sublattices (panel d). This generates two unpaired electrons in the vicinity of the attached group, which remain separated (c) or subsequently undergo pairing (d).*

in graphene. As depicted in Figure 1.10, the Dirac point of pristine graphene lies at 4.6 eV with respect to vacuum. To enable electron transfer to the diazonium salt, the lowest unoccupied molecular orbital (LUMO) of the diazonium ion needs to be lower in energy. For nitrosyl- and bromium-substituted diazonium salts, the redox potential is 5.15/ 5.08 eV [80, 85]. After receiving an electron, molecular nitrogen is released from the diazonium ion with the formation of a phenyl radical that covalently attaches to the underlying graphene [72, 90–93].

The diazonium modification is interesting because it leaves an unpaired electron on the lattice of graphene. According to theory, if the phenyl groups selectively attach to one sublattice, e.g., sublattice A, the unpaired electron delocalizes on sublattice B around the attached moiety. As shown in Figure 1.10, a pairing of an electron on sublattice A can only happen with an electron located on sublattice B. The chemical challenge is to steer the reaction towards one sublattice. One option to achieve this might be the use of bulky groups, like aryl-groups, in order to sterically hinder the favored 1-2 or 1-4 addition (resulting in an attachment to the B-sublattice). In

the kinetically controlled regime further addition to the same sublattice should be feasible [80]. For weak functionalization the unpaired electrons are expected to create paramagnetic moments on the graphene lattice. However, SQUID[4] and scanning tunneling microscopy measurements on phenyl-modified graphene revealed ferromagnetic behavior, indicative of sizeable coupling between the moments [19].

---

[4]superconducting quantum interference device measurements

2 Magnetotransport phenomena
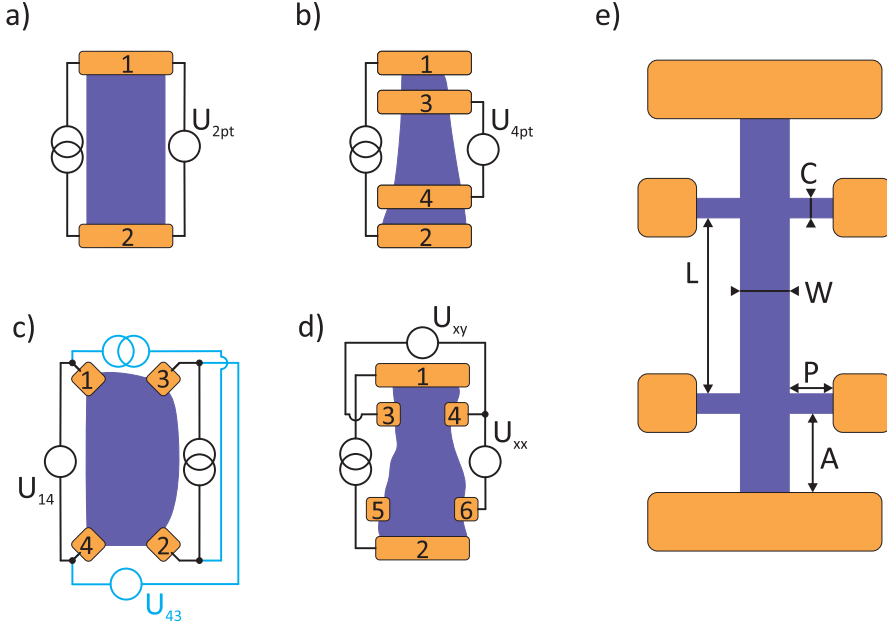
Fig. *2.1: Device configurations commonly used for electrical characterization. a),b), and d) Current is passed from contact 1 to 2. c) The* VAN DER PAUW *geometry is suitable for samples of irregular shape. In panel c), the transverse and longitudinal resistivity is obtained from two independent measurements (blue vs. black configuration). e) Hall bar device with the relevant sample dimensions.*

Electrical transport experiments are a valuable tool to probe material properties like the electronic dimensionality and the shape of the Fermi surface, thermo-electrical coefficients and electron-electron interactions. Depending on geometry of the sample and the arrangement of the electrodes, different quantities are accessible within one experiment.

In the following, different sample geometries will be described and their advantages highlighted. Subsequently the theory of charge and spin transport in general will be introduced, with focus on phenomena that where observed during this thesis.

2.1 Device geometries in magnetotransport

The quantities accessible through electrical transport and their accuracy strongly depend on the sample geometry and the arrangement of the electrodes. As shown in Figure 2.1 there exist a number of different contact geometries.

The simplest and most straightforward way of electrically contacting a sample is to put one contact at each end of the sample (geometry a). In a voltage driven experiment, the measured resistance

$$R_{2pt} = R_{\text{sample}} + 2 \cdot R_{\text{contact}} + R_{iV} + R_{iC}$$

contains the resistance of the sample as well as the contact resistance, resistance of the leads, resistances of the voltage source (iV) and the ammeter (iC). For current driven experiments the contribution of the current source (R_{iI}) can be neglected

$$\frac{1}{R_{2pt}} = \frac{1}{R_{\text{sample}} + 2 \cdot R_{\text{contact}}} + \frac{1}{R_{\text{vV}}}$$

and the resistance of the voltmeter (R_{vV}) has to be considered. These parasitic contributions can mask transport phenomena. To eliminate these unwanted contributions another pair of electrodes is needed (geometry b). The four-point resistance provides access to the specific resistivity and conductance via

$$\rho = \frac{1}{\sigma} \quad = \begin{cases} \frac{w \cdot R_{4pt}}{L} & [\Omega] \quad 2\,\text{D} \\[2ex] \frac{w \cdot t \cdot R_{4pt}}{L} & [\Omega\text{m}] \quad 3\,\text{D} \end{cases}$$

Here L is the distance between the inner electrodes, w the width of the device and t the thickness, as defined in Figure 2.1 e). In the four-point as well as two-point geometry, the measured conductance is a mixture of the longitudinal (xx) and transverse (xy) conductance. The mixing strongly depends on the ratio of width to length. For the special case of a square-shaped sample, the measured conductance is simply the geometrical average [94]

$$G_{L=W} = \frac{I_{1,2}}{U_{3,4/1,2}} \quad \approx \sqrt{\sigma_{xx}^2 + \sigma_{xy}^2}.$$

Hence, quantum phenomena are still accessible, but need special care in evaluating.

For 2 D materials like graphene, which can be electrostatically gated, the field-dependent resistance gives access to the mobility of the charge carriers as shown in equation 1.7 and can be extracted from

$$R_{2pt} = R_C + \frac{l}{W} \frac{1}{e\mu_{\text{FE}}\sqrt{n_0^2 + \left(\frac{\epsilon_0 \cdot \epsilon_r}{e \cdot d} V_{\text{Gate}}\right)^2}},$$

from a resistance vs back-gate voltage plot [95]. The mobility is also accessible from equation 1.7 if the charge carrier density n_c is known. This can be determined by two approaches. One is to define at least three electrodes at the edges of the sample like in geometry d) and e) and measure the Hall voltage (U_{xy}) by applying an out of plane magnetic field (B-field)[1]. Within this *Hall bar* configuration the error of the measured

---

[1]The other option is to determine n from Shubnikov de Haas oscillations.

quantities (U_{xx}, U_{xy}) is less than 1 % if the following geometrical relations

$$\frac{L}{W} \geq 4, \qquad \frac{C}{W} \leq 0.2, \qquad P \approx C, \qquad A \geq 4W$$

hold (see Figure 2.1 e for notation). This can be obtained by etching the sample into geometry e) [96, 97]. Geometry deviations from the ideal shape can lead to a mixing of longitudinal and transverse signals (U_{xx}, U_{xy}), as well as add a linear and/or quadratic background in the longitudinal signal.

From the measured longitudinal and transverse voltages, the specific resistances

$$\rho_{xx} = \frac{U_{4,6}}{I} \cdot \frac{W}{L} \quad = \frac{U_{xx}}{I} \cdot \frac{A}{L^2} \qquad \text{and} \qquad \rho_{xy} = \frac{U_{4,3}}{I}$$

can be obtained. These transform into conductivity as follows

$$\sigma_{xx} = \frac{\rho_{xx}}{\rho_{xx}^2 + \rho_{xy}^2} \qquad \text{and} \qquad \sigma_{xy} = \frac{\rho_{xy}}{\rho_{xx}^2 + \rho_{xy}^2}. \tag{2.1}$$

The type (sign) and density (n_{Hall}) of the charge carrier can be extracted from the slope of the transverse resistance

$$\rho_{xy} = \frac{1}{n_{Hall} \cdot e} B \qquad \Rightarrow \qquad n_{Hall} = \text{sign} \frac{1}{e \cdot \text{slope}},$$

$$\mu = \frac{\sigma_{xx}(B=0)}{e \cdot n_c} \quad = \frac{1}{e \cdot n_c \cdot \rho_{xx}(B=0)}.$$

Using the Einstein relation $(\sigma = e^2 N(E_F) D)$, the scattering time of the charge carriers can be extracted according to

$$\tau_m = \frac{m\mu}{e} \quad = \frac{\hbar k_F \mu}{e v_F} \quad = \frac{\hbar \cdot \sigma(B=0)\sqrt{\pi n_c}}{e^2 v_F}, \tag{2.2}$$

which is related to the mean free path $(l_m = \tau_m \cdot v_F)$.

The big advantage of geometry e) over all the other geometries is that the voltage probes are not invasive, i.e., they do not influence the measurement [98]. However, the required extra patterning step often necessitates additional cleaning procedures to remove the etching mask.

Another simple contact arrangement is geometry c), introduced by VAN DER PAUW. With this arrangement, ρ_{xx} as well as ρ_{xy} are accessible through measurements in the black and blue configuration. The longitudinal resistance (R_s) can be obtained from

numerically solving of the equation

$$\exp\left(\frac{R_{1,2;3,4}}{R_s}\right) + \exp\left(\frac{R_{2,3;4,1}}{R_s}\right) = 1 \quad \text{with} \quad R_s = \frac{\rho_{xx}}{t} \quad \text{and} \quad R_{i,j;k,l} = \frac{U_{i,j}}{I_{k,l}}.$$

The Hall resistance is given by

$$R_H = \frac{\left(R_{1,3;2,4}(B > 0) - R_{1,3;2,4}(B < 0)\right) + \left(R_{2,4;3,1}(B > 0) - R_{2,4;3,1}(B < 0)\right)}{4}.$$

The VAN DER PAUW method was developed for idealized point contacts at the edges. In real experiments the result of the measurement strongly depends on the overlap of the contacts with the edge.

2.1.1 Restrictions to the electrodes

As mentioned above, the configuration of the contacts, especially the voltage probes, has a strong influence on the measured quantities. In a standard experiment, the voltage probes are placed in between the source and drain contacts. The measured voltage difference can be related to an electrochemical potential μ (ECP) via

$$\Delta V = V_{p1} - V_{p2} \qquad = \frac{\mu_{p1} - \mu_{p2}}{q} \qquad = (1 - T)\left(\mu_1 - \mu_2\right)$$

which is detected by the probes. T is the transmission of an electron from the potential μ_1 of the source to the drain contact with a potential μ_2. The measured potential μ_{Pi} strongly depends on the coupling of the voltage probe to the system. By fabricating the electrodes out of the same material as the channel (e.g., by etching voltage probes as in Figure 2.1 d)) or by decoupling them using an oxide barrier, it is possible to reduce the coupling and hence the perturbation of the measurement itself. Invasive probes can act as scatterers and lead to an underestimation of the mean free path.

Ideally, the electrodes are left *floating*, meaning that the voltage measurement is *current less*. The voltage probes are then in equilibrium with the system. The distance between the electrodes should be at least one order of magnitude larger than the mean free path of the system, as otherwise the measurement is strongly affected by quantum interference effects between the probes[2]. Finally the above derivation assumes that the electrodes are identical, which is rarely the case for mesoscopic devices.

---

[2]Invasive contacts can create a barrier due to local doping underneath the probe. If the distance is less than the mean free path, the formed cavity will give rise to resonance effects like Fabry Perot oscillations.

2.2 General charge transport

For charge transport, the ballistic and diffusive transport regimes can be distinguished, as shown in Figure 2.2. To enter the ballistic regime, certain requirements concerning the quality of the sample have to be met. In most cases, experimentalists deal with diffusive charge transport where the applied electric field causes a charge carrier drift.
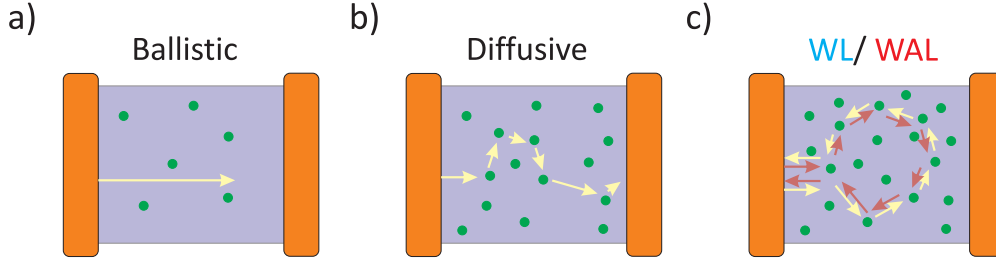
Fig. 2.2: *(a-c) Overview of charge transport regimes. The arrows visualize the current pathway, while the green dots are impurities. In the localization regime (panel c), a closed path (yellow) can interfere with its time reversed path (red). Depending on the spin-orbit coupling (SOC) strength, weak localization (WL) or weak antilocalization (WAL) can be seen in the magnetoresistance. Figure adapted from [99].*

2.2.1 Diffusive charge transport

Electrical charge transport in metals and semiconductors of macroscopic dimensions can be well described by the Drude model. In the picture of Drude theory the electrons are treated as an electron gas. Charge carriers move randomly and diffusive on the lattice background. An electrical field (E-field) acts like a drift field, which causes the carriers to move from source to drain. Main scattering mechanisms involve other electrons, phonons or impurities in the lattice. The effect of the lattice potential is accounted for by defining an effective mass $m^* \neq m_0$. The movement of the electrons can be described by a classical equation of motion

$$m^* \dot{v} + \frac{m^*}{\tau_m} v_D = -e \cdot \mathbf{E} \quad \Rightarrow \text{steady state} \quad \Rightarrow v_D = -\mu \cdot \mathbf{E}, \tag{2.3}$$
$$\text{where} \quad \mu = \frac{e \cdot \tau_m}{m^*}.$$

In the stationary state ($m^* \dot{v} = 0$), scattering and acceleration compensate each other and the carrier velocity is defined by the drift in the applied E-field. After a time τ_m the charge carriers have lost their initial momentum state due to multiple scattering events. The current density is defined as

$$\mathbf{j} = e \cdot n \cdot \mu \cdot \mathbf{E} = \sigma_0 \cdot \mathbf{E}, \tag{2.4}$$

which is consistent with Ohm's law [96]. Quantum effects can emerge on top of the classical behavior, if one geometrical sample dimension is smaller than one of the following characteristic length scales

- **mean free path** l_m is the distance an electron preserves its initial momentum. With every scattering event, the initial momentum is changed until it is completely lost after a time τ_m, which can be much larger than the time between two scattering events (τ_s). It scales inversively with temperature.

$$l_m = v_F \cdot \tau_m$$

- **phase relaxation length** By treating the electron quantum mechanically as a wave, it receives a phase ϕ. On a length scale l_ϕ, two electrons can interfere with each other in a constructive or destructive manner. Scattering that changes the phase requires a degree of freedom within the scatterer that can change upon scattering, such as a magnetic moment. l_ϕ is an important benchmark for the transition from a quantum mechanical to a classical diffusive system.

$$l_\phi = \sqrt{D \cdot \tau_\phi} \quad = \frac{\sqrt{v_F^2 \cdot \tau_m \cdot \tau_\phi}}{2}$$

- **Fermi wavelength** For low temperatures, charge transport is mainly carried by electrons close to the Fermi level, which makes the Fermi wavelength a relevant scale. For a carrier concentration of $1 \cdot 10^{12}$ cm^{-2} the Fermi wavelength is 25 nm

$$\lambda_F = \frac{2h}{\mathbf{p}_F} \quad = \frac{2\pi}{\mathbf{k}_F} \quad = \frac{2h}{\sqrt{2m_e E_F}} \quad = \sqrt{\frac{2\pi}{n}}.$$

The above length scales define mesoscopic systems that are in-between classical Ohmic (macroscopic systems) and pure quantum mechanical systems. They strongly scale with temperature, but are also material property. Accordingly mesoscopic transport can be observed in samples with dimensions in the micrometer range not only at low temperatures [100].

2.2.2 Electrical transport regimes

Quantum effects are usually smeared or averaged out due to the macroscopic dimensions of the sample and the relatively high temperature at ambient conditions. Reducing the size of the system and/or lowering temperature can make one of the above described quantities larger than the sample dimensions. This can lead to counterintuitive phenomena, stemming from the quantum nature of the electrons. Besides the already mentioned three length scales, there is a fourth one that also

needs to be considered. The localization length ξ describes the spacial expansion of the electron wave function and is sensitive to potential fluctuations. By comparing the four relevant length scales to the smallest geometrical length scale L of the sample, different transport regimes can be defined [96, 101].

- **diffusive classical transport** $L, \xi \gg l_m \geq l_\phi \gg \lambda_F$
  The electron conductivity is well described by the Drude model for electron gases. Random walk can be used to describe the trajectories of electrons due to scattering dominated transport.

- **mesoscopic systems** $l_\phi > L$
  The dimensionality of a system depends on the relation of l_ϕ to the dimensions of the sample. If one of the sample dimensions is smaller than l_ϕ, the system is 2 D ($L, W > l_\phi > T$). Further classification into ballistic ($L, W << l_m$) and diffusive ($L, W \gg l_m$) mesoscopic systems depends on wether the main scattering mechanism is dominated by the sample boundary or impurities.

- **ballistic transport** $l_m > L, W$
  The length between two scattering events is larger than any dimension of the sample. As a consequence the electron propagates without scattering and reaches the drain contact with its initial momentum state. Transport is "non-Ohmic" and the conductance is given by $\sigma = \frac{2e^2}{h} \cdot M$, where M is the number of modes that can carry one quantum of conduction ($\frac{2e^2}{h}$). The conductor can be regarded as an electron waveguide.

- **weak localization** $L, \xi \gg l_\phi \gg l_m > \lambda_F$
  The motion of the electron at low temperatures can be described by quantum diffusion. For long coherence lengths the electron can interfere with itself leading to localization effects. As l_ϕ has a strong temperature dependency, this regime can be left by heating the sample.

- **strong localization** $\xi \approx l_m \approx \lambda_F$
  A distinction between the classical ($\xi \geq l_\phi$) and quantum ($\xi < l_\phi$) regime can be made. In the classical case, transport is described as incoherent or coherent hopping between localized states. Interference can take place between alternative hopping paths in the coherent case.

2.2.3 Ordinary Magnetoresistance (OMR)

In the classical picture of the Drude model, a magnetic field orthogonal to the direction of motion introduces a Lorentz force. This effect is classified as ordinary magnetoresistance (OMR). Two distinct regimes for the OMR can be defined by the product of the cyclotron frequency ω_c ($= e \cdot B/m^*$) with the mean free scattering time τ_m. In the weak limit ($\omega_c \cdot \tau_m << 1$), a magnetic field ($B = (0, 0, B_z)$), orthogonal to the direction of motion, deflects the electrons between every scattering event. Within this

limit, the magnetoresistance (MR) is governed by the scattering processes. Diluting the scatterers or increasing the magnetic field strength ($\omega_c \cdot \tau_m >> 1$), the particles will move on circular orbits in a corkscrew fashion, and the detailed shape of the Fermi surface governs the transport. Expanding equation 2.3 to include the magnetic field

$$
\begin{pmatrix} v_x \\ v_y \\ v_z \end{pmatrix} = \frac{\mu}{1 + (\omega_c \cdot \tau_m)^2} \begin{pmatrix} 1 & \omega_c \cdot \tau_m & 0 \\ -\omega_c \cdot \tau_m & 1 & 0 \\ 0 & 0 & 1 + (\omega_c \cdot \tau_m)^2 \end{pmatrix} \begin{pmatrix} E_x \\ E_y \\ E_z \end{pmatrix},
$$

gives the conductivity

$$
\boldsymbol{\sigma} = \frac{n \cdot e \cdot \mu}{1 + (\omega_c \cdot \tau_m)^2} \begin{pmatrix} 1 & \omega_c \cdot \tau_m & 0 \\ -\omega_c \cdot \tau_m & 1 & 0 \\ 0 & 0 & 1 + (\omega_c \cdot \tau_m)^2 \end{pmatrix}
$$

and by tensor inversion the resistivity

$$
\boldsymbol{\rho} = \frac{1}{n \cdot e \cdot \mu} \begin{pmatrix} 1 & -\omega_c \cdot \tau_m & 0 \\ \omega_c \cdot \tau_m & 1 & 0 \\ 0 & 0 & 1 \end{pmatrix}, \tag{2.5}
$$

with both having magnetic field-dependent elements. For thin or 2 D samples, the current flow in z-direction can be neglected, such that the tensor reduces to a 2×2 matrix. Hence conductivity and resistivity transform into each other according to equation 2.1. In the case of $\omega_c \cdot \tau_m >> 1$ the off-diagonal elements

$$
\sigma_{xy} = -\sigma_{yx} \quad = \frac{n \cdot e \cdot c}{B}, \qquad \rho_{xy} = \frac{B}{n \cdot e}
$$

correctly describe the Hall effect. It is noteworthy that the Drude model predicts the longitudinal resistance to be independent of the magnetic field

$$
\rho_{xx} = \frac{1}{n \cdot e \cdot \mu},
$$

that is in contradiction to the experimentally observed non-zero MR

$$
\delta \rho_{xx} = \frac{\rho_{xx}(B) - \rho_{xx}(0)}{\rho_{xx}(0)}
$$

in metals and semiconductors [102, 103]. This discrepancy can be resolved within the Drude model by expanding it to more than one charge carrier with each having a

different drift velocity v_i. The current density then becomes

$$\mathbf{j} = n \cdot e \left(\sum_i v_i \right) \quad = \left(\sum_i \boldsymbol{\sigma}_i \right) \mathbf{E}$$

and thus the conductivity tensor is the sum of all individual conductivities. Longitudinal and transverse conductivity

$$\sigma_{xx} = \sum_i \frac{\sigma_{0,i}}{1 + \beta_i^2}, \quad \sigma_{xy} = \sum_i \frac{\beta_i \cdot \sigma_{0,i}}{1 + \beta_i^2},$$

$$\text{where} \quad \beta_i = \frac{e_i \cdot B}{m_i \cdot c} \tau_i \quad \text{and} \quad \sigma_{0,i} = \frac{n_i \cdot e_i^2 \tau_i}{m_i}$$

are now functions of the individual charge e_i, mass m_i and the scattering time τ_i with respect to the i independent charge carriers. The discrimination of charge carriers directly follows from the band structure of the material. For transition metals, charge carriers can differ on wether they belong to s- or d-bands. In semiconductors, different curvatures of overlapping sub bands in the conduction (valence) band give rise to heavy and light electrons (holes). In addition, depending on the temperature and position of the Fermi level, both electrons and holes simultaneously contribute to charge transport. The latter can be described by two carriers ($e_1 = -e_2$), with different masses and scattering times for the electrons and holes.

In the strong magnetic field limit, the transverse conductivity

$$\sigma_{xy} = \frac{(n_2 - n_1) \cdot |e| \cdot c}{B}$$

depends on the difference between the electron and hole concentration. For equal concentrations it becomes zero and hence the Hall-voltage vanishes. Following equation 2.1 the longitudinal resistivity now simplifies to

$$\rho_{xx} = \frac{1}{\sigma_{xx}} \quad \approx \left(\mu_{eff} \cdot B \right)^2 \frac{1}{n \cdot |e| \cdot \mu_{eff}}, \tag{2.6}$$

where an effective mobility ($\frac{1}{\mu_{eff}} = \frac{1}{\mu_1} + \frac{1}{\mu_2}$) is assumed. In this limit, the MR has a quadratic dependence on the magnetic field, and does not saturate. For non-equal concentrations, this model is able to describe the experimentally observed quadratic MR, as well as the saturation of the MR.

For metals like Bi, Sb, Ag or Au where only electrons contribute to the charge transport, this model cannot explain the observed MR. Here, non-saturating MR is observed, which originates from the shape of the Fermi surface. For a free electron gas, the Fermi level lies completely in the first Brillouin zone and has the shape of a sphere. For

transition metals, the Fermi surface can take complex shapes. Along some directions in k-space, it may even extend out of the first Brillouin zone. Due to the periodic boundary conditions, a continuous surface will form along this direction in k-space (assumed in k_x direction in the following). A current in real space will have to travel along the y-direction in order to take advantage of the open orbit along k_x. If a magnetic field is applied, the charge carriers start to move on closed orbits on the Fermi surface normal to the applied field. For a closed Fermi surface, e.g., the current flowing in the x-direction, the resistivity

$$\rho_{xx} \approx \frac{n \cdot e \cdot \mu}{1 + s}$$

will saturate for high B-fields, while a current in the y-direction (along the open orbit)

$$\rho_{yy} \approx \frac{(\mu \cdot B)^2}{n \cdot e \cdot \mu} \frac{s}{s+1},$$

will, in analogy to equation 2.6, rise quadratically due to the continuous Fermi surface [103]. Here s is defined by $\sigma_{yy} = s \cdot n \cdot e \cdot \mu$.

2.2.4 B-field dependent quantum oscillations

As already stated, a magnetic field will bend the trajectory of an electron according to the Lorentz force. If the mean free scattering time allows the electron to perform a closed orbit ($\omega_c > \frac{1}{\tau_m}$), the electron will start to interact with itself. On the closed orbit, the electron will accumulate a phase, which leads to constructive or destructive interference. Only radii with a multiple of 2π as a phase factor will form closed orbits, resulting in a quantization of the trajectories. These discrete states are called Landau Levels (LLs).

The corresponding Hamiltonian for this problem

$$H = \sum_{i=1}^{N} \frac{\left(p_i - \frac{e}{c} A(r_i)\right)^2}{2m}$$

can be solved with the ansatz of a standing wave in the Landau gauge. The eigenvalue solutions are similar to those of a one dimensional quantum mechanical harmonic oscillator with

$$E(n) = \hbar \omega_c \left(n + \frac{1}{2}\right) \underbrace{+ \frac{\hbar^2 k_z}{2m}}_{3\,\text{D extension}} .$$
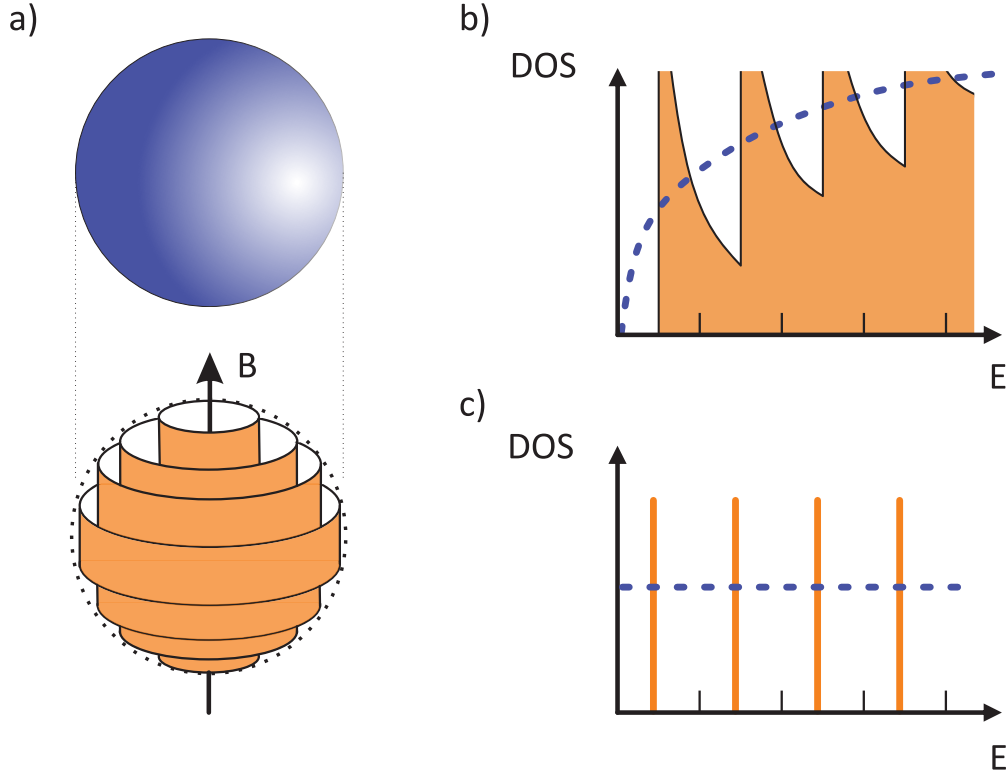
Fig. *2.3: a) The Fermi surface of a free electron gas is a sphere. Upon applying a B-field, Landau levels emerge as cylinders parallel to the B-field. b-c) Energy vs. density of states (DOS) for a 3 D (b) and 2 D (c) system without (dashed blue line) and with an externally applied B-field (orange).*

Accordingly, 2 D systems have LLs in the shape of a ring. By comparison 3 D systems have LL in the shape of a cylinder, due to the continuum of states in the z-direction (see Figure 2.3).

Dirac fermions in 2 D differ from Schrödinger fermions by the energetic spacing of their LLs. While latter have a constant spacing of $\hbar\omega_c$, Dirac fermions follow

$$E_{\pm}(N) = \pm\sqrt{\left(\frac{2e\hbar v_F B}{C}\right) N},$$

which is symmetric around the charge neutrality point[3].

As can be seen from Figure 2.3 b), the formation of LL changes the DOS spectrum. For the 2 D case it can be described by a delta function

$$\mathcal{D}_{2D}(E,B) = \underbrace{\frac{|e|B}{h}}_{n_L}\sum_{n,\sigma}\delta\left(E - E_n^{\sigma}\right) \xrightarrow[\text{level broadening}]{\text{due to}} \sum_0^n \frac{n_L}{\pi}\frac{\frac{\hbar}{2\tau q}}{(E - E_n)^2 + \left(\frac{\hbar}{2\tau q}\right)^2},$$

---

[3]Here $\pm$ refers to the positive and negative energy side of the Dirac point.

located at E_n, the energy of a LL. Scattering causes a broadening of the DOS and the delta function is replaced by a Lorentzian. Letting the number of LL go to infinity ($n \to \infty$), the DOS can be written as

$$\mathcal{D}_{2D}(E,B) = \frac{m^*}{\pi\hbar^2}\left(1 - 2\exp\left[-\frac{\pi}{\omega_c\tau_q}\right]\cos\left[2\pi\frac{E_F}{\hbar\omega_c}\right]\right). \tag{2.7}$$

The effect of the formation of LL on the transport is quite drastic. It will become visible, provided that

$$\hbar\omega_c >> \begin{cases} \frac{\hbar}{\tau_m} & \text{broadening due to scattering} \\ \frac{3}{2}k_BT & \text{thermal broadening}, \end{cases}$$

which results in well-separated LLs. Rewriting the cyclotron frequency in terms of applied B-field

$$\frac{eB}{m} >> \frac{1}{\tau_m} \quad \Rightarrow B \quad >> \underbrace{\frac{m}{e\tau_m}}_{\mu^{-1}}$$

gives an estimate on the sample quality, which is required to detect signatures of the LLs in charge transport. For a mobility of 10^4 cm^2/(V s) they will be manifested above 1 T [100].

Implementing the above result into the Drude model as a linear perturbation, the following expression for the longitudinal resistance of 2 D systems

$$\rho_{xx}(B,T) = \underbrace{\frac{m^*}{n_{SdH}e^2\tau_m}}_{\rho_0}\left(1 - \underbrace{2\exp\left[-\frac{\pi}{\omega_c\tau_q}\right]}_{3}\underbrace{\frac{\frac{2\pi^2k_BT}{\hbar\omega_c}}{\sinh\left[\frac{2\pi^2k_BT}{\hbar\omega_c}\right]}}_{2}\underbrace{\cos\left[j\pi\frac{E_F}{\hbar\omega_c} - \phi\right]}_{1}\right)$$

can be used to describe quantum oscillation effects due to LL formation, the so called *Shubnikov-de Haas* (SdH) oscillations. They originate from the passing of LLs through the Fermi surface, which reduces the longitudinal resistivity due to the newly available states, and are centered around ρ_0, the classical Drude resistivity. The numerated terms of the SdH oscillations provide access to:

1. **charge carrier density** The cosine modulation gives rise to minima for values (2N-1)π of the argument with N being an integer. Substituting E_F with equa-

tion 1.8, $\omega_c = eB/m^*$ and $m^* = \frac{\hbar k_F}{v_F}$ gives the following relation [104]

$$\frac{j\pi h n_s}{2eB} - \phi = (2N-1)\pi \quad \begin{cases} \phi = \pi & \text{Dirac} \\ \phi = 2\pi & \text{Schrödinger} \end{cases}$$

By plotting $B_{min}^{-1}(= 4|e|N/hn)$ versus continuous integer values the carrier density n_s can be extracted from the slope. For graphene $j = 1$. The intersection with the ordinate corresponds to the phase ϕ and helps to discriminate between Dirac and Schrödinger particles. In the 3 D case, the oscillations provide access to the reciprocal vector k_F. From measurements of the three principal axis (a,b,c) of the system, the carrier density can be obtained from

$$n_{3D} = \frac{1}{3\pi^2} k_F^a k_F^b k_F^c.$$

2. **cyclotron mass** From the temperature dependency of the amplitude of one oscillation

$$B_{min,i}(T)/B_{max,i}(T) = \frac{\frac{2\pi^2 k_B T}{\hbar\omega_c}}{\sinh\left[\frac{2\pi^2 k_B T}{\hbar\omega_c}\right]} \quad \text{with} \quad \omega_c = \frac{e \cdot B}{m^*} \tag{2.8}$$

the cyclotron mass m^* can be extracted.

3. **LL broadening** At temperatures below the Dingle-Temperature T_D, the effect of thermal damping is small ($T \ll T_D$). By fitting the envelope of the SdH oscillations to

$$\frac{\rho(B) - \rho_0}{\rho_0} \frac{\frac{2\pi^2 k_B T}{\hbar\omega_c}}{\sinh\left[\frac{2\pi^2 k_B T}{\hbar\omega_c}\right]} = 2\exp\left[-\frac{\pi}{\omega_c \tau_q}\right],$$

the quantum life time τ_q can be derived, which is a measure of the broadening of momentum eigenstates

$$T_D = \frac{\Gamma}{\pi k_B} = \frac{\hbar}{2\pi \tau_q k_B}.$$

The ratio of τ_q and τ_m yields information about the main scattering process in the sample. From the definition of both scattering times

$$\frac{1}{\tau_q} = n_{\text{impurities}} v_F \int_0^\pi \mathcal{Q}(\Theta)\left[1 + cos(\Theta)\right] d\Theta,$$

a)   b)
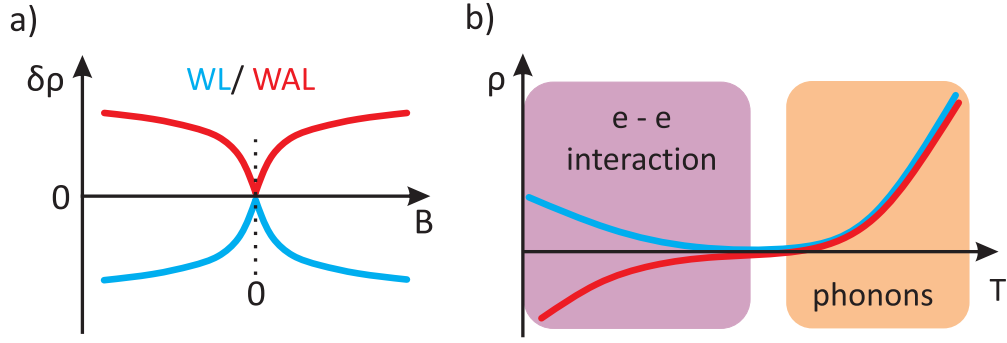
Fig. *2.4: a) Depending on the spin-orbit coupling (SOC) strength, weak localization (WL, blue curve) or weak antilocalization (WAL, red curve) can be seen in the magnetoresistance as a cusp at B = 0. b) After freezing-out the phonons, the WL (WAL) can be distinguished by the temperature dependence of resistance. As T→0, the system becomes more insulating (metallic) in the WL (WAL) case (blue vs. red curve). Figure adapted from [99].*

$$\frac{1}{\tau_m} = n_{\text{impurities}} \nu_F \int_0^\pi \mathcal{Q}(\Theta) \left[1 + cos\,(\Theta)\right] \left[1 - cos\,(\Theta)\right] d\Theta,$$

it is evident that they are a measure of different scattering angles, where $\mathcal{Q}$ defines the scattering potential. While $1 - cos\,(\Theta)$ describes large angle scattering events, $1 + cos\,(\Theta)$ attributes for small scattering angles. For graphene, τ_m is weighted by the product of both, which differs from the normal $2\,D$ case, where only $1 + cos\,(\Theta)$ is included. This makes τ_m insensitive to large and small scattering angles. The quantum scattering time in graphene, on the other hand, is sensitive to small backscattering angles.

Large τ_m/τ_q ratios are a signature of long range scatterers or charge impurities buried deep in the supporting substrate. When these charged scatterers come closer to the graphene sheet the ratio approaches 2 [104–106].

2.2.5   Quantum correction to low field magnetotransport

While the above quantum oscillations require samples with a sufficiently large scattering time/length, high mobility and rather high magnetic fields, quantum localization effects can be seen in conductors with lower mobility and at comparatively small magnetic fields.

As outlined in section 2.2.2, the phase coherence length is a benchmark for the type of transport regime present. For disordered diffusive systems at low temperature the weak localization regime is entered (Fig. 2.2 c), which can lead to strong localization at even lower temperatures.

2.2.5.1   Localization effects

Coherent motion pathways between multiple scattering events can interfere on a closed trajectory leading to a reduction of the conductivity which is neglected in

classical Drude theory. For a system with a large phase coherence length[4] and time reversal symmetry, like that shown in Figure 2.2 c), an electron can travel around a closed loop clockwise or counter-clockwise giving rise to quantum interference at the crossing of the trajectories. Interference is constructive as the two paths are the same resulting in a higher probability to back-scatter. Each wave can be described quantum mechanically by the following ansatz

$$|A^{\pm}(B)\rangle = A^{\pm}\exp\left(\pm\boldsymbol{i}\varphi^{\pm}(B)\right),$$

where $\pm$ refers to the clockwise or anti-clockwise path [96, 100]. The probability of returning to the origin on these two paths is given by the probability of reflection

$$P(m \rightarrow m) = |\langle A^{-}|A^{+}\rangle|^2 \quad = |A^{+}|^2 + |A^{-}|^2 + 2|A^{+}|\cdot|A^{-}|\cos\left(\varphi^{-}-\varphi^{+}\right). \qquad (2.9)$$

Without any magnetic field and under time reversal symmetry, the pathways interfere constructively ($\varphi^{+} \equiv \varphi^{-}$). This requires that the amplitudes of both paths are the same ($A^{+} \equiv A^{-}$), resulting in a reflection probability of $4|A|^2$. In the classical case without coherence between the path, the probability is just the sum of the squares ($P = 2|A|^2$). In a 2 D system, this leads to a correction (decrease) in the conductivity of

$$\sigma_{\text{quantum}} = \sigma_{\text{classical}} - \frac{e^2}{\pi h}\ln\left(\frac{\tau_{\varphi}}{\tau_m}\right)$$

which is proportional to the ratio of the phase coherence and mean free scattering time. This holds as long as the starting and end point are identical, which can be anywhere in the sample. This effect is called *weak localization*, as the number of transport pathways through the sample is reduced and the electron get localized.

Weak localization (WL)
Upon applying a B-field normal to the enclosed area, electrons will pick up an additional phase shift

$$A^{\pm}(B) = \pm A_0\exp\left(-\boldsymbol{i}\frac{e}{\hbar}BS_p\right),$$

which is proportional to the area S_p enclosed by the path. Naively inserting this ansatz into equation 2.9 could give rise to B-field oscillations. However, in a mesoscopic sample there exist many individual paths with different enclosed areas that interfere with themselves. Only when no B-field is applied, the paths are in phase and will start to average each other out as the B-field is increased. The resulting magnetoconductance curve is sketched in Figure 2.4 d) by the red line. As the B-field is increased the

---

[4]This is usually achieved by cooling the system to ^{4}He temperature

constructive interference is lost and the classical conductance value is restored. The resulting dip in the magnetoconductance can be modeled by

$$\delta\sigma = \frac{e^2}{2\pi^2\hbar}\left[\psi\left(\frac{1}{2}+\frac{\hbar}{4eDB\tau_\varphi}\right)-\psi\left(\frac{1}{2}+\frac{\hbar}{4eDB\tau_m}\right)+\ln\left(\frac{\tau_\varphi}{\tau_m}\right)\right]$$

for a 2D system. Here, ψ is the digamma function and D the diffusion constant of the system.

Weak anti-localization (WAL)
For systems with strong spin-orbit coupling (SOC) or which host Dirac particles, the situation is somewhat different. In particular, the charge carriers pick up a phase of π while traveling the closed loop, leading to destructive interference of the two time-reversed paths. For Dirac particles, the phase shift stems from the Berry phase of the system. An external magnetic field will again add an additional phase to the path, destroying the destructive interference and restoring the classical Drude conductivity. The B-field dependent conductivity for a 2D system can be described by the model of Hikami, Larkin and Nagaoka (HNL)

$$\delta\sigma(B) = \frac{\alpha e^2}{2\pi^2\hbar}\left[\psi\left(\frac{1}{2}+\frac{\hbar}{4eBl_\varphi^2}\right)-\ln\left(\frac{\hbar}{4eBl_\varphi^2}\right)\right], \tag{2.10}$$

where the prefactor α is -0.5 for each transport channel carrying a Berry phase of π or being affected by strong SOC [107]. In the case of strong SOC, every scattering event on the closed loop rotates the spin. SOC can be understood as an intrinsic B-field. The overall phase that is picked up equals π and thus the interference is constructive [108].

Graphene
As charge transport in pristine graphene is governed by Dirac fermions, it should exhibit WAL due to the Berry phase of π. However, experimentally WL was observed significantly more often. This is due to the interplay of the chiral nature of the charge carriers and elastic scattering events (inter- and intravalley). The correction to the magneto-conductivity (MC)

$$\sigma\frac{\pi h}{e^2} = F\left(\frac{eB}{\hbar l_\varphi^{-2}}\right)-F\left(\frac{eB}{\hbar\left(l_\varphi^{-2}+2l_i^{-2}\right)}\right)-2F\left(\frac{eB}{\hbar\left(l_\varphi^{-2}+l_i^{-2}+l_*^{-2}\right)}\right)$$

$$\text{with}\quad F(z) = \ln(z)+\Psi\left(\frac{1}{2}+\frac{1}{z}\right)\quad\text{and}\quad l_{\varphi,i,*} = \sqrt{D\tau_{\varphi,i,*}}, \tag{2.11}$$

derived by MᴄCᴀɴɴ ᴇᴛ ᴀʟ, describes not only the phase breaking mechanism (τ_φ) but also elastic intervalley (τ_i) and intravalley scattering (τ_*) between and within the Dirac cones [109]. The former process describes scattering at sharp defects, resulting in a scattering between the two Dirac cones. The latter (τ_*) incorporates elastic scattering by extended scatterers (size of the lattice constant), dislocations or ripples that breaks the chirality due to scattering within each valley [110]. The model assumes that momentum relaxation is the shortest timescale present and does not affect the chirality of the system. As long as inter- and intravally scattering occurs on a much shorter time scale than the coherent motion ($\tau_\varphi >> \tau_i, \tau_*$) WL is seen in graphene [111].

2.2.5.2 Decoherence

The temperature dependence of the phase coherence time (decoherence) reveals information about the main underlying phase breaking mechanism of the charge carriers. Usually the decoherence rate $1/\tau_\varphi$ is used in this context and follows a power law dependency with temperature

$$\frac{1}{\tau_\varphi} \propto (k_B T)^p .$$

In the case of inelastic electron-electron scattering p is 3/2 for 3 D, 1 for 2 D and 2/3 for 1D systems. This is usually observed in pure samples at low temperatures ($\approx 4\,\text{K}$) when all phonons are frozen out [112].

As the temperature is further lowered[5] a change in slope or even a saturation of the phase coherence length has been observed for different systems. The origin of this behavior is related to spin-spin scattering or non-equilibrium effects [113, 114]. Hot-electron effects or electromagnetic noise sources might also be relevant as they can influence the electron bath. Hence, the design of the measurement set-up is very important. The magnitude (RMS) of the measuring current should be limited to prevent Joule heating. Also the sample geometry may limit the phase coherence time, if the corresponding length reaches the dimension of the sample [110].

2.3 Spin transport

Today's electronic devices utilize the charge of electrons and holes to carry out logic operations. In contrast, data storage additionally utilizes the magnetic moment μ_e of the electron. It is defined as

$$\mu_e = \frac{-g \cdot e}{m \cdot c} \bar{s} \quad = \frac{\pm e \hbar}{2 \cdot m \cdot c} \quad = \mu_B$$

---

[5]This can be done with ^{3}He-systems
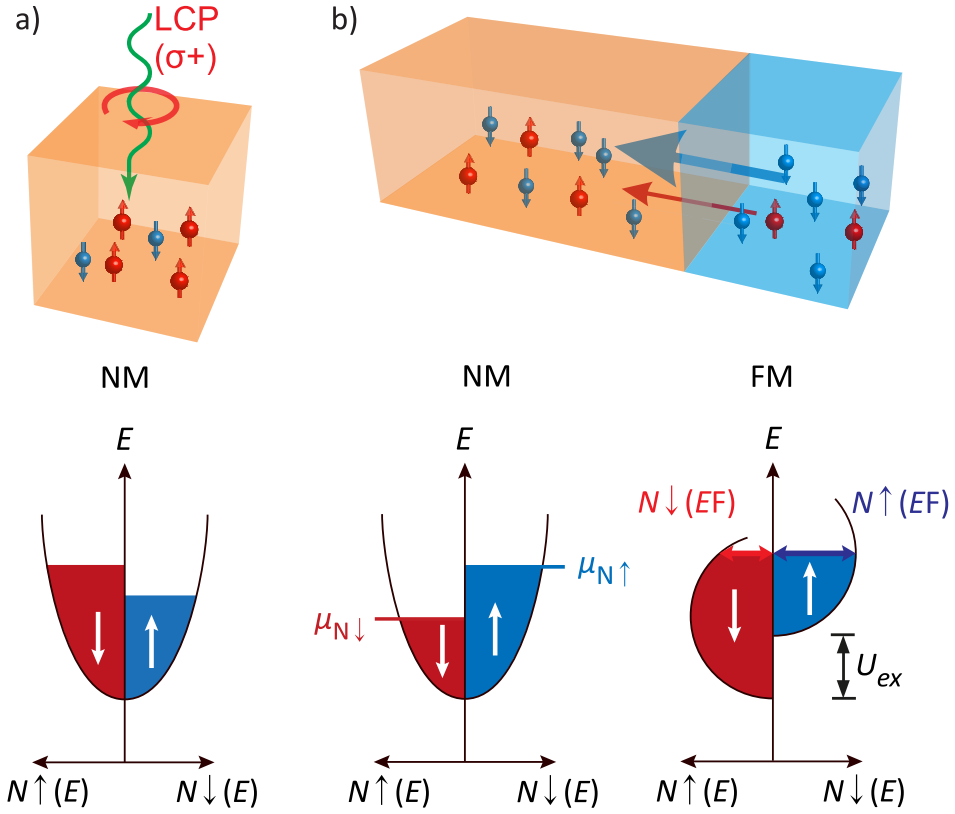
Fig. *2.5: a) Circular polarized light can be used to induce a spin imbalance in materials with spin-orbit coupling (SOC). b) Electrically induced spin imbalance with the aid of a ferromagnetic contact (FM). The splitting of the bands (U_{exc}) in the FM leads to a spin-dependent DOS ($N(E_F)$), which generates a spin polarized current. This can be used to induce a spin imbalance ($\mu_\uparrow \neq \mu_\downarrow$) in a nearby non-magnetic material (NM) [115].*

by the spin state $\bar{s}$ of the electron, which is $\pm 1/2$.

The concept of exploiting the spin of an electron for logic operations opens the field of *spintronics* (spin electronics). Here a spin imbalance in the channel is used to process information. A major obstacle for spintronics is to generate the spin imbalance, e.g. spin polarization, in a non-magnetic material

$$P_n = \frac{n_\uparrow - n_\downarrow}{n_\uparrow + n_\downarrow},$$

so that more electrons are spin-up ($N_\uparrow$) than -down ($N_\downarrow$), or vice versa. It can be induced by optical (by using circular polarized light Fig 2.5 a), resonant or transport methods (spin polarized currents (Fig 2.5 b) [116]. For compact devices, the last approach is most convenient.

By passing the current through a polarizing medium, such as magnetic oxides (EuO, LMSO) or ferromagnets (FM = Co, Fe, Ni or their alloys), sizable current polarization

in non-magnetic channel materials (NM) like copper, silicon or graphene has been achieved [17, 117, 118].

Spin polarization in ferromagnets originates from the energetic splitting (U_{ex}) of the d-band for up- and down-spins due to exchange interactions and can be described by the Stoner model. As depicted in Figure 2.5 b) (lower right), the d-band is split in a spin-dependent manner with one subband lifted by U_{exc} with respect to the other. Due to this splitting, the lower d-subband is filled with more electrons, leading to the magnetization of the material. As second consequence, the density of states (DOS) at the Fermi level ($N(E_F)$) is different for the two spin orientations ($N_\uparrow(E_F) \neq N_\downarrow(E_F)$). Using the Einstein relation the spin-dependent conductivity

$$\sigma_{\uparrow\downarrow} = e^2 D_{\uparrow\downarrow} N_{\uparrow\downarrow}(E_F)$$

with a spin-dependent diffusion constant D can be defined ($D_\downarrow \neq D_\uparrow$). The difference in $N_{\uparrow\downarrow}(E_F)$ (Figure 2.5 b) leads to different magnitudes in $\sigma_{\uparrow\downarrow}$. While both s- and d-electrons have a finite DOS at the Fermi level and contribute to the conductance, the s-electrons dominate due to their higher DOS. Momentum scattering from the s-band into the d-band are the main source of scattering and strongly spin-dependent. As spin-flip scattering times are usually much larger than the momentum scattering time, scattering between the bands will not depolarize the current. Thus, conduction occurs in parallel through two independent spin channels that have different conductivities [6].

The important point is that the electrical current carried by the d-bands can be simplified as the sum of two spin-dependent currents ($J = J_\uparrow + J_\downarrow$), which results in a net polarization ($J_s = J_\uparrow - J_\downarrow$). They can be modeled independently within the *two current model* introduced by MOTT in 1936 [29, 115, 116].

2.3.1 AMR, GMR and TMR

Applying an external magnetic field parallel to an applied current in a ferromagnetic structure like in Figure 2.6 a) leads to an *anisotropic magnetoresistance* (AMR).

The resistive change is on the order of $\frac{\Delta\rho}{\rho} \lesssim 0.02$ and results from the change of the scattering cross-section as the magnetic field is swept. Starting from a parallel alignment of the ferromagnet with respect to the external B-field (blue line), as depicted in panel b), domains will start to rotate as the B-field is reversed, reducing the scattering cross-section and hence the resistance. Once the coercive field of the structure is reached, all domains align again parallel to the external field. The result is a positive resistance change [119–121].

With the development of electron beam lithography (EBL), numerous studies have been performed on ferromagnetic nanostructures concerning AMR. The main result is that the coercive field $B_{c,FM}$ of a nanostructured ferromagnet changes with its width
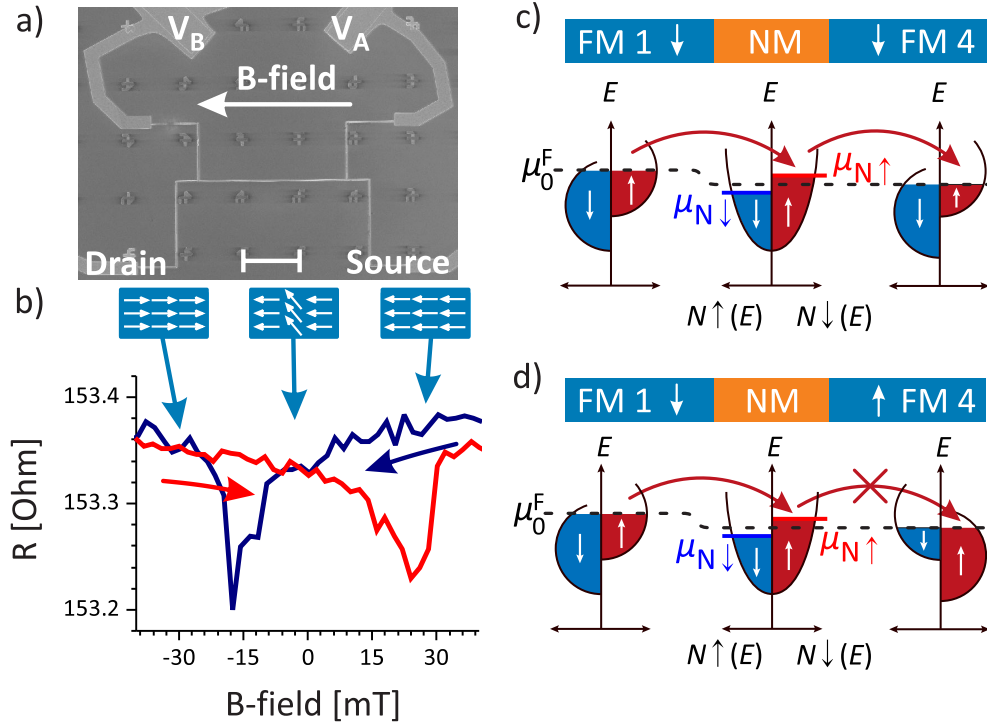
Fig. 2.6: *a) Scanning electron micrograph of a Co-stripe (500 nm width) used to detect the anisotropic magnetoresistance (AMR) (scale bar 10μm). b) The MR shows two distinct resistance changes upon sweeping the in-plane B-field. c) (FM/NM/FM) sandwich structure giving rise to GMR. For parallel magnetization of the two ferromagnetic contacts, the majority spin (up direction) has nearly the same DOS in all three materials. d) In the antiparallel configuration, the spin-up DOS is drastically reduced in the contact FM4, leading to increased resistance due to spin-dependent scattering at the NM/FM4 interface [115, 119].*

and thickness. Sections of different width and thickness can be decoupled from each other effectively by 90° turns as shown by the SEM image in Figure 2.6. For Co it has been found that cobalt oxide couples antiferromagnetically to the metallic Co. This leads to a decrease of the AMR and the coercive field. Thus, Co nanostructures are often capped to prevent oxidation [122–125].

A higher change in resistance ($\frac{\Delta\rho}{\rho} \lesssim 0.15$) can be achieved when a non-magnetic metal (NM) is sandwiched between two ferromagnets (FM1, 4) with different coercive fields, leading to the *giant magnetoresistance* (GMR). As shown in Figure 2.6 c) and d) the parallel alignment of FM1 and FM4, gives rise to a low resistance state. The DOS for both types of spins is the same in both FMs. When an anti-parallel configuration is reached, the density of the major spin species in FM1 is different to FM4, leading to spin-dependent scattering processes at the NM/FM4 interface. As a consequence, the anti-parallel configuration has a higher resistance. Replacing the non-magnetic

metal by an insulator I, *tunneling magnetoresistance* (TMR) occurs with even higher resistive changes on the order of 0.7 [121, 126].

2.3.2 Spin injection and spin transport

When moving from a stacked device geometry like that shown for the GMR in Figure 2.6 c-d), to an extended lateral geometry, like that shown in Figure 2.7 a), spin properties of the *sandwiched* non-magnetic layer (NM) can be probed or even manipulated by external means like artificial scatterers, chemical functionalization or electrostatic gates.

The device must have at least two electrodes, but usually four are used. As sketched in Figure 2.7 a), the contacts are designed to have different widths to achieve different switching fields (B_c) of the electrodes[6] as the magnetic field is swept in-plane parallel to the major axis of the electrodes.

Based upon the two-current model, a non-equilibrium current in the diffusive regime

$$\mathbf{j}_{\uparrow,\downarrow} = \sigma_{\uparrow,\downarrow}\mathbf{E} - eD_{\uparrow,\downarrow}\nabla\delta n_{\uparrow,\downarrow} \quad \text{with} \quad \delta n_{\uparrow,\downarrow} = n_{\uparrow,\downarrow} - n_{0,\uparrow,\downarrow} \tag{2.12}$$

is driven either by an E-field ($\mathbf{E} = -\nabla\phi$) and/or by a gradient in the carrier density $\delta n_{\uparrow,\downarrow}$ and influenced by the spin-dependent conductivity σ and diffusion constant D. In the following, labels $\uparrow, \downarrow$ are used to distinguish between spin-dependent quantities. Defining a spin-dependent electrochemical potential $\mu_{\uparrow,\downarrow}$ (ECP), the spin-dependent current can be written as

$$\mathbf{j}_{\uparrow,\downarrow} = -\frac{\sigma_{\uparrow,\downarrow}}{e}\nabla\mu_{\uparrow,\downarrow} \quad \text{with} \quad \mu_{\uparrow,\downarrow} = \frac{e^2 D_{\uparrow,\downarrow}}{\sigma_{\uparrow,\downarrow}}\delta n_{\uparrow,\downarrow} + e\phi_{\uparrow,\downarrow},$$

where the electrical potential ϕ acts in the same manner on both spin species as they have the same charge. In the steady state the continuity equations

$$\nabla\left(\mathbf{j}_{\uparrow} + \mathbf{j}_{\downarrow}\right) = 0 \quad \text{and} \quad \nabla\left(\mathbf{j}_{\uparrow} - \mathbf{j}_{\downarrow}\right) = -e\frac{\delta n_{\uparrow}}{\tau_{\uparrow\downarrow}} + e\frac{\delta n_{\downarrow}}{\tau_{\downarrow\uparrow}} \tag{2.13}$$

ensure the conservation of charge current $\mathbf{j} = \mathbf{j}_{\uparrow} + \mathbf{j}_{\downarrow}$ and introduce a position dependent spin current $j_s = \mathbf{j}_{\uparrow} - \mathbf{j}_{\downarrow}$. The current polarization is given by the ratio j_s/j. Spin-dependent scattering rates ($1/\tau_{\uparrow\downarrow}$) connect state $\uparrow$ with $\downarrow$ and vice versa. Both define the spin relaxation time

$$\tau_s = \frac{\tau_{\uparrow\downarrow}\tau_{\downarrow\uparrow}}{\tau_{\uparrow\downarrow} + \tau_{\downarrow\uparrow}}.$$

---

[6]This is a consequence of the AMR.
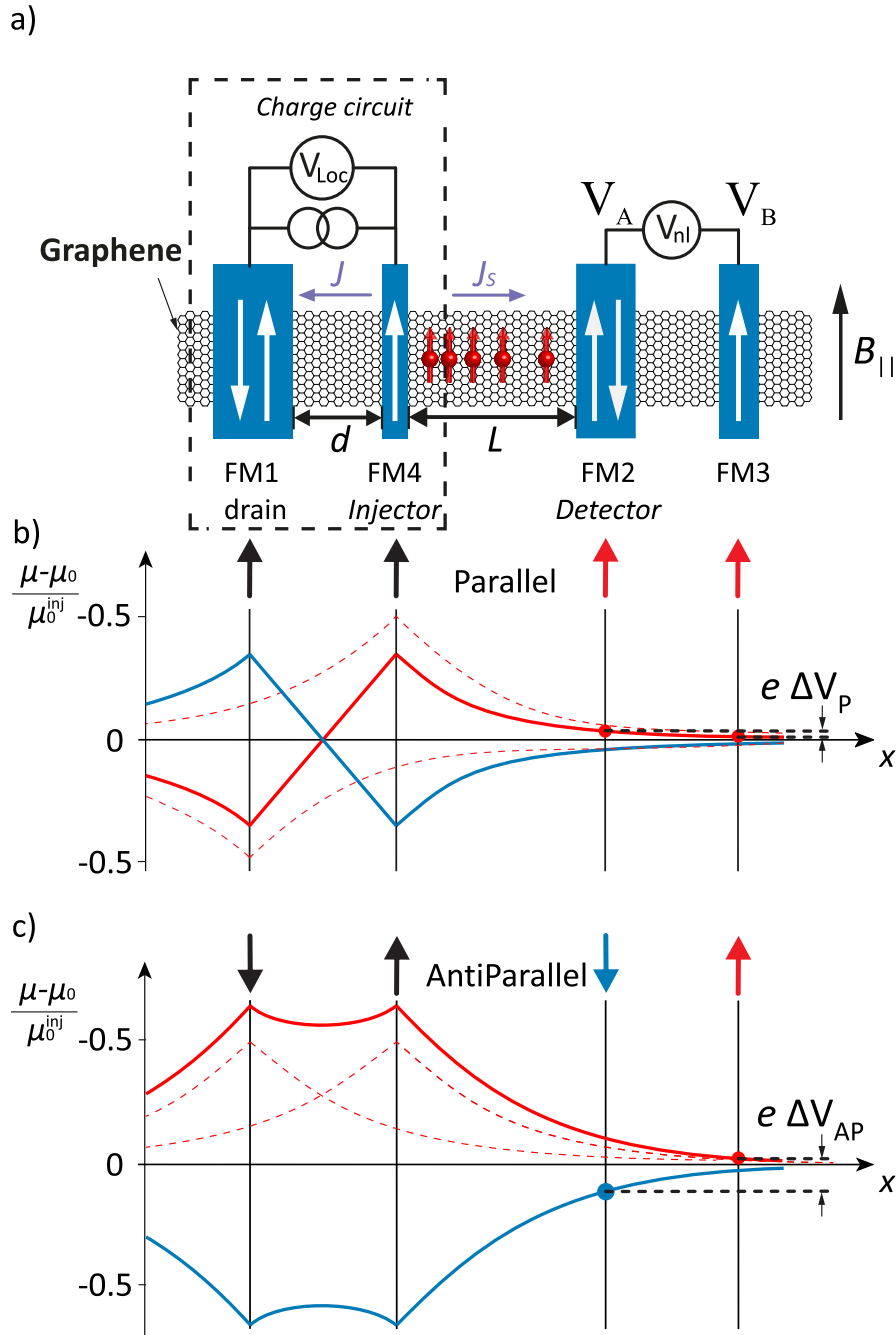
Fig. 2.7: a) Schematic depiction of a graphene-based spin valve. The electrodes are numbered according to their coercive fields and connected in the nonlocal measurement configuration. b),c) Spin dependent electrochemical potential (solid lines) for parallel (panel b) and anti-parallel (panel c) configuration. Dashed lines are the potential induced by the individual contacts. The relative magnetization of the electrodes is indicated together with the measured potentials [115].

Assuming that depopulation of the polarization due to spin-dependent scattering

in equilibrium is the same for both spins ($N_\uparrow \tau_{\downarrow\uparrow} = N_\downarrow \tau_{\uparrow\downarrow}$), the ECP can be described by

$$\nabla^2 \left(\sigma_\uparrow \mu_\uparrow + \sigma_\downarrow \mu_\downarrow \right) = 0 \quad \text{and} \quad \nabla^2 \left(\mu_\uparrow - \mu_\downarrow \right) = \frac{\mu_s}{\lambda_s^2} \quad \text{with} \mu_s = \mu_\uparrow - \mu_\downarrow, \quad (2.14)$$

where a spin-average diffusion constant

$$D = \frac{\sigma_\downarrow D_\uparrow + \sigma_\uparrow D_\downarrow}{\sigma} \quad \text{with} \quad \sigma = \sigma_\uparrow + \sigma_\downarrow$$

and spin diffusion length $\lambda_s = \sqrt{D\tau_s}$ is used [116, 127]. Here, μ_s is often referred to as spin accumulation

$$\mu_s = \frac{I_s \cdot \tau_s}{A \cdot d},$$

and depends on the polarized current I_s per volume unit.

To analyse the ECP across the FM4/NM interface (Figure 2.8), the above equations can be applied separately to the ferromagnet and the NM-channel. A charge current is driven by an E-field across FM4/NM/FM1, with a net spin polarization $\mathbf{j}_s$. Spin-dependent quantities in the ferromagnet, like the conductivity and diffusion constant, become spin-independent in the non-magnetic channel ($\sigma_\uparrow = \sigma_\downarrow = 0.5\sigma$).

The solution for equations 2.14 is an exponential ansatz

$$\mu_{NM,\uparrow,\downarrow} = \mu_{NM}^* \pm \left[a_1 \exp\left(-\frac{|x|}{\lambda_{NM}} \right) - a_2 \exp\left(-\frac{|x-L|}{\lambda_{NM}} \right) \right] \quad (2.15)$$

$$\text{with} \quad \mu_{NM}^* = -\frac{eI}{\sigma_{NM} A_{NM}} x \quad \text{and} \quad A_{NM} = d_{NM} w_{NM}$$

$$\mu_{FM_4}^{\uparrow,\downarrow} = \mu_{FM}^* \pm \frac{b_4}{\sigma_{FM,\uparrow,\downarrow}} \exp\left(-\frac{z}{\lambda_F} \right) \quad (2.16)$$

$$\text{with} \quad \mu_{FM}^* = -\frac{eI}{\sigma_{FM} A_J} z + eV_1, \quad \text{where} \quad = 0 \text{ for } x > 0$$

for both sides of the interface, where the charge current is implemented by μ^*[7]. The cross-section of the channel A_{NM} and the contact area A_J have to be taken into account. For the ferromagnetic electrodes, the current is assumed to flow along the z-direction. This is reasonable for the interface as long as the thickness t_{FM} is much larger than the spin diffusion length λ_F of the ferromagnet[8].

---

[7]Charge current is only considered for x<0 as shown in Figure 2.7 a).
[8]Typical values are λ_F(FeNi) = 5 nm and λ_F(Co) = 30 nm [128].
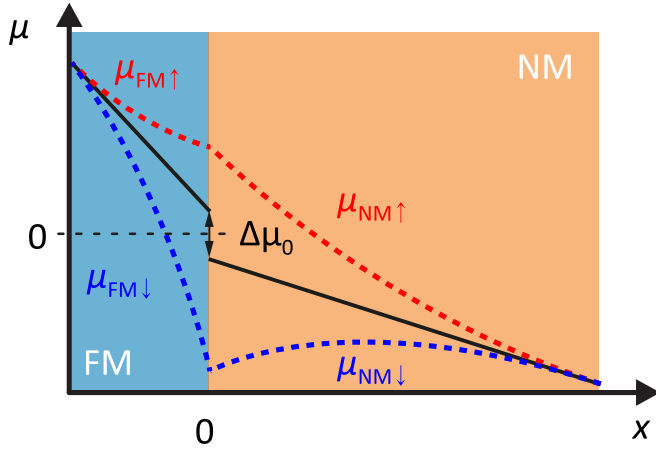
Fig. 2.8: Scheme depicting the spin-dependent electrochemical potential μ (red and blue dashed line for spin-up and spin-down orientation, respectively) across the FM/NM interface. The induced spin imbalance decays exponentially over a characteristic length scale λ. The magnitude of the discontinuity $\Delta\mu_0$ in the overall electrochemical potential (black line) depends on $\mathbf{j}R_c$. Adapted from [115].

At the interface FM4/NM ($x = 0$) both current components fulfill

$$\mathbf{j}_{\uparrow,\downarrow}(x = 0) = \sigma_{c,\uparrow,\downarrow}\left(\mu_{NM,\uparrow,\downarrow}(0) - \mu_{FM,\uparrow,\downarrow}(x = 0)\right)$$

where a spin-dependent interface conductivity σ_c is introduced. The ECP across the interface can be written as

$$\mu_{s,NM}(x = 0) - \mu_{s,FM}(x = 0) = 2R_c\left(P_j - P_\sigma\right)j$$
$$\mu_{NM}(x = 0) - \mu_{FM}(x = 0) = R_c\left(1 - P_j P_\sigma\right)j,$$

with an effective contact resistance $R_c = \sigma/4\sigma_\uparrow\sigma_\downarrow$ and conductivity polarization $P_\sigma = (\sigma_\uparrow - \sigma_\downarrow)/\sigma$. The spin imbalance on both sides of the interface

$$\mu_{s,FM}(X = 0) = 2R_{FM}\left(P_J - P_{\sigma,FM}\right)j \quad \text{and} \quad \mu_{s,NM}(x = 0) = -2r_n P_j j$$

leads to the definition of the current polarization in the channel

$$P_j = \frac{R_c P_{\sigma,c} + R_{FM} P_{\sigma,FM}}{R_c + R_{NM} + R_{FM}},$$

with the effective resistances

$$R_{NM} = \frac{\rho_{NM}\lambda_{NM}}{A_{NM}} \quad \text{and} \quad R_{FM} = \frac{\rho_{FM}\lambda_{FM}}{A_J}$$

and the contact resistance R_c. As Ohmic contacts show little or no contact resistance ($R_c = 0$), the polarization is determined in first order by the ratio of the effective resistances (R_{FM}/R_{NM}). In particular for semiconductors, as non-magnetic materials, they do not match ($R_{FM} << R_{NM}$) and the above equation implies inefficient generation of spin imbalance ($P_j \lesssim 0.01$) in a NM. This issue is termed as *conductivity*

mismatch [129]. One way to overcome this hurdle is to ensure high contact resistances, which can be achieved by inserting an insulating layer (I) between FM and NM[9] resulting in a tunnel-barrier [130]. The disadvantage is a high power consumption of such devices.

2.3.3   Nonlocal spin currents

As shown in Figure 2.7 b), the spin imbalance described by equation 2.15 and 2.16 leads to an exponential decay outside of the current circuit ($x > 0$) in the NM channel. For the parallel alignment of FM4 and FM1 one type of spin species is injected by FM4 while the other one is extracted from NM by FM1. This alters the gradient of the ECP inside the current path where the steepness depends on on the contact separation d.

A ferromagnetic probe will sense, according to

$$\mu_{p1} = \mu^* + \frac{\vec{P}_1\vec{\mu}_s}{2} \qquad = \mu^* + |P| \cdot |\mu_s| \cos[\phi],$$

both charge μ^* and spin currents. Importantly, it measures the projection of the spin vector $\vec{\mu}_s$ on its own magnetization vector $\vec{P}$[10]. Spin currents can be measured independently from charge currents with a set of voltage probes (FM2 and FM3) placed outside the current path (Figure 2.7 a)[131, 132]. In this manner charge based effects like the Hall effect, anisotropic magnetoresistance and quantum interferences can be minimized, which otherwise could mimic or mask spin-related signals [133]. The detected voltage difference between FM2 and FM4 can be used to define a nonlocal resistance

$$R_{nl} = \frac{V_{nl}}{I}.$$

When sweeping an in-plane B-field parallel to the contacts, as shown in Figure 2.9 a), the electrodes of different width will reverse their magnetization direction at different fields B_c. For the parallel contact configuration both electrodes will detect the same spin-dependent ECP (Fig. 2.7 b). In the antiparallel configuration the detected ECP will be different for each electrode according to the different magnetization direction (Fig. 2.7 c). This jump in voltage (V_{nl}) is called the spin-valve effect (Fig. 2.9 c). The number of jumps depends on the spin diffusion lenght λ and the spin polarization achieved in the transport channel. Two jumps, as shown in Figure 2.9 a), are seen with at least two ferromagnetic contacts. The magnitude of the corresponding resistance

---

[9]The resulting stack is abbreviated FM/I/NM

[10]$\vec{P}$ must not lie along the easy axis of the contact.
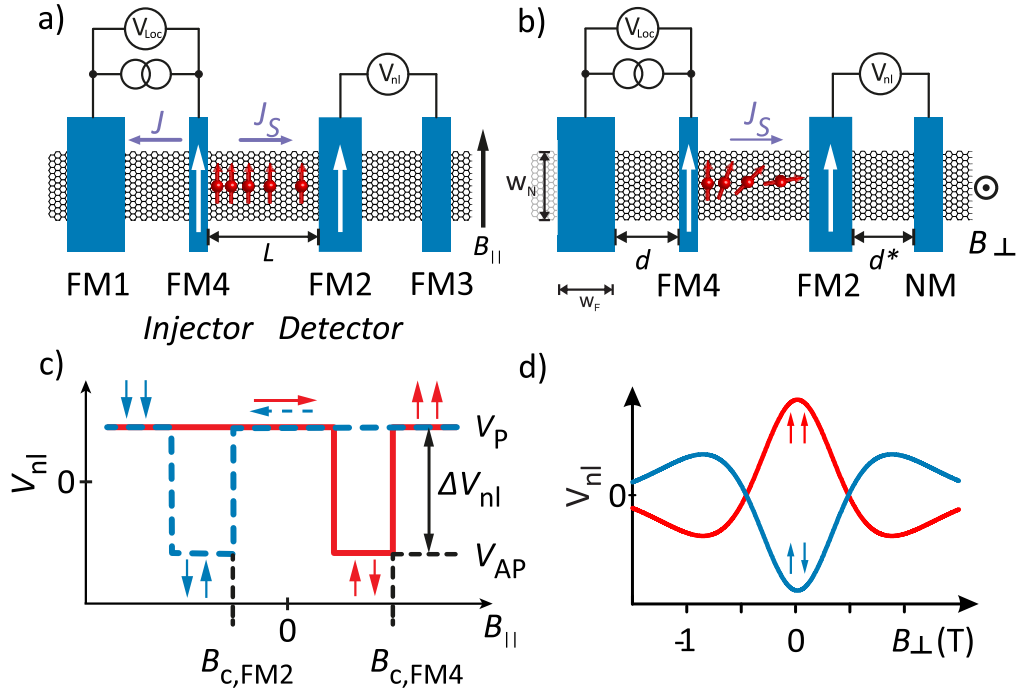
Fig. 2.9: *a) Typical device configuration for a nonlocal spin valve. Several devices with different contact separation L are needed to determine the spin lifetime through sweeping an in-plane B-field. b) Use of an out-of-plane B-field to determine τ_s via the Hanle effect. c) Typical switching behavior of a spin-valve for an in-plane B-field sweep. d) An out-of-plane B-field causes the electrons to precess while they diffuse to the detector. A change of the B-field strength alters the precession frequency and hence the angle projected onto FM2, which in turn causes a change in V_{nl}.*

jump

$$\Delta R_{nl} = R_{NM} \frac{\left(2P_{c,1}R_{c,1} + 2P_{FM}R_{FM}\right)\left(2P_{c,2}R_{c,2} + 2P_{FM}R_{FM}\right)\exp\left(-\frac{L}{\lambda_{NM}}\right)}{\left(1 + 2R_{c,1} + 2R_{FM}\right)\left(1 + 2R_{c,2} + 2R_{FM}\right) - \exp\left(-2\frac{L}{\lambda_{NM}}\right)} \quad (2.17)$$

depends on the contact resistance R_c of the injector FM4 and detector FM2, the spacing (L) between them, the effective resistances of the ferromagnets and the channel (R_{FM}, R_{NM}), the current polarization P and the spin diffusion length in the channel λ_{NM}. Also the nature of the drain contact and its separation from the injector d can influence the spin signal. For a non-magnetic (NM) drain electrode, only the injector will manipulate the spin bath giving rise to the dashed line in Figure 2.7 b).

Simplified expressions for eq. 2.17 can be obtained for transparent and tunneling

contacts

$$\Delta R_{nl,\text{transparent}} = 2P^2 R_{NM} \left(\frac{R_C}{R_{NM}}\right)^2 \frac{\exp\left(-\frac{L}{\lambda_{NM}}\right)}{\left(1 + 2\frac{R_C}{R_{NM}}\right)^2 - \exp\left(-\frac{2L}{\lambda_{NM}}\right)} \quad \propto \quad \frac{1}{R_{NM}}$$

(2.18)

$$\Delta R_{nl,\text{tunnel}} = R_{NM} P^2 \exp\left(-\frac{L}{\lambda_{NM}}\right) \quad \propto \quad R_{NM}$$

(2.19)

that show a different scaling with the channel resistance [134]. The assumptions in the first case are that $R_{FM} << R_C, R_{NM}$ and that R_C is approximately the same for all contacts. In the latter case $R_{FM}, R_C << R_{NM}$ is required. For a channel material with an adjustable resistance like graphene, measuring ΔR_{nl} for different channel resistances helps to characterize the contact behavior[11].

The above equations can also be used to determine the current polarization from the measured spin signal ΔR_{nl} for different contact separations or for a given λ_s[12].

2.3.4 Spin lifetime measurements

General the relaxation and dephasing of the magnetization M of a spin ensemble can be treated within the phenomenological framework of the BLOCH-TORREY equations in three dimensions

$$\frac{\partial M_x}{\partial t} = \gamma (M \times B)_x - \frac{M_x}{T_2} + D\nabla^2 M_x$$

(2.20)

$$\frac{\partial M_y}{\partial t} = \gamma (M \times B)_y - \frac{M_y}{T_2} + D\nabla^2 M_y$$

(2.21)

$$\frac{\partial M_z}{\partial t} = \gamma (M \times B)_z - \frac{M_z - M_z^0}{T_1} + D\nabla^2 M_z \quad \text{with} \quad \gamma = \frac{\mu_B g}{\hbar}$$

(2.22)

Equation 2.20 and 2.21 describe the dephasing of the spin ensemble in the x,y plane under a static magnetic field in the z-direction $B = B_{0,z}$. This occurs on the timescale T_2 called the transverse dephasing time. The relaxation of the spin population to thermal equilibrium is described by equation 2.22. This takes place within a timescale T_1 called the longitudinal dephasing time.

In spin-valve devices the spin relaxation time τ_s is electrically measured by applying an out-of-plane magnetic field ($B = B_z$, $B_{x,y} = 0$). This leads to a precession of the spin ensemble with the lamor frequency ω_L around the applied B-field. Starting at the detector, the spin ensemble is align along y-axis, parallel to both injector an detector.

---

[11]The resistance of graphene can be changed by changing the carrier density, which can be adjusted via electrostatic gating.

[12]Which can be extracted from Hanle-measurements.

While the ensemble diffuse the distance L from the injector to the detector during the time $t = L^2/D_s$, the magnitization vector of the ensemble rotates in the xy plane due to the precession. With increasing B-field strength, the precession frequency increases and accordingly the orientation of the spin ensemble with respect to the detector magnitization changes after they have traveled the distance L. This results in a reduction of the nonlocal voltage, as the projection of the magnetization of the spin ensemble onto the magnetization vector of the detector electrode is reduced as the B-field is increased. Experimentally, a constant current is used, leading to a constant spin imbalance e. g. time dependency is just given by the time the ensemble need to travel from the injector to the detector. As the experimental timescale[13] is much larger than the spin lifetime, a steady state is reached quite fast. This leads to the equation

$$\underbrace{D_s\nabla^2\mu_s}_{\text{diffusion}} - \underbrace{\frac{\mu_s}{\tau_s}}_{\text{relaxation}} + \underbrace{\omega_L \times \mu_s}_{\text{precession}} + \underbrace{\mu\mathbf{E}\nabla\mu_s}_{\text{drift}} = \frac{\partial\mu_s}{\partial t} = 0 \quad \text{with} \quad \omega_L = \frac{g\mu_B B_z}{\hbar} \qquad (2.23)$$

where drift effects due to an E-field can be neglected for nonlocal measurements. For isotropic and cubic solids, as well as metals the two relaxation times are identical ($T_1 = T_2 = \tau_s$) [115]. Considering a 1 D channel with an injector and detector (four-point nonlocal measurement) the solution to equation 2.23 as a function of B_Z is given by

$$\Delta R_{nl} = \frac{P_{NM}^2 R_{NM} D_s}{W} \int_0^\infty \underbrace{\frac{\exp\left(-\frac{L^2}{4D_s t}\right)}{\sqrt{4\pi D_s t}}}_{\text{diffusion time distribution}} \underbrace{\cos(\omega_L t)}_{\text{spin precession}} \underbrace{\exp\left(-\frac{t}{\tau_s}\right)}_{\text{spin flip probability}} dt.$$

This function is difficult to fit to experimental data, such that various analytical expressions for the above equation have been derived. For evaluating the present experimental data, the expression

$$R_{nl}^{\text{Hanle}} = \pm\Delta R_{nl}\frac{1}{2\sqrt{1+(\omega_L\tau_s)^2}}$$

$$\times \left[\sqrt{1+\sqrt{1+(\omega_L\tau_s)^2}}\cos\left(\frac{L\omega_L\tau_s}{\sqrt{2D_s\tau_s}\sqrt{1+\sqrt{1+(\omega_L\tau_s)^2}}}\right)\right.$$

---

[13]A typical experiment uses an AC-current with a DC-offset. The AC-frequency is usually below 50 Hz due to impedance mismatch originating from the high contact resistance.

$$-\frac{\omega_c \tau_s}{\sqrt{1+\sqrt{1+(\omega_L \tau_s)^2}}} \sin\left(\frac{L\omega_L \tau_s}{\sqrt{2 D_s \tau_s}\sqrt{1+\sqrt{1+(\omega_L \tau_s)^2}}}\right)\Bigg]$$
$$\times \exp\left(-\frac{L}{\sqrt{2 D_s \tau_s}}[\sqrt{1+\sqrt{1+(\omega_L \tau_s)^2}}\right) \tag{2.24}$$

has been used [135] and is fitted together with a linear and quadratic term to the magnetoresistance data. If the contact separation is set to zero (L=0), this corresponds to a three-terminal nonlocal measurement, where V_A is connected to the source contact. In this case the resulting magnetoresistance curve with the Hanle-effect is fitted with the following Lorentzian function [136]

$$R_{nl} = \frac{P^2}{e^2 N(E_F) A}\left(\frac{\tau_s}{1+(\omega_L \tau_s)^2}\right). \tag{2.25}$$

3 Sample preparation and characterization

As the miniaturization of electronic device components continues, it becomes necessary to identify novel types of nanostructures and tailor their electronic properties. Top-down and bottom-up approaches are two complementary strategies for nanostructure fabrication. The top-down approach requires a material whose dimensions can be reduced without deteriorating its crystalline structure and integrity. A common method involves the cleaving and thinning of layered materials with the aid of adhesive tapes. By repeatedly pulling adhesive tapes off each other, the material is thinned down. In the last step, the adhesive tape is pressed onto the target substrate in order to transfer the ultrathin sheets. The exfoliation technique requires that the material consists of only weakly (van der Waals) bonded layers. Suitable layered materials include graphite and transition metal dichalcogenides (TMDCs) like MoS_2 or WSe_2. The thickness of exfoliated sheets can be further reduced by laser thinning, where a high power laser beam is used to sublimate the top most layers [137, 138]. Furthermore, lateral structuring is achievable by reactive ion or wet chemical etching, in order to pattern the object into a shape compatible with the device configuration.

The bottom-up approach provides convenient access to nanostructures of high structural quality. It works for a wide range of materials which do not have to belong to the class of layered materials. In general, wet chemical and vapor phase methods can be distinguished, the latter of which commonly yields samples of higher quality, i.e., a lower density of impurities and defects. Vapor phase-grown nanostructures, in comparison, often contain impurities originating from incorporation of the transport agents used in the synthesis. For instance, bromium is incorporated into nanostructures grown via the VAN ARKEL DE BOER process, wherein the halogen serves as a gas phase transport agent [139].

Nanostructures of high crystallinity can be obtained by evaporating the bulk material (source) at the hottest zone of a tube furnace under inert gas flow, as shown in Figure 3.1. The gas flow transports the material downstream, where it condenses on the colder surface and crystallizes. Size and shape of the resulting nanostructures are determined by the evaporation temperature, gas background pressure, amount of source materials, temperature gradient, gas flow rate and the type of substrate [140–143]. By placing metal nanoparticles (e.g., Bi, Ag and Au) as growth catalysts on the substrate, the crystallization and growth characteristic can be influenced [144]. Due to their small size, the particles melt at slightly lower temperatures than the corresponding bulk material. In the small droplets, material from the gas phase dissolves and as the concentration of the dissolved material reaches the saturation limit, crystallization starts. Accordingly, this approach is called vapor-liquid solid (VLS) growth. Another advantage of the use of metal nanoparticles is that the diameter of the resulting nanowires can be controlled by the size of the particles [145].

3.1 PVD growth of SnTe nanostructures

For the growth of SnTe nanostructures, a three-zone horizontal tube furnace is equipped with a quartz tube and a quartz boat[1]. On the left side, the tube is connected to a flow controller, which allows to adjust the flow of argon 5.0 in the range of $1 - 150$ sccm. To speed up the venting processes the flow controller is bridged with a bypass.

At the other end of the tube, a pressure gauge[2] and a needle valve are connected in line to a pumping station[3]. The needle valve is used to set the pressure in the tube. For a faster evacuation process the needle valve is bridged by a bypass. Figure 3.1 shows the temperature profile of the oven at a set growth temperature of $550\,^{\circ}$C together with a time profile at the source position. The source material is placed in the hottest zone of the oven, which is 44 cm from its left end. SnTe powder is used as a source and the growth substrates are placed $7 - 15$ cm away from it, where the temperature is between $544\,^{\circ}$C and $366\,^{\circ}$C.
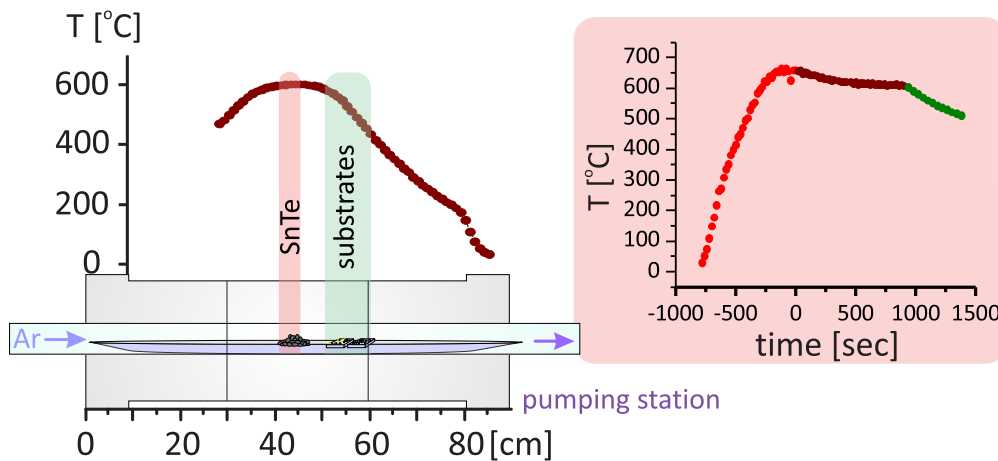
Fig. *3.1: left panel) Schematic illustration of the three-zone tube furnace, along with the temperature profile. The source material is placed at the hottest zone (44 cm from the left opening of the furnace). right panel) Temperature ramp at the source position. It comprises the heat-up period (red), followed by the growth period (brown), and finally the cool-down period (green).*

The shown temperature profile was recorded when the oven's internal sensors reached a constant target temperature of $550\,^{\circ}$C. This information is relevant, as the time profile of the temperature at the source position indicates an overshoot by almost $100\,^{\circ}$C. For the internal temperature sensors this is only $10\,^{\circ}$C. This difference results from the way the oven is constructed and controlled. The heating rate is set by the

---

[1]The quartz boat extends through the whole oven.

[2]Betriebsmanometer mit Feinteilung from Leybold, 1500 to 0 mTorr with a precision of 1 %

[3]HighCube 80 Eco from Pfeiffer
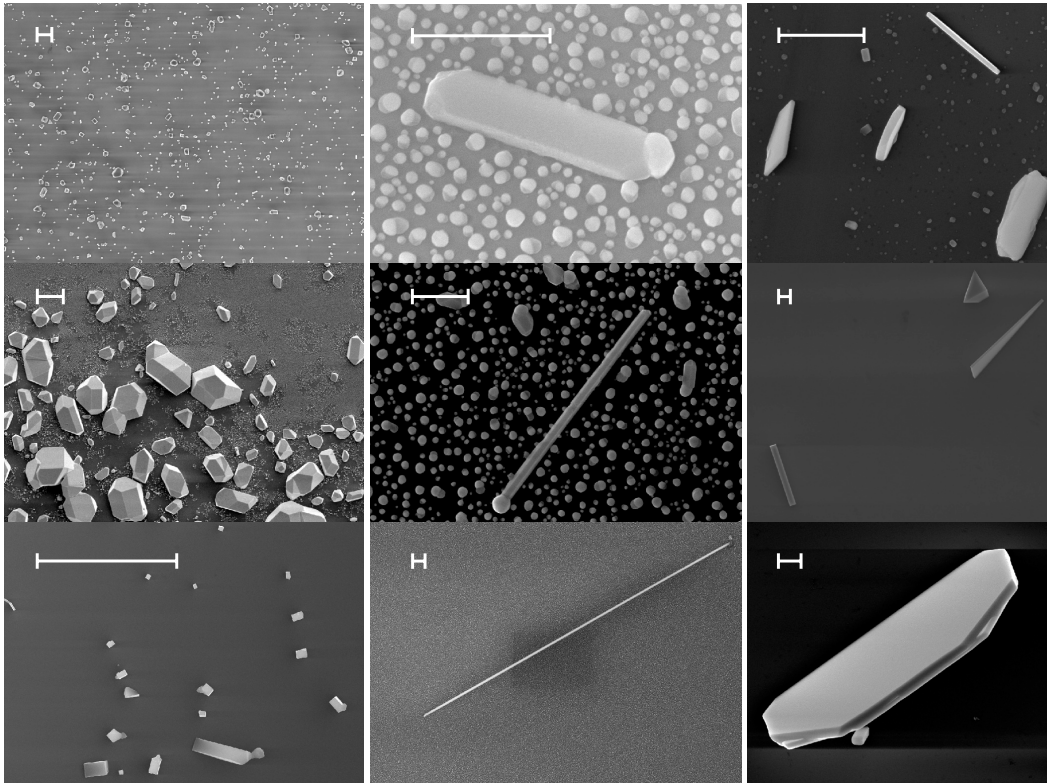
Fig. *3.2: Scanning electron micrographs of different crystal morphologies obtained for SnTe. The first row shows nanocrystals obtained for unbalanced conditions, while examples of wires grown under optimized conditions are presented in the second row. Vapor-liquid-solid growth increases the yield of nanowires. The last row shows results for optimized growth of platelets, which partially grow in a twinned fashion. Scale bar 5/ 0.5/ 1 μm from left to right column.*

temperature controller of the oven. It had been optimized by previous users to reach $600\,^oC$ on a stable basis. As the temperature sensor is located in the isolation of the coil, modifications of the system would primarily result in a better temperature reading, and thus affect the ramping of the temperature. The latter factor has a sensitive influence on the growth and hence further modifications were avoided after the first successful growth [146].

A typical growth process consists of the following steps:

1. Cleaning of the growth substrates (plus in some cases depositing 1-2 nm Au as a catalyst).
2. Placing the source at 44 cm from the entrance side of the quartz boat (this will be the hottest spot).
3. Placing the substrates at a specified position with respect to the source in the boat.
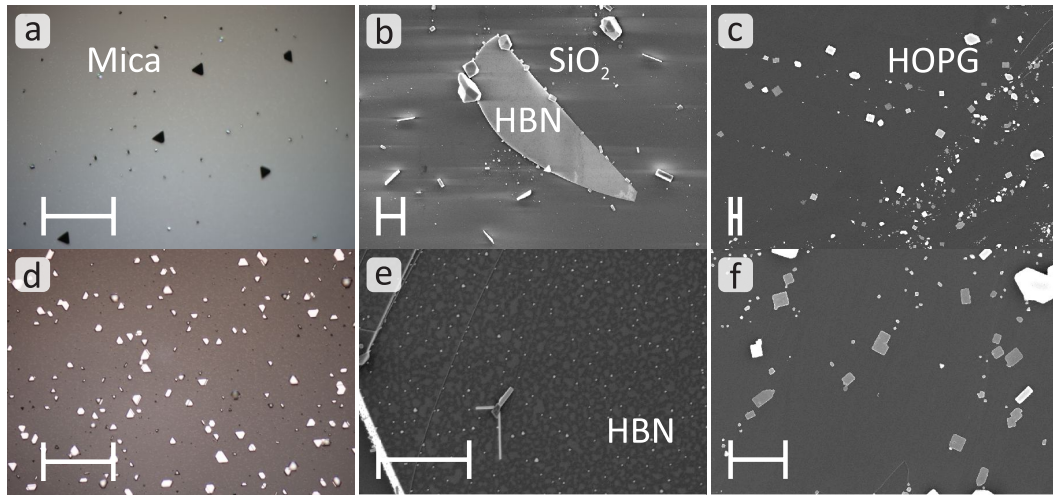
Fig. *3.3: Optical images and electron micrographs of various SnTe nanostructures, grown at 560 °C and 100 mTorr and 10 sccm Ar (left to right) on mica (a), HBN (b) and HOPG (c). Panel e) (f) is a zoom of panel b) (c). The image in panel d) shows nanoplatelets from a growth on mica with a rate of 120 sccm. Scale bar is 100 µm in a) and d), and 1 µm otherwise.*

4. Evacuating the system to a pressure below 10 mTorr and flushing it with pure argon. This step is repeated at least three times to remove residual O_2 and H_2O.
5. Adjusting the carrier gas flow and pressure inside the tube.
6. Initiating the heating process. The timer is started after the internal temperature sensor indicates that the target temperature is reached.
7. After the time is completed, carrier gas flow and pumping station are turned off, and the system is let to cool down naturally at a constant pressure.

The source material SnTe is purchased from ALFA AESAR. The chemical composition was verified by EDX and powder diffraction analysis. The bulk material can be easily crushed into powder.

For growth on bare Si/SiO$_2$ substrates, the middle zone of the oven is set to 550 °C, while the pressure at the tube end is set to 100 mTorr. Initially, a flow of 40 sccm and a growth time of 30 min were used, which resulted in cuboids of various sizes, as shown within the top row of Figure 3.2. In general, for too fast flow (> 60 sccm) and/or too high temperatures (> 560 °C set at the oven) SnTe nanostructures that are too thick for electrical contacting by e-beam lithography (EBL) are obtained. Lowering the flow to 10 − 20 sccm while maintaining the growth time and utilizing gold nanoparticles for VLS-growth, yields SnTe rods and wires with a diameter down to 40 nm. All these structures have a cap at their substrate remote end, as exemplified in the middle row of Figure 3.2, which testifies successful VLS growth. At a flow rate of 10 − 40 sccm, a pressure of 100 mTorr and a lower temperature of 490 °C, octahedral and square-like sheets are growing out of the substrate. While some of them can be identified

as single sheets, the majority consists of twinned structures (see Figure 3.2, lower right). The sheet thickness ranges between 50 nm and 1 μm, and their lateral size is several μm.

In order to obtain sufficiently thin sheets (thicknesses below 50 nm), epitaxial growth on different types of 2 D materials was tested. The latter included mica, hexagonal boron nitride (HBN) and highly ordered pyrolytic graphite (HOPG). As apparent from Figure 3.3, SnTe grows on mica in a highly oriented manner with a [111] bottom surface. Growth in this direction results in a pyramidal shape, with the bodies sharing one parallel edge. Attempts to obtain a closed film by increasing the flow to 120 sccm or the growth time to 24 h resulted in an increased thickness rather than an extended lateral growth. Even a merging of the pyramids could not be achieved.

No conditions were found that would allow for epitaxial growth of SnTe on HBN. For this type of substrate, growth preferably occurs on the Si/SiO$_2$ substrate rather than on the HBN flakes, as can be seen in Figure 3.3 b) and e). Even when Au nanoparticles are present during the growth, only tiny structures are formed on the HBN, while extended wires and sheets are found on the Si/SiO$_2$ substrate. Epitaxial growth of SnTe (at 550 $^{\mathrm{o}}$C , 10 mTorr and 10 − 20 sccm argon flow) on HOPG or exfoliated multilayer graphene yields ultrathin sheets with a [100] bottom surface and thicknesses of 7 − 10 nm. In contrast to mica, no preferred orientation was found. The growth mainly starts at edges and ripples of the underlying graphene.

3.1.1   TEM characterization of SnTe nanostructures

Like mentioned in section 1.2.2, SnTe does not exhibit any Raman modes at room temperature, thereby complicating the chemical identification of the grown SnTe nanostructures. Conventional chemical analysis methods like elementary analysis require several mg of material and thus cannot be used to determine the chemical composition of an individual nanosheet.

TEM offers the possibility to analyze the crystal structure by means of electron diffraction. In conjunction with energy-dispersive X-ray spectroscopy (EDX) the chemical composition can be determined within 5 wt-%. EDX data gained from various SnTe nanoplatelets and nanowires are collected in Table 3.1. The bulk material displays a close-to 1:1 stoichiometry. SnTe nanostructures transferred onto Si/SiO$_2$ substrate show a lack of tin, while on a TEM grid the expected stoichiometry is obtained. This difference is most likely due to the strong background of the Si/SiO$_2$ substrate. Hence, in order to enhance the interaction cross-section and reduce the background contribution, spectra were acquired with only 20 kV to reduce the X-ray emission.

The grown SnTe nanostructures are transferred to a *lacey carbon film* on a 400 mesh Cu-grid (ø = 2.3 mm) by sandwiching the grid between the growth substrate and a bare

Tab. 3.1: *EDX data in at% determined for different SnTe structures. Measurement was performed with a scanning electron microscope from Zeiss (Merlin) using 20 kV acceleration (first and second table sections), and with a TEM at 300 kV acceleration voltage (last section of table).*

	Sn	Te	Substrate
source material	50.0(9)	49.9(1)	-
platelet (not connected)	48.5(7)	53.2(4)	SiO_2
nanowire (not connected)	47.8(8)	51.4(3)	SiO_2
platelet (connected)	43.3(3)	56.6(7)	SiO_2
nanowire (connected)	46.3(5)	53.6(5)	SiO_2
platelet (TEM)	49.3(1)	50.6(9)	TEM-Grid
platelet (TEM)	50.4(1)	49.5(9)	TEM-Grid
nanowire (TEM)	49.0(7)	50.9(3)	TEM-Grid

substrate. For both the nanowires and nanoplatelets, atomic resolution is obtained with a Philips CM 30ST microscope (LaB6 cathode). The results of the EDX analysis are listed in Table 3.1.

The SnTe nanowires are found to grow along the [100] direction, as can be concluded from the electron diffraction pattern in Figure 3.4 a) and c). SEM images indicate that the wires have a quadratic cross-section. Moreover, EDX maps reveal that the caps at the nanowire ends consist of gold, and the presence of gold traces along the wire. The wire body exhibits a homogeneous composition of tin and tellurium.

The SnTe nanoplatelets grow in twinned morphology. Figure 3.4 b) shows the atomically resolved TEM image of a region with a twinned (top left) and a single crystal domain (bottom right). Evidently, in the twinned region the atomic resolution is lost due to a superposition pattern. In the electron diffraction pattern, this results in an additional set of reflexes and an altered intensity distribution. In contrast, by acquiring the pattern of a single crystalline domain (see the bottom right inset) and superimposing a pattern that is rotated by 37 ° , the twinned pattern becomes visible.
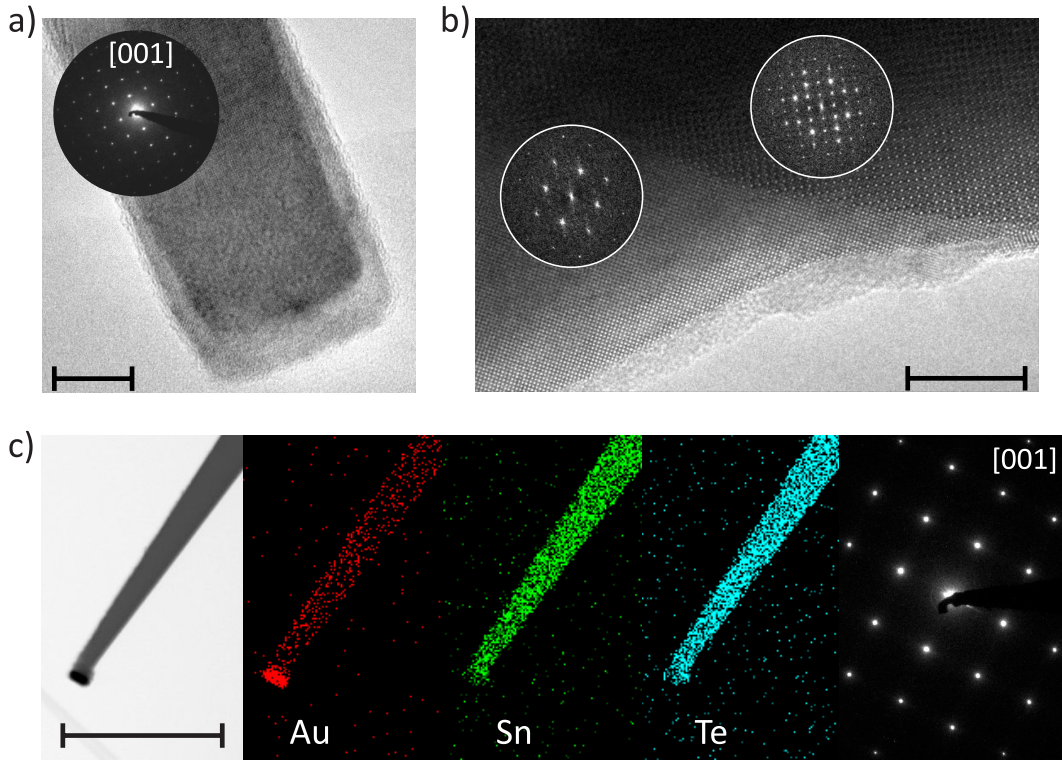
Fig. 3.4: Atomically resolved TEM image and electron diffraction pattern of a) an individual SnTe wire and b) a twinned SnTe platelet, both taken with 300 kV. Scale bar is 10 nm. c) TEM image (left) of the top of a SnTe wire, and corresponding EDX maps specific for Au, Sn and Te, respectively. The rightmost image shows the electron diffraction pattern of the wire. Scale bar is 100 nm.

3.2 Electrical Device Fabrication

The grown SnTe nanostructures are transferred to a Si/SiO_2 substrate equipped with a marker coordinate system by pressing the growth substrate onto the pre-heated marker substrate[4].

Graphene is obtained by the so-called *Scotch tape* method. To this end, an adhesive tape is used to thin down a cleaved piece of HOPG. In the last step, the tape is pressed onto a Si substrate with a thermally grown SiO_2 layer of 300 nm thickness. This thickness has proven to give the strongest optical contrast for monolayer graphene, such that it can be easily seen in an optical microscope [147]. The substrate has a marker system to identify the position of a flake (Figure 3.5). To increase the adhesion of the substrate, it is cleaned by an oxygen plasma treatment for at least 10 min with a power of 100 W and a gas pressure of 0.3 mTorr, and subsequent heating to 130 °C.

The overall structuring and contacting procedure relies upon e-beam lithography

---

[4]Substrates are cleaned in an O_2-plasma 100 W, 0.3 mTorr for 2 min and heated to 130 °C afterwards.
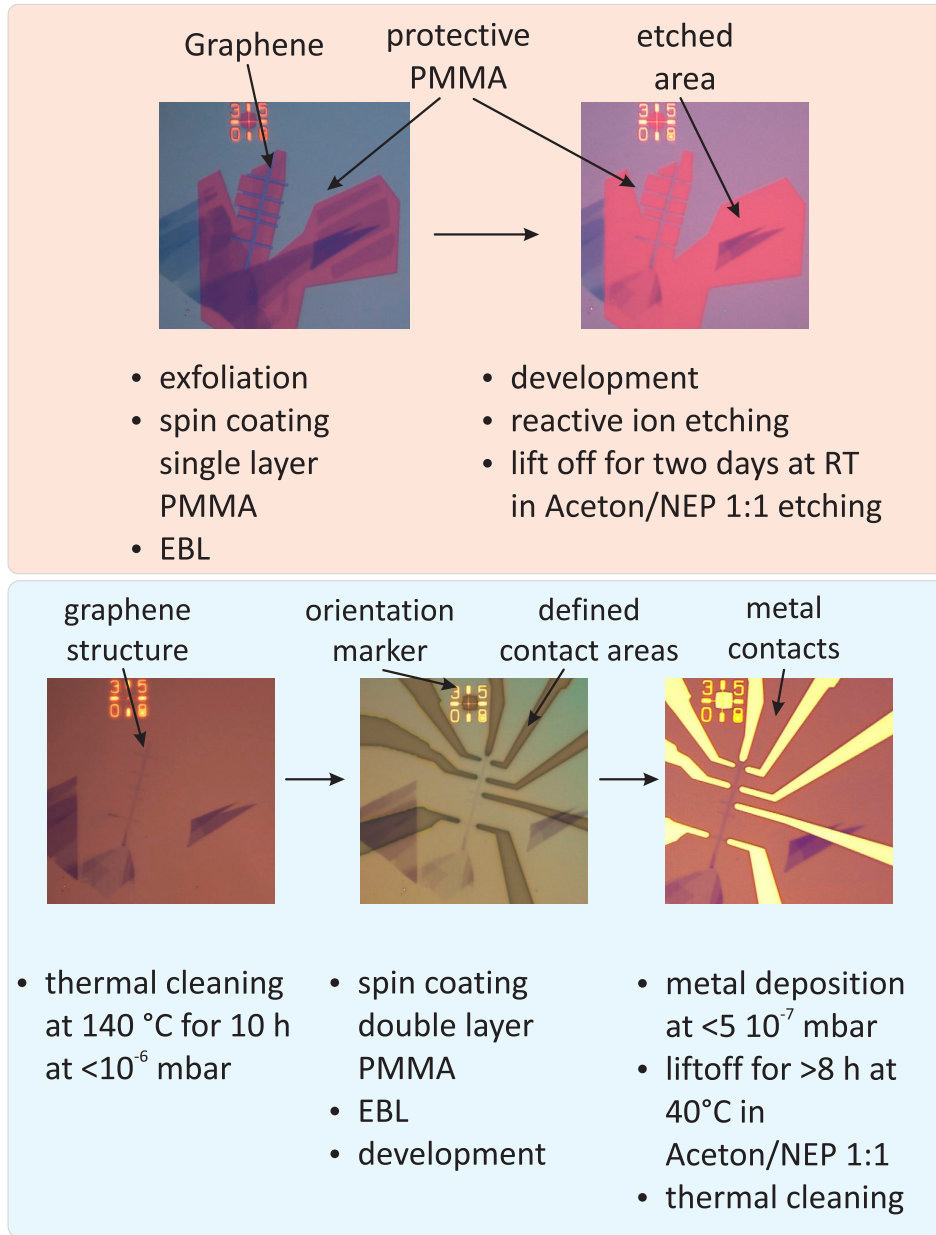
Fig. *3.5: Structuring (red box) and contacting (blue box) procedures used in the device fabrication. Structuring requires only a single layer of PMMA, while for contacting a double layer is used to facilitate the lift-off process after metal deposition. The underlying PMMA layer should be significantly thicker than the metal film deposited.*

(EBL), as outlined in Figure 3.5. In the first step, the marker substrate is screened under an optical microscope for potential flakes/wires. Subsequently, a poly-methylmethacrylate (PMMA) double layer is spin-coated on the substrate, followed by a baking step at $160\,^{\circ}$C for each layer. The thickness of the spin-coated film depends on the PMMA concentration and the speed of rotation. With the aid of the marker

system, the target structures are transferred to the E-line software[5] and the contact layout is drawn. In the writing process, the e-beam exposes the contact areas. The PMMA molecules get fragmented by the high energy electrons, and the resulting shorter chains render the PMMA more soluble.

For semiconductor structures the double layer consists of a 200 K-950 K stack, where the numbers refer to the average molecular weight of the PMMA. The advantage of high molecular weight PMMA is the high achievable contrast and the higher stability against Ar-plasma.

For graphene a 50 K-200 K double layer is used. The overall stack has a better lift-off performance, which leads to less PMMA residues on the graphene. To achieve the same EBL contrast as for the 200 K-950 K a higher acceleration voltage of 30 kV (vs. 20 kV) is used to attain a smaller cross-section for the interaction between electrons and the PMMA, combined with a larger penetration depth of the electrons into the silicon substrate. While the first effect ensures a higher clearance dose of the PMMA, the enlarged penetration depth reduces the number of electrons that backscatter into the PMMA. The latter, so-called proximity effect can be minimized by using the higher acceleration voltage [148, 149].

The exposed PMMA is developed in a 3:1 mixture of isopropanol and methylisobutylketone (MIBK) for 30 s. The electron dose during EBL exposure is adjusted such that this development time is sufficient for full removal of the exposed PMMA. Afterwards the sample is rinsed in clean isopropanol to remove the developer. Patterning of the graphene into stripes is accomplished by a 200 K PMMA single layer, which is used to protect the desired structures. The 200 K PMMA offers a suitable trade-off between stability during the etching process and solubility. The patterning is performed prior to the electrical contacting procedure (Figure 3.5). The areas to be etched are exposed and developed, and then etching is done in three cycles using the following parameters: Ar flow of 100 sccm, O_2 flow of 11 sccm with an overall pressure of p = 0.05 mbar for t = 5 s at P = 48 W. After each cycle, a pause of 10-20 min is made to allow the substrate to cool down. The remaining PMMA is then removed by immersing the sample in N-ethyl-2-pyrrolidon (NEP) for at least 48 h. Finally, it is heated in a tube furnace to 140 °C under vacuum ($< 1 \cdot 10^{-7}$ mbar) for at least 4 hours.

3.2.1   Metal deposition

The electrode metals are deposited by thermal evaporation in a vacuum chamber[6]. Titanium is used as an adhesion layer for the non-magnetic contacts ($\lesssim$ 1 nm) which are made of AuPd (60/40). This alloy yields metal films whose small metal grain size enables smooth edge formation during the lift-off process. The chamber is

---

[5]Is a brand of RAITH
[6]Univex by Oerlikon-Leybold or Vacuum chamber by Angstrom

evacuated overnight (> 12 h) to ensure a residual pressure of $\lesssim 5 \cdot 10^{-7}$. For graphene, the contact resistance is documented to decrease with the background pressure during metal evaporation, which is most likely due to enhanced desorption of surface contaminants [150]. In case of graphene, an electrode thickness of 30 nm is used.

For the SnTe nanostructures, the metal thickness is chosen to exceed the height of the nanostructure by at least 20 nm. To ensure Ohmic contacts, a contact pre-treatment is necessary. For this purpose, the developed sample is subjected to Ar-plasma (100 W at 0.3 mTorr for 90 s[7]), and then transferred as fast as possible to the vacuum chamber. This procedure results in contact resistances in the lower kΩ range. In the later stage, it became possible to perform an in-situ Ar-plasma process followed by direct metal evaporation without breaking the vacuum, such that contact resistances below 500 Ω could be achieved.

In case of the ferromagnetic contacts, special care must be taken during the fabrication. It turned out that only under very clean environment (i.e., low base pressure) electrodes showing anomalous magnetoresistance (AMR) can be obtained. Specifically, the base pressure for thermal evaporation should be below $1 \cdot 10^{-7}$ mbar, and the chamber has to be thoroughly cleaned before, in order to avoid contamination with other metals. Moreover, for the aim of preventing electrode oxidation, 10 nm Ti are evaporated against the closed shutter prior to ferromagnetic metal evaporation. During this process, the evaporation stage is heated up to release adsorbed water and oxygen which is then trapped by the evaporated Ti. The deposited ferromagnetic layer is capped with at least 5 nm of gold to avoid oxidation upon contact to the ambient.

Lift-off is done using a 1:1 mixture of NEP and acetone at 40 °C for at least 8 h. Residual metal films on the edges of the sample are removed with a toothpick in isopropanol. For nonmagnetic contacts to graphene, residues on the sheet are removed by subsequent thermal annealing, whereupon the contact resistance is reduced. For annealing, the sample is heated to 140 °C with a heating rate of 1 °C per min. This temperature is maintained for at least 4 h. During ramping up, the system is pumped to $1 \cdot 10^{-7}$ mbar. When the temperature is reached, Ar/H_2 (80/20) is introduced at a pressure of $1 \cdot 10^{-4}$ mbar. Owing to the catalytic activity of the Pd within the electrodes, good cleaning results are achievable in this manner[8] [151].

The substrates are glued with conducting silver paste into a chip carrier (see Figure 3.6 a) which allows for 19(+1) electrical connections[9]. Structures are connected to the chip carrier with the aid of ultrasonic assisted wedge bonding of gold wires.

---

[7]Te-Pla 100-E from Technics Plasma GmbH

[8]Evaluation is based on the field effect behavior and the lowest resistance that can be achieved by the device.

[9]The base is connected to one of the pins and allows to apply a voltage to the substrate.

3.3 Electrical measurement setup

For the low temperature magnetotransport studies, a ^{3}He-system was set up. It consists of a 70 l ^{4}He cryostat with a 66 l liquid nitrogen jacket and a 15 T magnet. The magnet can be swept at a maximum rate of 1 T per min. Two inserts are available; the first one is equipped with a rotatable sample chuck (Figure 3.6 a), while the second one hosts a fiber-based confocal microscope (CFM). The cryostat is suspended on mechanical springs to reduce interference from vibrational noise from the environment. Only the first insert is used within the present thesis work, while the cryostat is set up to work with both.

For electrical measurements the insert is equipped with a nonmagnetic home built chip carrier socket (orange) into which a commercially available chip carrier (blue) can be mounted that allows for 19 (+1) separate electrical connections. The chip carrier is compatible with square substrates of 5 mm edge length. The substrate is glued with conducting silver paste to the base plate which is connected to one of the pins. Connection to the outside (and room temperature) is made by a twisted pair constantan loom, which ends in a 24 pin Fischer connector at the top of the insert. The remaining four connections are used to connect a RuO temperature sensor close to the sample, which allows for precise temperature monitoring of the sample.

Temperature control is performed by the ITC 503 from Oxford, combined with four sensors and three cartridge heaters. Among these, Cernox sensors monitor the temperature at the 1 K pot, charcoal sorption pump and the ^{3}He pot. The latter is furthermore equipped with a RuO sensor to detect temperatures below 1.4 K. The heaters are placed in the surrounding of the temperature sensors, at the specific locations indicated in Figure 3.6 a). This configuration enables controllable measurements from 230 mK up to 10 K. Temperatures up to 300 K can be reached by pumping the sample space (IVC) to a pressure of $1 \cdot 10^{-6}$ mbar.

To reach the base temperature, the 1 K pot is pumped with a root pump[10], which is supported by a membrane pump. Vibrational decoupling of the pumps from the measurement setup is attained by a stainless steel body in conjunction with a sand box. Both are equipped with a NW-50 flange feed-through that helps to reduce vibrational noise from the pumping stage, which is especially important for the CFM insert. Electrical isolation from the pumps is achieved by a short plastic tube inserted into the pumping line. In addition, the pumps are placed in a metal box to reduce electromagnetic stray fields as well as noise disturbances.

---

[10]A100L from Pfeiffer
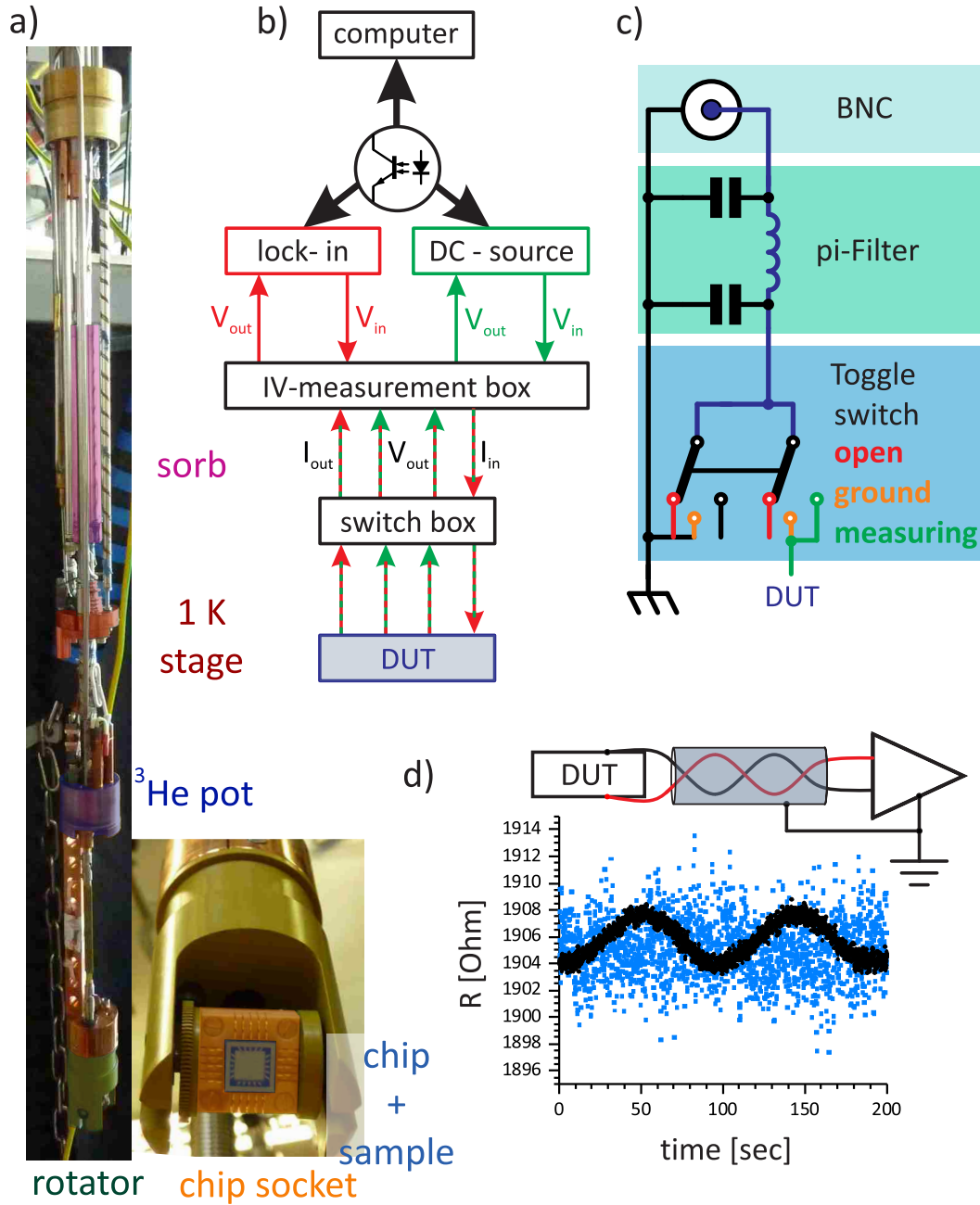
Fig. *3.6: a) HelioxVT insert with rotator extension and home-built chip socket. b) Schematic depiction of the electrical measurement connection, which is galvanically isolated from the PC. c) Internal components of the switchbox. d) DC measurements of the initial system (blue data points), performed with a long audio-grade cable, and after re-soldering the cable (black points). The white noise is reduced, while the 0.01 Hz frequency stems from vibrations of the system.*

3.3.1 Electrical connection

The main issue is the connection between the 24 pin Fischer connector and the measurement instruments. For the first testing of the setup, a long cable[11] is used

---

[11]Vandamme 268-224-060 Blue series Studio Grade Ver. 3.1

to place the switchbox inside a standard 19" rack in proximity of the cryostat. The switchbox consists of toggle switches and BNC connectors, as shown in Figure 3.6 c). In this way, the sample can be grounded upon making connections to the instruments. This offers the advantage of a flexible arrangement of the instruments and cables within the rack, and furthermore reduces interference by the magnetic field. However, the long cable tends to pick up vibrational noise, as demonstrated by the temperature trace in Figure 3.6 d), recorded using a RuO-sensor in a DC four point configuration[12]. The average resistance of $1905\,\Omega$ shows a sizable standard deviation of $2.1\,\Omega$. After re-soldering the connection (see the sketch above the plot), the noise (black) is significantly reduced, as apparent from the smaller standard deviation of $0.6\,\text{Hz}$ [152]. The remaining oscillation of $0.01\,\text{Hz}$ originates from mechanical vibrations of the suspension. This could be further reduced by damping the springs.

Optimum noise reduction was obtained by directly connecting the switchbox to the Fischer pin at the insert, and placing an amplifier stage (IV-measurement box) on the cryostat to reduce the cable length. The switchbox and amplifier stage are galvanically disconnected from the cryostat and computer (see Figure 3.6 b)) and supplied with a separated ground. Initially, the switchbox contained a pi-filter[13] to reduce high frequency noise transmission to the sample. However, in case of high Ohmic samples and current-driven measurements, these filters can act as a low frequency RC circuit, thereby making AC measurements impossible. Hence, a second box without filters was constructed. For the now much shorter connection to the amplifier stage $50\,\Omega$ miniature coaxial cables[14] are used. Their special structural design allows for less triboelectrical noise.

The amplifier stage[15] consists of a gate module with an output of $\pm 100\,\text{V}$, a constant voltage and current source (range 1 nA/V to 100 μA/V) that can be controlled by V_{in}, a current-to-voltage amplifier module ($1 \cdot 10^{10}$ V/A to $1 \cdot 10^4$ V/A), as well as a high impedance differential voltage amplifier ($1 - 1 \cdot 10^3$ amplification with $> 1\,\text{G}\Omega$ impedance)[16]. The latter component is particularly important for measuring nonlocal voltages, as low impedance voltage probes can influence the measurement outcome due to high sensing currents [153].

Furthermore, all signal entrances for controlling the stage are of high impedance ($10\,\text{M}\Omega$) to decouple the controlling instruments from the measuring circuit. Ground loops are eliminated by implementing one common ground for all circuits within the

---

[12]Keithley Delta-System

[13]4202-053 from Tusconix

[14]LN5001 from elspec

[15]The stage has been constructed and built in the electronic work shop of the Forschungszentrum Jülich. A high impedance differential amplifier stage as well as the battery power supply are developed inhouse.

[16]See Appendix for circuit layout

stage[17] and the power supply from batteries. Lock-in amplifiers[18] and DC-SMU[19], which serve to provide V_{in} and digitalize the measured voltages V_{out}, are connected via standard coaxial cables to the stage. The power supply to these instruments is provided by transformers that are connected to the same fuse. All digital connections to the instrumentation are galvanically separated from the computer by an opto-coupler. The latter is used to control and automatically run the experiments with the aid of LABVIEW software [154].

---

[17]The stage has an analog and digital ground that are disconnected from each other.
[18]LockIn 7230 from Ametek
[19]Keithley 2400 for sourcing and Keithley 2000 for measuring DC voltages

4 Chemically functionalized graphene

a)

b)

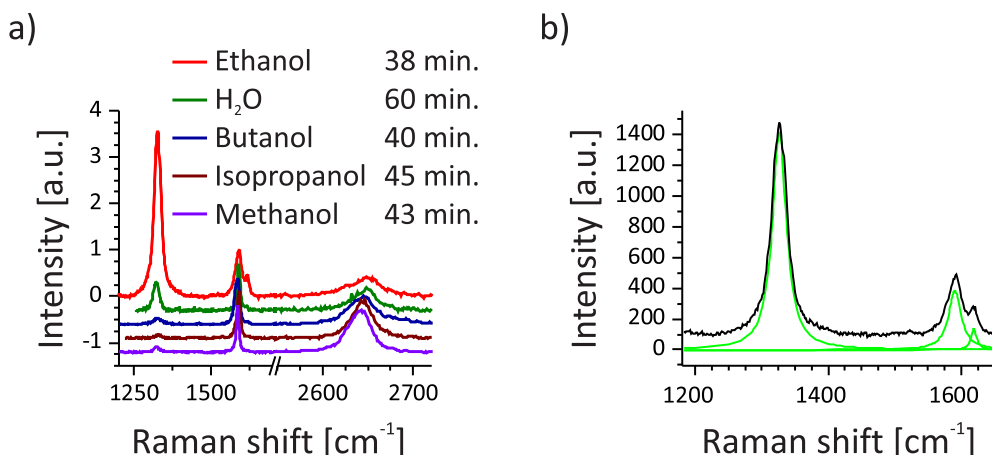**Fig.** *4.1: a) Raman spectra (λ_{exc} = 633 nm) of graphene subjected for 35 min to a solution of 4-nitrophenyl diazonium (NPD) tetrafluoroborate in five different solvents. All spectra are normalized to the G-peak and vertically shifted for clarity. The presence of the D- ($1325\ cm^{-1}$) and D'- ($1612\ cm^{-1}$) peaks signifies covalent bond formation. b) Fits of the D-, G- and D'-peaks with a single Lorentzian, respectively. For reaction in ethanol, this yields I(D)/I(D') = 10.5 and L_D = 8.8 nm.*

As described in section 1.3.4, the chemical functionalization of graphene with phenyl radicals[1] (derived from aromatic diazonium cations) introduces unpaired electrons that can give rise to a net magnetic moment [19]. Thus far, however, no magnetic signatures could be detected in magnetoresistance (MR) studies on diazonium-functionalized graphene [93, 155]. In all these works, the diazonium-based functionalization has been performed in acetonitrile or water, wherein the reaction rate is slow such that prolonged reaction times[2] are required. For graphene functionalized in this manner, a small increase of resistivity at the CNP (which is shifted to more positive gate voltages) and a Landau level (LL) broadening have been reported [93].

In order to identify the most suitable reaction conditions, first different solvents were tested with respect to the resulting reaction rate of nitrophenyl-diazonium ions with graphene. The typical procedure started with immersing the graphene flake in 18 M NPD solution for 30-40 min, followed by rinsing the sample with the corresponding solvent and finally isopropanol. The reaction extent is evaluated using the intensity of the D- and D'-peaks emerging in the Raman spectrum. Fastest reaction was observed for dry ethanol, as documented by the strong D-peak in Figure 4.1. Moreover, both spectra comprise a D'-peak, with a D/D' peak intensity ratio above 10, which is characteristic for the presence of sp^3 defects, as expected for covalent bond formation to the carbon framework of graphene.

---

[1]4-nitrophenyl diazonium tetrafluoroborate (NPD)

[2]20 h with a 10-20 M solution

4.1 Magnetotransport measurements

Graphene flakes are electrically contacted in Hall bar configuration (see Figure 4.2 a) without etching the sample as described in section 3.2. As a first step, the pristine flakes are electrically characterized to check their quality. From constant current lock-in magnetotransport experiments[3] performed at 1.4 K, the carrier mobility μ, mean free scattering time τ_m and quantum scattering time τ_q are determined in dependence of charge carrier concentration n_c in order to confirm the integrity of the flakes (following the outline of sections 2.2.3 and 2.2.4). From measurements of ρ_{xy} the charge carrier density n_c is extracted from a linear fit to ± 1.5 T and used to calculate μ. The devices described below showed a behavior in agreement with previous reports. In particular, the SdH-oscillations, as exemplified by Figure 4.5 a), emerge well above 3 T while localization effects are absent. Lowering the temperature from 280 to 1.4 K results in a resistivity decrease (see Figure 4.3 b) and 4.7 b)) with a minimum around 40 K (marked by grey line). The CNP of all flakes occurs between 0 V and 20 V, and the observed half integer LLs in σ_{xy} (as shown in Fig. 4.2 b) identifies the flakes as monolayer graphene.
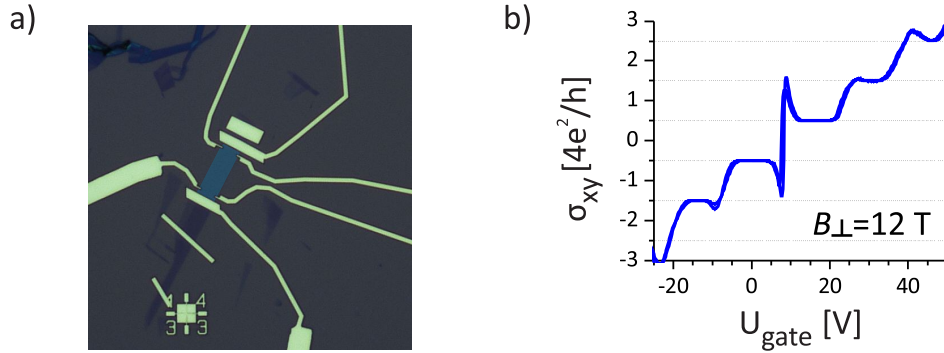
Fig. *4.2: a) Optical image of an investigated graphene device. The marker in the bottom left corner has a size of 9μm. b) Plot of σ_{xy} vs back-gate voltage under applied perpendicular B-field. The observed plateaus identify the flake as monolayer graphene. Overshoots at the plateau transitions are due to imperfections of sample geometry.*

Due to imperfections in the device geometry ρ_{xx} shows a slowly varying background which has to be taken into account when extracting the SdH oscillation minima. Background correction is done by fitting a polynomial of third order to the envelope (red line) of the SdH oscillations and subtracting the mean of the envelope (blue line) from the MR (as exemplarily shown in Figure 4.4 d) [106]. From the background-corrected MR trace τ_q is extracted as described in section 2.2.4.

---

[3]A current of 2-5 nA with 13 Hz is used.

After pre-characterization, the sample is removed from the chip carrier and immersed in a solution of NPD in dry ethanol[4] for a certain time. The reaction is stopped by rinsing the sample with 5 ml of dry ethanol. Subsequently, it is washed with isopropanol for one minute, and then blown dry with N_2. After gluing the sample into the chip carrier it is heated to $70\,^{\circ}C$ for more than 30 minutes to harden the glue and remove solvent residues. In the following, the magnetotransport behavior of graphene flakes subjected to two different reaction times is described.

4.1.1 Magnetotransport in weakly functionalized graphene

A graphene flake with a channel length of $9.7\,\mu$m and $1.1\,\mu$m width is immersed in 12.5 M NPD solution for 90 sec. The transfer curve in Figure 4.3 a) reveals a shift of the CNP by $\Delta U = +34$ V which is attributed to the electron-withdrawing nitro group (see section 1.10) on the NPD. In addition, the attachment of the phenyl radical goes along with an electron removal from the π-conjugated system of graphene. Besides the CNP shift, there is also an increase of resistivity. When the resistivity is plotted against the charge carrier density (Figure 4.3 c)) this increase becomes more evident and rules out a mere doping effect by adsorbates.

The mobility is decreased by a factor of four and its scaling with n_c changed from inverse to directly proportional. While the first is characteristic of graphene in the acoustic phonon scattering limit, the latter is associated with charge impurity scattering [156–158]. The high initial μ can be explained by the fact that the sample was heated to $140\,^{\circ}C$ at $< 10^{-6}$ mbar after the lift-off process, which is documented to not only remove residues on the graphene but also to reduce trapped charges in the underlying SiO_2 stemming from EBL [159].

The temperature dependent normalized resistivity $(\rho(T)/\rho(280\,K))$ of the functionalized flake (red), as can be seen from Figure 4.3 b), still displays metallic behavior like the pristine sample (blue). However, the resistance decrease is smaller for the functionalized sheet. Moreover, distinct changes of slope (marked by the grey line) occur at the same temperatures in both types of samples.

The strong decrease of τ_m in Figure 4.4 b) is caused by the functionalization, while it leaves the scaling behavior with respect to n_c unaffected. The much smaller τ_m also effects the onset of the SdH oscillations as disorder results in a broadening of the LLs. In contrast to τ_m, τ_q shows no clear trend after functionalization. The ratio τ_m/τ_q is reduced to ≈ 4, corresponding to roughly half of the initial value. The intial high value for the pristine flake indicates dominant long range scattering in forward direction. According to previous studies, a ratio of two is due to short range scatterers with a small scattering angle. For $1 < \tau_m/\tau_q < 2$ uncharged and > 2 charged scatterers are

---

[4]For this reason 99% ethanol is stored over activated $1\,\text{Å}$ molecular sieve to remove residual water traces.
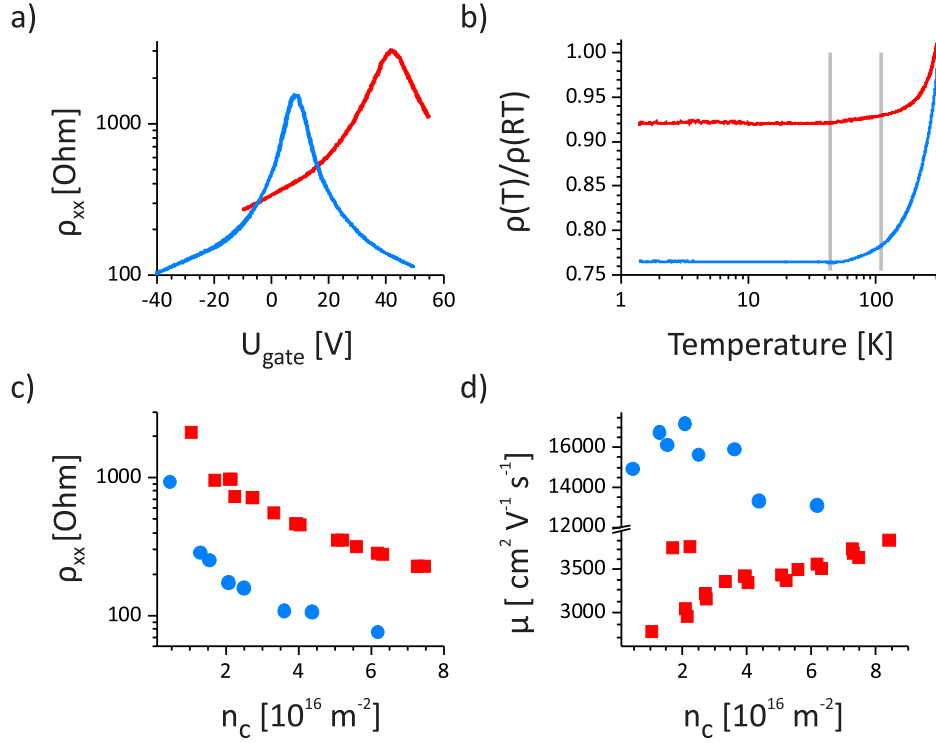
***Fig.** 4.3: a) Transfer curve of a graphene flake at 1.4 K before (blue curve) and after (red curve) 90 s of NPD functionalization. b) Temperature dependence of resistivity (normalized to RT) of the pristine (blue curve) and 90 s functionalized graphene (red curve). The vertical grey lines mark the changes of slope. c) Corresponding plots of resistivity (T = 1.4 K) as a function of carrier concentration. d) Corresponding plots of carrier mobility (T = 1.4 K) in dependence of carrier concentration.*

present [105]. Thus, it can be concluded that the functionalization introduces charged short range scatterers.

After the functionalization, the measurements at low magnetic fields reveal weak localization (WL) with an amplitude of $0.2 - 1\,G_0$[5]. As the quantum correction adds on top of the Drude conductivity it alters quantities like τ_m and μ which are calculated with $\rho_{xx}(B = 0)$. To remove these contributions, $\rho_{xx}(B = 0)$ is corrected by fitting the low field MR to a polynomial of third order, excluding the low field region where the localization effect occurs.

To remove the contributions of universal conduction fluctuations (UCFs), which are clearly visible in the plot of Figure 4.5 b), the MR is averaged over 17 different gate voltages in the range of $\pm 0.2 V_{\text{gate}}$. The averaged curve features a pronounced dip. By using equation 2.1, one obtains σ_{xx} which is fitted with equation 2.11[6].

Due to the sharp cusp and small signal, a high l_φ together with a strong inter-valley

---

[5]G_0 is the quantum of conductance and equals $2e^2/h$

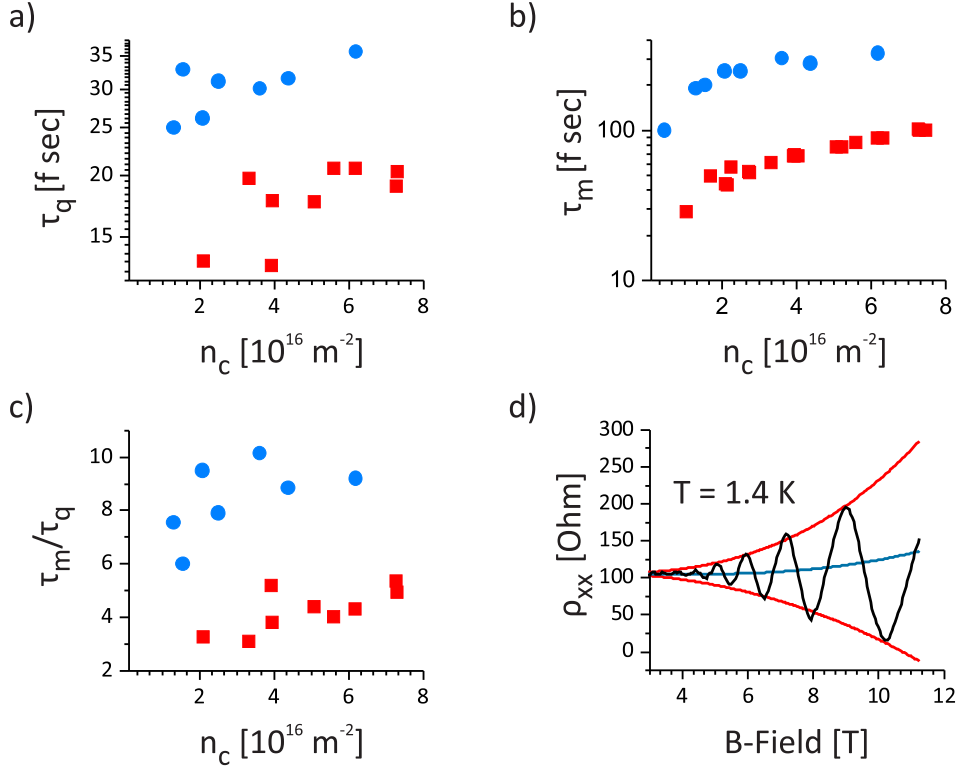[6]Fitting is done using Mathematica and Matlab [160, 161].

Fig. *4.4: a) Carrier concentration dependence of scattering time τ_q, extracted from the SdH oscillations, before (blue circles) and after (red squares) NPD functionalization of graphene for 90 s c. b) Corresponding plots of τ_m, derived from Hall measurements, against carrier density. c) Ratio of both scattering times in dependence of carrier concentration. d) SdH oscillations for the chemically functionalized graphene at $T = 1.4$ K. The background (blue line) is determined as the mean of the oscillation envelopes (red lines).*

scattering length l_i is extracted. While l_m (violet diamonds in Figure 4.6) is directly proportional to n_c the extracted length scales from the fit of the WL increases with decreasing n_c (Fig. 4.6 d).

All measured conductance curves show a negative magnetoconductance (MC) for B-fields above 50 mT (Fig. 4.5 b). This manifests itself by $l_\varphi \lesssim l_i$ as shown in Figure 4.6 d). Extrapolating this trend, l_φ should exceed l_i for $n_c > 10^{17} \mathrm{m}^{-2}$.

For three distinct charge carrier densities the temperature dependence is investigated. At lower densities, all extracted length scales exceed l_m. For the highest density studied ($7.5 \cdot 10^{16}$ m^{-2}) l_* is similar to l_m over the entire temperature range, suggesting that momentum relaxation is not the fastest process anymore. A weak temperature dependency of l_i results in a similar l_φ for the lowest temperature (Fig. 4.6 a-c), hinting
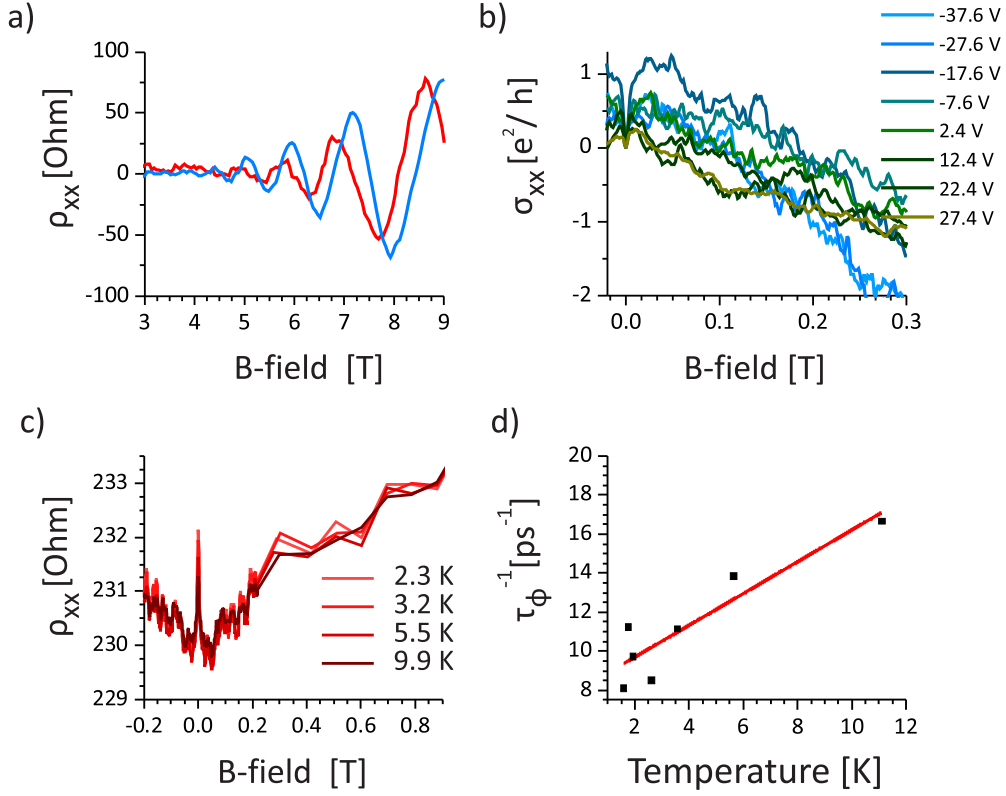
Fig. *4.5: a) SdH oscillations (T = 1.4 K) for two similar carrier densities in pristine (red line: $3.2 \cdot 10^{16}\ m^{-2}$) and NPD-functionalized graphene (blue line: $3.4 \cdot 10^{16}\ m^{-2}$). The functionalization reduces the amplitude resulting in lower τ_q. b) Low field magnetoconductance of the functionalized graphene, recorded at different back gate voltages. WL is observed with a small WAL contribution. c) Magnetoresistance of the functionalized graphene for $n_c = 7.5 \cdot 10^{16}\ m^{-2}$ at four different temperatures. The WL is decreased, and the independence of temperature indicates only minor electron-electron interaction. d) A linear fit of the extracted dephasing rate vs. B-field (for the same carrier density) using equation 4.1 yields $A = 0.85$.*

at a weak antilocalization (WAL) effect. For all experimental conditions,

$$\frac{k_B T \tau_m}{\hbar} < 1$$

holds as a benchmark for the interaction strength. In this regime, electrons experience many collisions with impurities during their interaction time $\hbar/k_B T$ with a second electron. The temperature dependency of l_φ follows

$$\tau_\varphi^{-1} = A \frac{k_B T}{2E_F \tau_m} \ln\left(\frac{2E_F \tau_m}{\hbar}\right) \tag{4.1}$$

where $\quad l_\varphi = \sqrt{D\tau_\varphi} \quad D = \frac{l_m \cdot v_F}{2} \quad$ and $\quad E_F = \hbar v_F \sqrt{\pi n}$
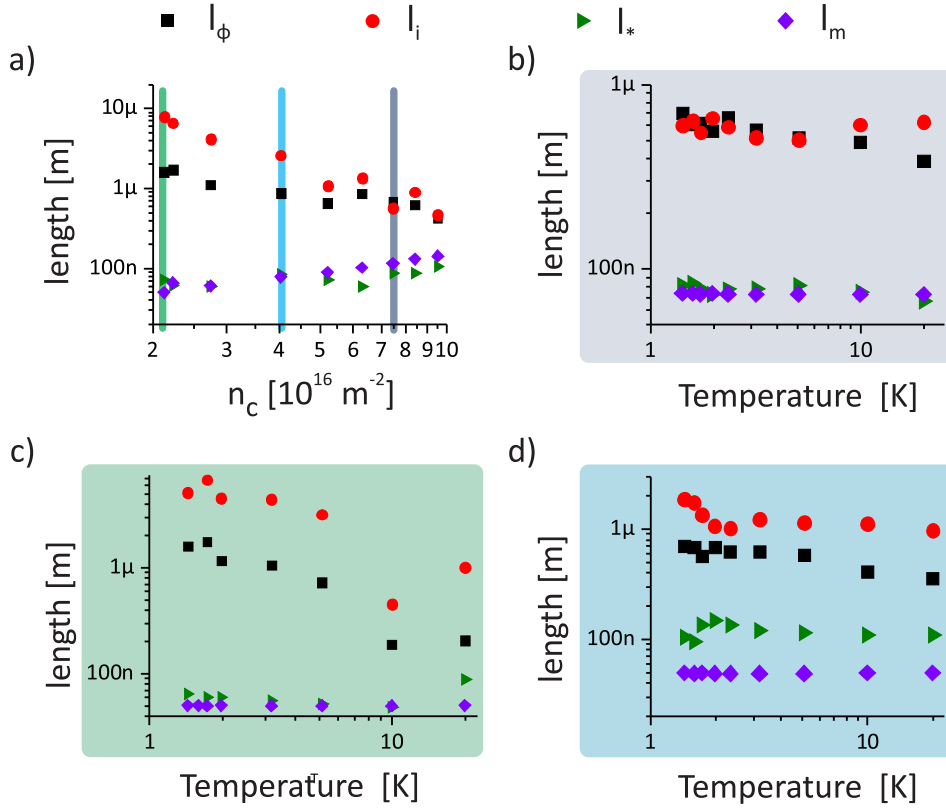
Fig. *4.6: a) Relevant lengths (see color code on the top), extracted from the fit to equation 2.11 as a function of carrier density. b-d) Corresponding plot in dependence of temperature. In addition, l_m is shown in all plots.*

are used. The fits yield A = 0.85, which is close to 1 in accordance with theory [113, 162, 163].

As all the MR curves overlap without any correction, a notable contribution from electron-electron interactions can be excluded and a correction of σ_{xx} is not necessary [113]. The above data demonstrates that the 90 sec. functionalization alters the electronic properties of graphene only slightly. After such short reaction time, only a small density of phenyl groups seem to be covalently attached and these groups mainly act as charged impurities. The gained MR data does not provide any evidence that the functionalization for the given reaction time introduces magnetic impurities. Furthermore, the phase coherence length experiences a substantial increase upon functionalization, such that it approaches the sample size. The resulting large inter-valley scattering length on the other hand, may originate from an enhanced spin orbit coupling as a consequence of the introduced sp^3 carbons. Theoretical calculations indicate that these carbons are associated with a dislocation in the z-direction of the lattice, which in turn leads to a higher spin orbit coupling [164].

4.1.2 Magnetotransport in strongly functionalized graphene

In a second series of experiments, the graphene functionalization time was increased to 900 sec. Like for the shorter treatment, the CNP after functionalization is shifted to more positive gate voltages ($\Delta U = +49\,V$). The conductivity at the CNP is lowered to 2.6-3.4 G_0 after functionalization, which is almost half of the value observed for the 90 sec. functionalization.

The temperature dependence of ρ_{xx} changes drastically after the functionalization, as reflected by the only small decrease until 180 K in Figure 4.7. For lower temperatures, a semiconductor-like behavior emerges. There appear three distinct changes of slope at 190 K, 40 K and 4 K, respectively (each marked by a grey line). The data points at higher temperatures can be correlated with change of slopes of the pristine flake. Moreover, the point at 4 K suggests the onset of electron-electron interactions that modify the MR.

Raman spectra acquired with $\lambda = 532\,nm$ display sizable D and D'-peaks, signifying
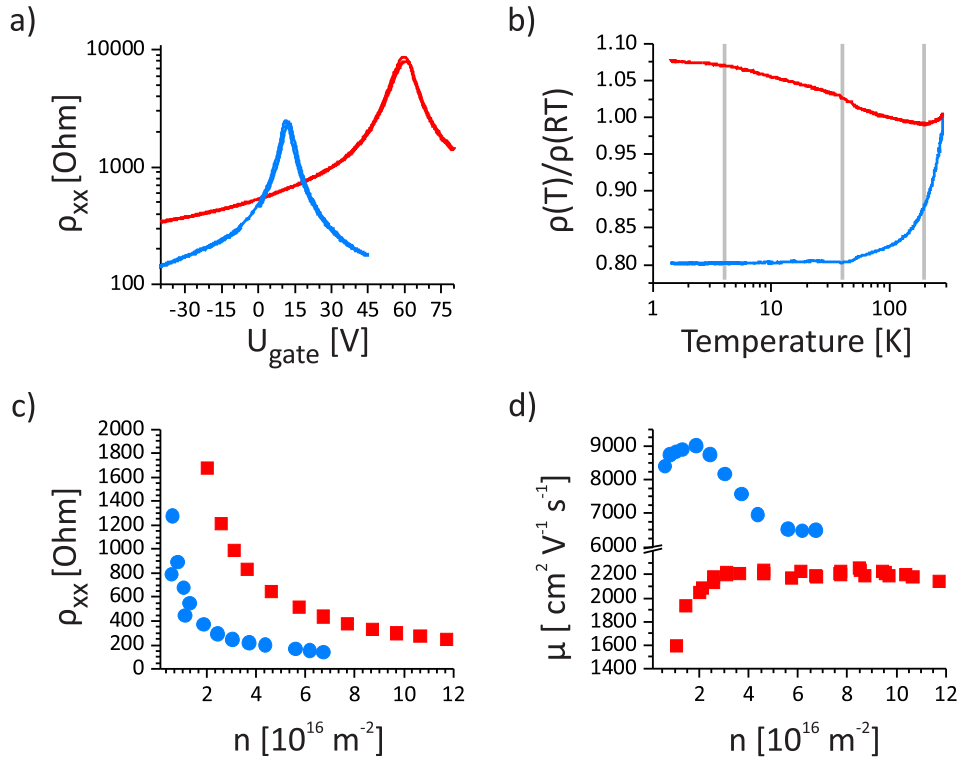
Fig. *4.7: a) Transfer curve for the pristine (blue curve) and strongly functionalized (red curve) graphene (T = 1.4 K). b) Normalized resistivity as a function of temperature for pristine (red curve) and functionalized (blue curve) graphene. The vertical grey lines mark changes in the slope at 4 K, 40 K and 190 K, respectively. c) Corresponding plots of resistivity vs. carrier density. d) Corresponding plots of carrier mobility as a function of carrier density.*
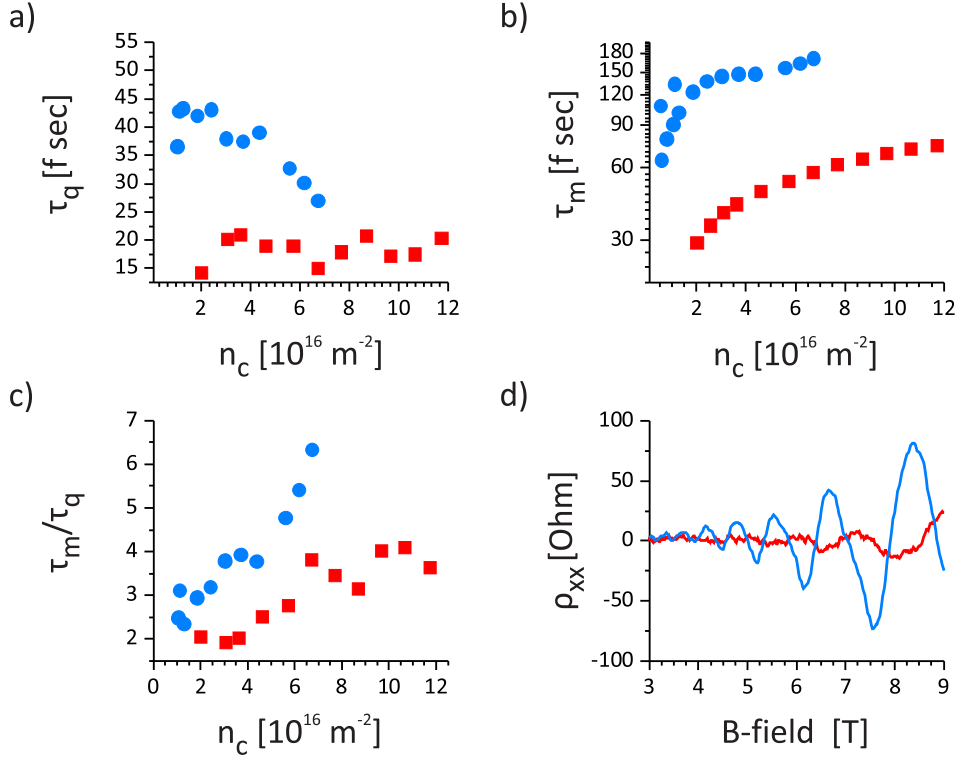
Fig. *4.8: a) Quantum and b) transport scattering time as a function of carrier density for the pristine (blue curve) and functionalized graphene (red curve). c) Corresponding plots of the ratio of the two scattering times vs. carrier density. d) Background corrected magnetoresistance trace for $n_c = 3.4 \cdot 10^{16}\,m^{-2}$ in functionalized graphene.*

the presence of lattice distortions (Fig. 4.10 a). The D/G intensity ratio between 0.91 and 1.12 yields an average L_D of 11.9 nm. This corresponds to one impurity per 112.2 nm^2 which is equivalent to one impurity per 4282 carbon atoms or a coverage of 0.023 %.

In this set of experiments, pristine flakes showed signatures of charged impurity and acoustic phonon to scattering contributions in the μ vs n_c plot (see Figure 4.7 d). This finding is attributable to the omission of the bake-out step after lift-off, as a consequence of which trapped charges remain close to the surface. For the longer functionalization, μ is reduced even further compared to the 90 s case. As n_c increased up to $3 \cdot 10^{16}\,m^{-2}$ μ increases. For higher n_c, μ remains nearly constant at 2100 cm^2 V^{-1} s^{-1}, which is indicative of pronounced charged impurity scattering or the introduction of mid-gap states [165].

For the strongly functionalized graphene, not only the onset of the SdH oscillations is shifted, but also their amplitude strongly reduced (Fig. 4.8 d). The extracted τ_q values are thus reduced by a factor of two to three (Fig. 4.8 a) and are nearly constant for the explored range of n_c. The dependency of τ_m on n_c is different as well, as apparent
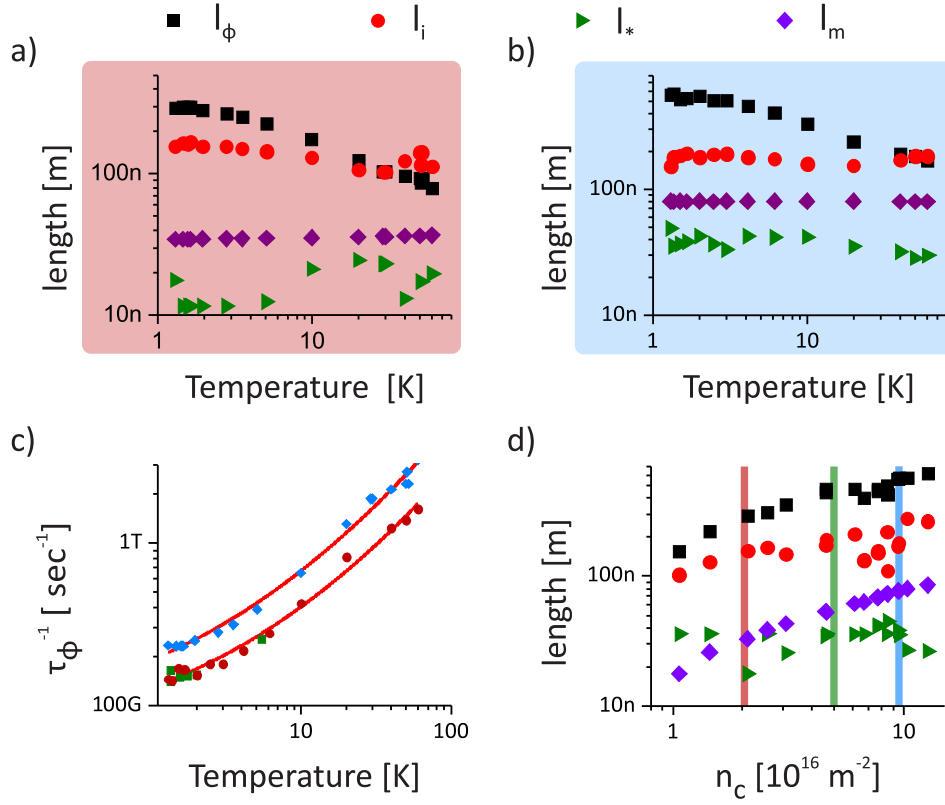
Fig. *4.9: (a-c) Temperature dependence of the relevant lengths (see color code on the top) for the 900 s functionalized graphene. The data are extracted from fits to equation 2.11. The carrier density is $n_c = 2 \cdot 10^{16}\ m^{-2}$) in a), and $n_c = 9 \cdot 10^{16}\ m^{-2}$ in b). c) Phase coherent scattering rate as a function of temperature, fitted with a polynomial of second order (red line). d) Carrier density dependence of the phase coherence and intra-valley scattering length. Both show the same square root dependency as the mean free scattering length.*

from a reduction by a factor of 2 along with a flattening. The corresponding ratio is reduced to almost half of its initial value and now close to two. This observation strongly points toward the relevance of charged short range scatterers [105].

At low B-fields, WL can be observed which is substantially enhanced in comparison to the shorter functionalized samples, and manifests itself by a signal on the order of one to two G_0 (Fig. 4.10 c). Moreover, the present sample does not show negative MC in the range of ±300 mT, which reflects notably shorter intra- and inter-valley scattering times. The latter shows, similar to l_φ, the same dependency as l_m on n_c (Fig. 4.9 d). Here, l_m has been corrected, as the resistivity is altered by the WL.

For two distinct n_c values (as marked in Figure 4.9 d)) a full temperature dependency was recorded (Fig. 4.10 d). While l_m, l_* and l_i are only weakly temperature dependent, l_φ displays a strong dependency (Fig. 4.9 a-b). Remarkably, for the latter quantity, there occurs a change of slope which is at the same temperature as seen in the cool-

down curve. It becomes better visible when plotting τ_φ^{-1} (scattering rate) against T, as illustrated by Figure 4.9 c). While for higher temperatures a linear dependency can be seen, the scattering rate levels off below 2 K. The red line is a data fit by a polynomial of second order, with the constant section marking the saturation time of $\tau_\varphi(n_c = 9 \cdot 10^{16} \, \mathrm{m}^{-2}) = 7 \, \mathrm{ps}$ and 5 ps for the lower charge carrier density.

Saturation behavior of the phase coherence time has been observed in the present work for in total two different samples. Various explanations have been reported in the literature for different types of graphene samples. As one option, the change of slope has been accounted for by the phase coherence length being close to the sample size [162]. The present sample is 1.9 μm wide and 8.5 μm long, and thus much larger than the extracted phase coherence length of 200 nm at the lowest charge carrier density. The above explanation can furthermore be ruled out by the fact that the saturation value changes with charge carrier density.

An alternative explanation involves Joule heating due to significant measuring currents, which raises the electronic temperature well above the substrate temperature. In Figure 4.10 b) back-gate sweeps are shown for measurements currents in the range of 2-40 nA. While the data belonging to 2 nA and 10 nA are mostly coinciding, a reduction of resistivity at the CNP for the 40 nA sweep due to Joule heating is apparent[7]. It hence follows that the measuring current of 2 nA at 1.3 K is insufficient to heat the sample. Microwave radiation picked up by the measuring lines can be largely ruled as a source of heating, as the system is equipped with appropriate π-filters [166].

A common cause of saturation not only in graphene are magnetic impurities [167]. In the presence of the latter τ_φ has to be replaced by an effective time $\tau_{\varphi,s}$ which comprises the phase coherence time and spin flip time. Following MATTHIESSEN's rule

$$\frac{1}{\tau_{\varphi,s}} = \frac{1}{\tau_\varphi} + \frac{1}{\tau_s} \tag{4.2}$$

a temperature independent τ_s will eventually become smaller than τ_φ as $T \to 0$ leading to a saturation of $\tau_{\varphi,s}$ [113, 168]. In the specific case of graphene, not only magnetic impurities can give rise to such behavior, but also the presence of spin orbit coupling (SOC). However, SOC should favor the emergence of WAL instead of the observed WL. It has been shown by theory that a z-symmetric system with SOC leads to WL with a saturation of $\tau_{\varphi,s}^{-1}$ for $T \to 0$ [167]. This scenario is inconsistent with the supposed attachment of phenyl radicals to only the top face of the graphene sheet, which is rather expected to destroy the z-symmetry. Nonetheless, a z-symmetric SO term in the theoretical framework might be amplified by asymmetrical impurities, provided that they introduce sp^3 hybridization [164, 167].

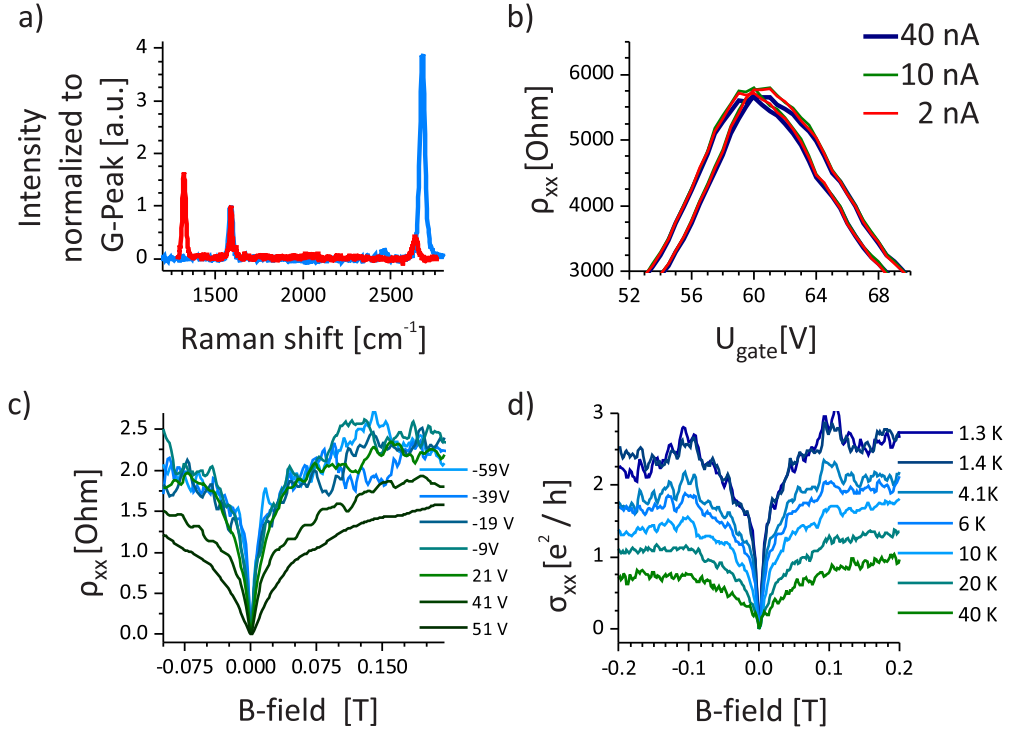[7]The heating power scales as $P = U \cdot I = R \cdot I^2$.

Fig. *4.10: a) Raman spectrum of a pristine (blue) and functionalized (red) graphene device, acquired with $\lambda = 532\,nm$. b) Corresponding back-gate dependence of resistivity for different I_{rms} to investigate the effect of current heating. c) Gate dependence of ρ_{xx} vs. B-field for the functionalized graphene at 1.3 K. d) Temperature dependence of σ_{xx} for $n_c = 9 \cdot 10^{16}\, m^{-2}$ in the functionalized graphene.*

A saturation of the l_φ has also been reported for graphene decorated with Pd clusters [169]. In this case, zero-point fluctuations have been invoked to explain the saturation behavior. This model assumes a disordered metal [114, 170] and could therefore be applicable also to the present functionalized graphene. However, at the present stage, it is only possible to convincingly prove the introduction of scattering centers which cause disorder in the graphene lattice. A full proof for the presence of magnetic impurities might be gained by applying a constant in-plane B-field while sweeping the out-of-plane B-field. If magnetic impurities are present the saturation behavior should alter with the strength of the in-plane B-field [167].

4.2 Spin transport

A major challenge in electrical spin transport experiments is the conductivity mismatch at the ferromagnetic metal/graphene interface. This problem can be overcome by increasing the contact resistance [129]. One strategy involves the use of a tunnel barrier between graphene and the ferromagnetic electrode, whereby the spin

injection rate is enhanced while the spins are prevented from diffusing back into the ferromagnetic electrode [130].

In semiconductor spintronics, tunnel barriers have been made from different oxides including Al_2O_3, MgO, HfO_2 and SiO_2. The deposition techniques range from atomic layer deposition (ALD) over molecular beam epitaxy (MBE) to plasma-assisted oxide growth and sputtering [14]. In general, the barriers need to fulfill several criteria to attain good device performance [14]. These are:

- uniform and planar growth with good thickness control
- low density of defects or trapped states
- inertness towards the ferromagnetic metal and semiconductor
- low resistance-area product to minimize the power consumption of the device.

Research on graphene-based spintronics has focused on oxide-based tunneling barriers formed by deposition of metals followed by oxidation [134, 171], ALD or e-beam assisted deposition of MgO [135]. A major complication is the strongly hydrophobic character of graphene. Accordingly, instead of a uniform growth, oxides deposited on graphene tend to form clusters or islands. Thus, such layers must be quite thick to exclude pinholes.

One solution for the wetting problem is to pretreat the graphene. In the case of ALD, a pretreatment with NO_2 or O_3 as well as an adsorption of a monolayer of perylene tetracarboxylic acid (PTCA) has been reported to yield a closed and uniform oxide layer on graphene for deposition temperatures below $100\,^{\circ}C$ [172–175]. Alternatively, the deposition and gradual oxidation of reactive metals like Al provides access to uniform oxide layers via MBE [176, 177].

4.2.1 Spin valves with tunnel barriers

As ALD of Al_2O_3 enables a precise control of the oxide thickness it is the natural choice for the fabrication of oxide barriers. As described above graphene is first decorated with PTCA molecules following the protocol in reference [174] in order to improve the wetting capability of graphene. A Cambridge Nanotech ALD system with trimethylaluminum (TMA) and H_2O as precursors was used at $100\,^{\circ}C$ and a base pressure of 10 mTorr. The pulse sequence has been adapted from reference [174]. These parameters result in a growth rate of 0.12-0.16 nm/cycle. Figure 4.11 depicts a graphene flake, which was subjected to 25 cycles of ALD either performed over the entire area (panel f), or through a patterned PMMA mask (panel e), in order to obtain a global or local oxide barrier, respectively. The absence of a uniform oxide layer most likely arises from a too low density of PTCA on the graphene. For ALD through the PMMA mask, a templating effect of the PMMA can been seen.

This is due to the diffusion of the two precursors into the PMMA where they react to form a sponge which is difficult to lift-off [178]. Increasing the numbers of cycles
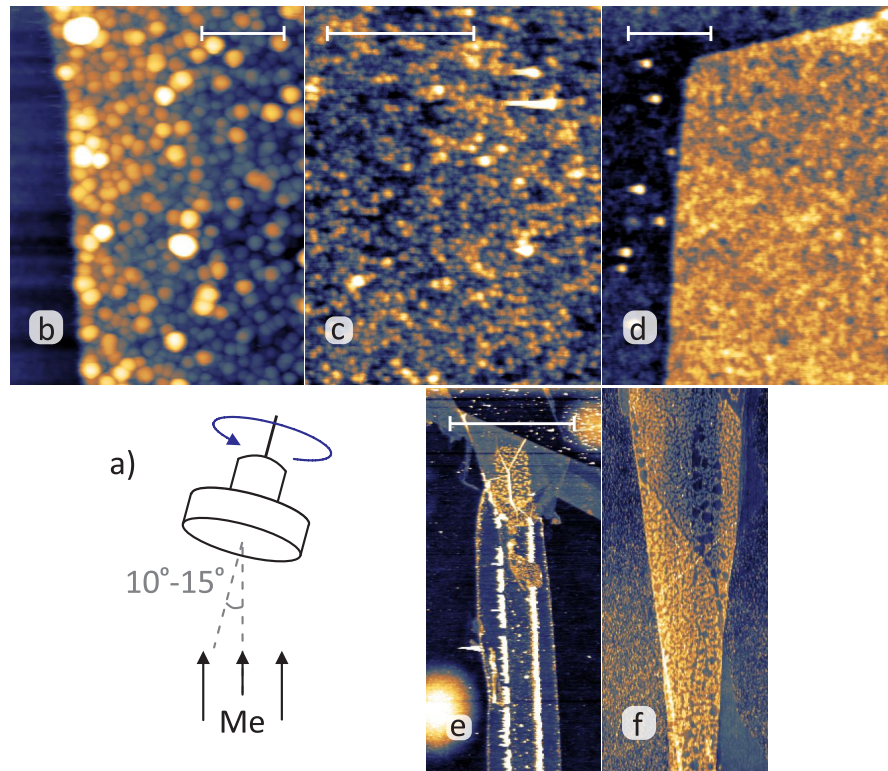
Fig. *4.11: a) Schematic sketch of the metal (Me) deposition under an angle while rotating the sample. (b-f) AFM images of graphene covered by Al or Al/Al$_2$O$_3$. b) Aluminum deposition with 1 Å/s on graphene results in a buckled film. c) Smaller bubbles are visible for room temperature deposition rates of r = 0.5 − 0.8 Å. d) Cooling the sample to liquid nitrogen temperatures results in a smooth film for an Al deposition rate of 1 Å/s. (e,f) 25 cycles of Al$_2$O$_3$ ALD on Al-coated graphene with (e) and without (f) a PMMA mask. As the alumina nucleates uniformly, the shape of the window in the PMMA mask is maintained. Scale bar is 400 nm in (b-d), and 5 µm in (e).*

enhances this templating effect and the resulting sponge can only be removed by ultrasonication. Accordingly, ALD does not represent a suitable option for local oxide barrier formation.

As an alternative approach, Al is deposited under an angle of 10° on the graphene, followed by an oxidation step. The resulting film is very rough, as apparent from Figure 4.11 b). Decreasing the deposition rate reduces the roughness to some extent. A highly uniform Al$_2$O$_3$ film can be achieved by cooling the sample to liquid nitrogen temperature during the Al depositing with a rate of 1Å per second followed by oxidation at $200\,^oC$ (d). However, as PMMA has a glass temperature on the order of $100\,^oC$, this procedure is not compatible with a PMMA mask.

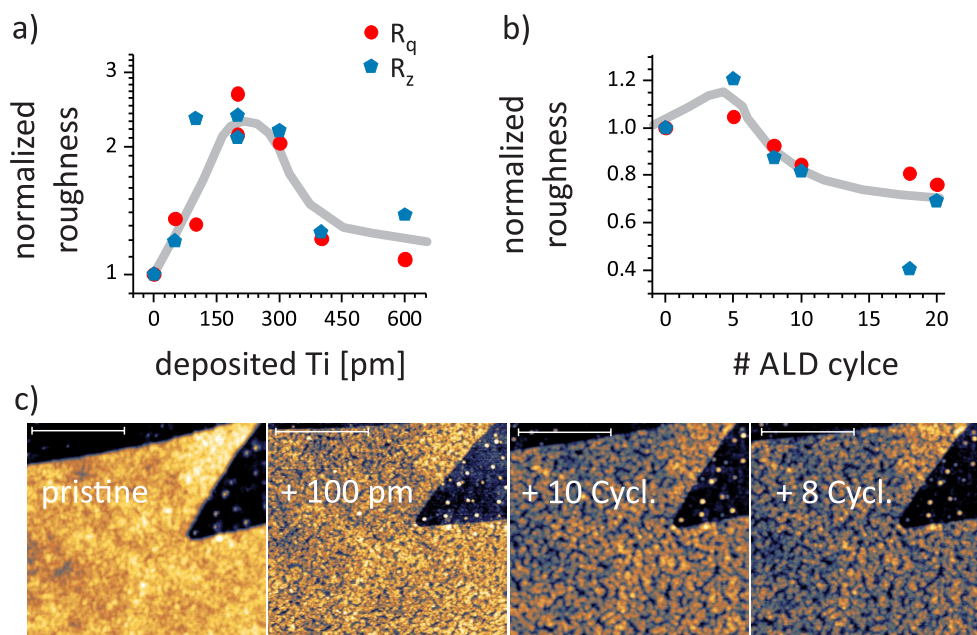In further experiments, Ti is used instead of Al as a metal. It is able to wet graphene

Fig. *4.12: Roughness parameters extracted from AFM measurements for a) different thicknesses of deposited Ti and b) different numbers of alumina ALD cycles on top of the Ti film. Parameters are normalized to the pristine (metal) values in panel a) (b). The grey line is a guide for the eye. c) AFM images of a graphene flake in its pristine form, and after decoration with a 100 pm Ti film and two consecutive steps of alumina ALD. Metal thickness is monitored with a quartz crystal calibrated for the deposition of 100 nm.*

and can be easily oxidized as well [175]. In Figure 4.12 c), the surface morphology of a pristine graphene flake is compared to the same flake after deposition of 100 pm Ti. Deposition was done in a standard UHV system with a base pressure of 10^{-7} mbar while rotating the sample under an angle of $10\,^{\mathrm{o}}$ (see Fig. 4.12 a). The extracted roughness parameters (R_q and R_z) plotted in Figure 4.12 a) and b) are normalized with respect to the pristine case. From them, it is evident that small amounts of deposited Ti do not form a closed film, which is manifested by an increase of all roughness parameters. After deposition of 200-300 pm Ti the mean roughness decreases, indicating the closing of the film. Importantly, as the extracted roughness parameters strongly depend on the quality of the AFM tip, care was taken to avoid blunt tips.

After the oxidation step, the pinholes in the metal oxide film are closed with the aid of ALD[8]. The evolution of roughness, normalized with respect to the metal film, is documented by the AFM images in Figure 4.12 c). After five cycles, all roughness

---

[8]At 100 mTorr and 100 °C one cycle consists of 0.1 s/40 s and 0.1 s/15 s pulse/purge time for H_2O and TMA respectively and results in 0.12 nm oxide.

parameters are decreasing with the number of ALD cycles, which testifies the creation of a spatially homogeneous oxide film.

4.2.1.1   Extended sheets with tunnel barriers

Graphene spin-valves with oxide barriers are fabricated as described in section 3.2 with two sets of contacts. In addition to the tunneling contacts (oxide + Co) at least two direct contacts were defined according to the design in Figure 4.13 b). The aim is to ensure a stable electrical connection to the graphene flake and correspondingly a well-defined local electrical potential, which is required as reference for all sourcing and gating voltages and to avoid signal fluctuations.
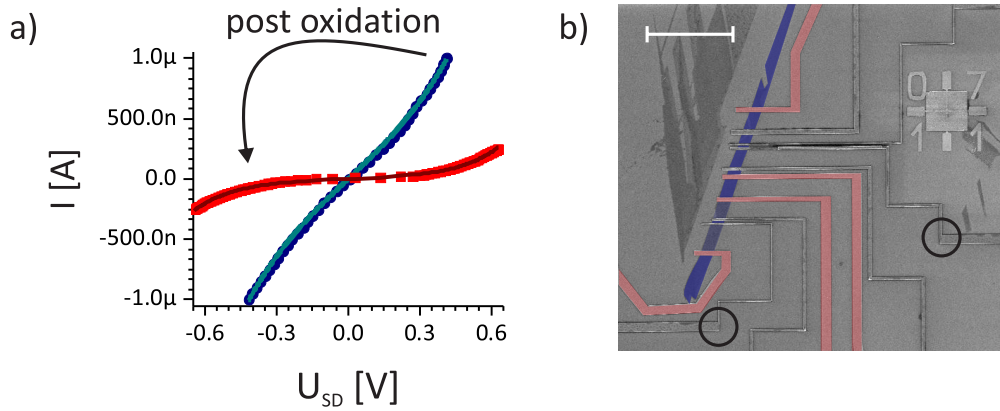
Fig. 4.13: a) I-V characteristics for contacts with a barrier made of 1.4 nm Ti and 10 cycles of alumina ALD, recorded before (green curve) and after oxygen treatment (red curve). Solid lines are fits to eqn. 4.3. (b) Electron micrograph of a measured graphene (blue) spin-valve device, comprising decoupled Co and direct AuPd (red) contacts. 90° turns (marked by black circles) are used to decouple wide from narrow Co sections and stabilize coercive fields. Scale bar is 10 µm.

Based upon AFM investigation, a seeding layer of 1 nm Ti followed by 10 cycles of ALD[9] was used for the oxide barrier. After depositing Ti, the device was exposed to ambient environment and further processed the next day. Unfortunately, this barrier composition did not yield the expected spin-valve behavior, despite the observed nonlinear source-drain (S-D) I-V characteristic (see blue line in Figure 4.13 a)). Fitting the curve to the SIMMONS model for tunneling current

$$I(V_{SD}) = \frac{Ae^2}{(2\pi d)^2\,\hbar}\left[\left(\frac{\phi}{e} - \frac{V_{SD}}{2}\right)\exp\left(-2d\sqrt{\frac{2em_e}{\hbar^2}\left(\frac{\phi}{e} - \frac{V_{SD}}{2}\right)}\right)\right]$$

---

[9]One cycle is expected to result in 0.12-0.14 nm Al_2O_3.
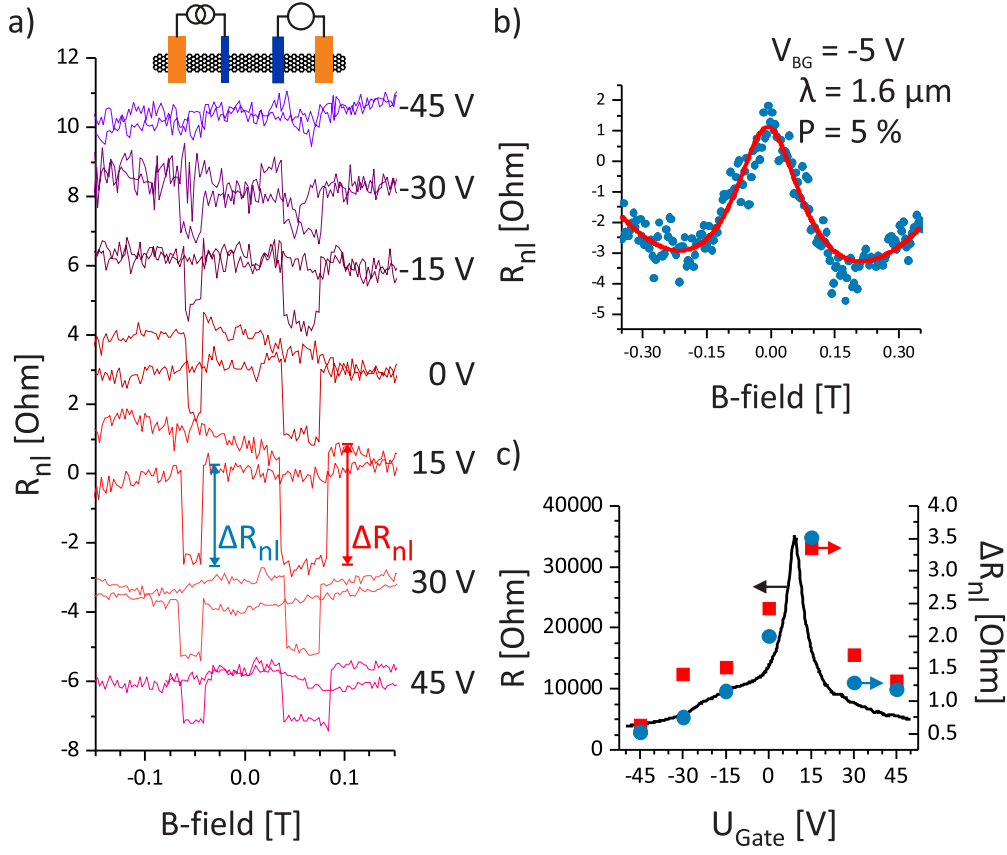
Fig. *4.14: a) Spin-valve signal of a pristine graphene device like in Figure 4.13 for different back-gate voltages (T = 1.4 K). The curves are vertically offset for visibility. Contact separation is 800 nm for all contacts. Drain contact and voltage probe V_B are made out of Au. b) Hanle curve measured at T = 1.4 K on the same device with a different contact configuration. The fit to equation 2.24 (red line) provides the spin life times. c) Comparison of the local resistance and nonlocal resistance change (derived from panel a) as a function of back-gate voltage.*

$$-\left(\frac{\phi}{e} + \frac{V_{SD}}{2}\right)\exp\left(-2d\sqrt{\frac{2em_e}{\hbar^2}\left(\frac{\phi}{e} + \frac{V_{SD}}{2}\right)}\right)\Bigg]$$

(4.3)

provides the barrier height ϕ and thickness d as fitting parameters [179, 180]. For the above device, the extracted thickness is 1.3 nm which is close to the thickness expected for 10 cycles of ALD. This agreement signifies that Ti does not at all or at least not fully oxidize to TiO_2 [181, 182].

A stack of the same height as before, but with the oxidation performed in pure oxygen atmosphere at 0.3 mTorr for ten minutes, again resulted in a nonlinear I-V curve (red squares in Figure 4.13) from which a thickness of 2.4 nm is derived. This value is approximately the sum of heights of the Ti and Al_2O_3 deposited by ALD, indicating

that the Ti is at least partially oxidized. Unexpectedly, this device did not exhibit any spin-valve effect.

To ensure a full oxidization of the Ti, in further experiments the deposition is done in steps of 100 pm, each of which is followed by flushing the evaporation chamber with pure oxygen and maintaining the pressure above $1 \cdot 10^{-1}$ mbar for 10 min until the desired height is reached. Afterwards the sample is placed in an oxygen atmosphere (0.3 mTorr pressure) for at least one hour.

Reducing the oxide height to 0.3 nm Ti plus 0.6-0.7 nm Al_2O_3 (5 cycle ALD) finally resulted in devices displaying a spin-valve effect. MR curves acquired from one such device by sweeping the in-plane B-field are shown in Figure 4.14 a). A two-step spin-valve effect is clearly visible, albeit with substantial noise for the hole conduction regime (CNP = 10 V). Measurements are done using the Delta Mode of a Keithley Delta system with a current of 300 nA [183]. Source and V_A are connected to the ferromagnetic electrodes (blue) with an oxide barrier, while drain and V_B are barrier-free AuPd contacts (orange), as depicted in Figure 4.14 a).

The SD I-V characteristics of the above device are all linear with $9.5 \, k\Omega < R_C < 22 \, k\Omega$, which is below the range expected for the tunneling regime. From the plot of the extracted ΔR_{nl} for both sweeping directions against the back-gate voltage (Figure 4.14 c)), the barrier characteristic can be evaluated. Here the resistance change is the highest around the CNP, which is expected for highly decoupled tunneling contacts.

Out-of-plane B-field sweeps show the Hanle effect (Figure 4.14 b), which can be fitted to equation 2.83. The resulting spin diffusion length of 1.6 μm is then used to calculate the current polarization via equation 2.19. Thus gained polarization values of 5 % coincide with the range expected for low impedance contacts [134].

For the fabrication of a second device, the additional ALD step is omitted. Again a two-step spin-valve effect appears (see Figure 4.15 a). The measurements are carried out using the preamplifier stage mentioned in section 3.3 in a combined AC-DC method with the contact configuration as described above. From two-point sweeps as a function of back gate voltage, contact resistances in the range of $5 \, k\Omega - 20 \, k\Omega$ are determined. In the plot of ΔR_{nl} against the back-gate voltage (Fig. 4.15) no clear dependency is discernable, which indicates an intermediate electrode coupling regime.

The spin diffusion lengths derived from the Hanle measurements are less than half the values obtained for the former device. This reduction is attributable to surface contaminations/residues from the device fabrication, the presence of which is supported by the broad peak in the transfer curve.

From length dependent spin-valve measurements, the spin diffusion length as well as the current polarization can be extracted by fitting equation 2.19. The data in Figure 4.16 a) reveals an inhomogeneous oxide barrier across the flake. For the fitting,
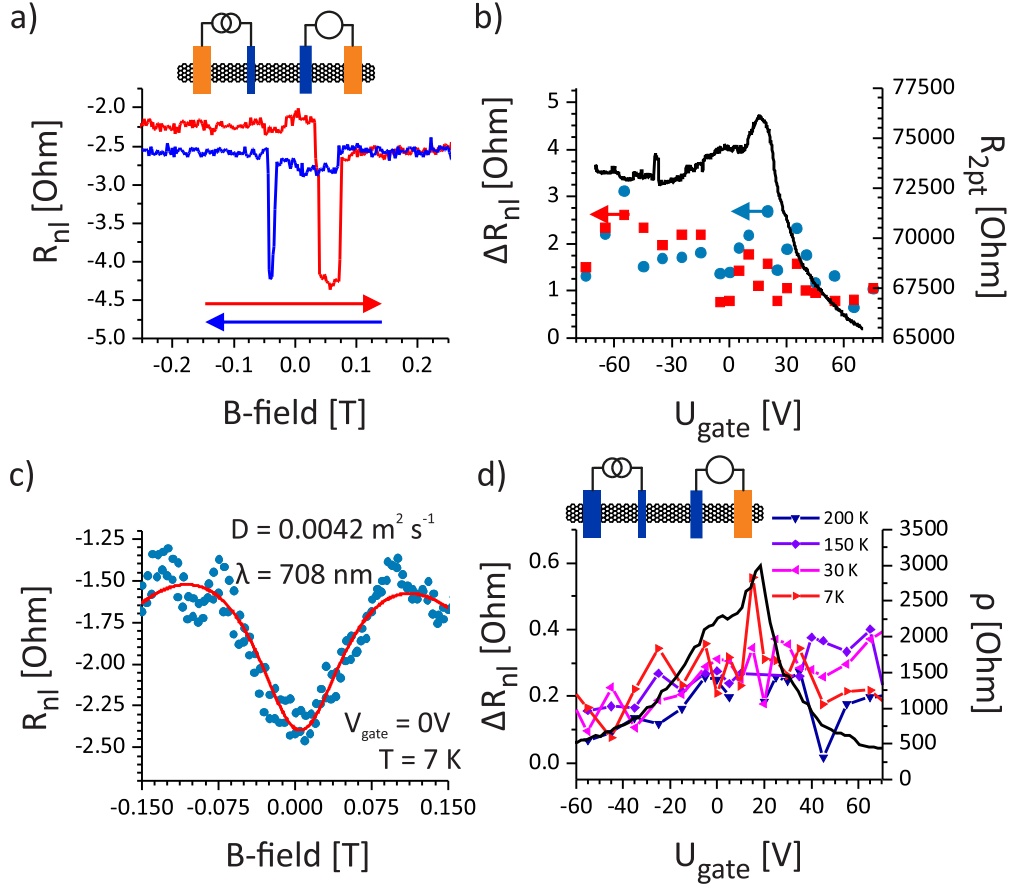
Fig. *4.15: a) Pristine graphene spin-valve effect (T = 1.4 K) for a ferromagnetic (Co) contact separation of 500 nm (see the contact configuration depicted above). b) Nonlocal resistance jumps vs. back-gate voltage, demonstrating that contacts with barriers are not fully decoupled from the graphene. c) Hanle curve at T = 1.4 K fitted to eq. 2.24 (red line). d) Gate dependence of the spin signal in the device altered by an unintentional voltage shock. The resulting contact arrangement enables to detect spin transport up to 200 K. See text for explanation.*

the outlier at L = 400 nm has been neglected. The obtained λ is very close to the value extracted from Hanle measurements, indicating that $T_1 = T_2$. To estimate the error by neglecting the contact resistance in eq. 2.19, the error on λ and P is estimated by using eq. 2.18 which accounts for finite contact resistances, although it is more difficult to fit. Along these lines, ΔR_{nl} is calculated with the parameters of the present device for a range of R_C. The resulting curves are fitted with eq. 2.19 and λ^* and P^* are extracted as a measure for the deviation. Results are shown in Figure 4.16 b). With the contact resistances extracted from the back-gate sweeps, the error on λ is less than 1 %. However, the error is considerably larger for the polarization, i.e., on the order of 10 %. Nevertheless, the graph shows that while the error on λ is limited to maximally

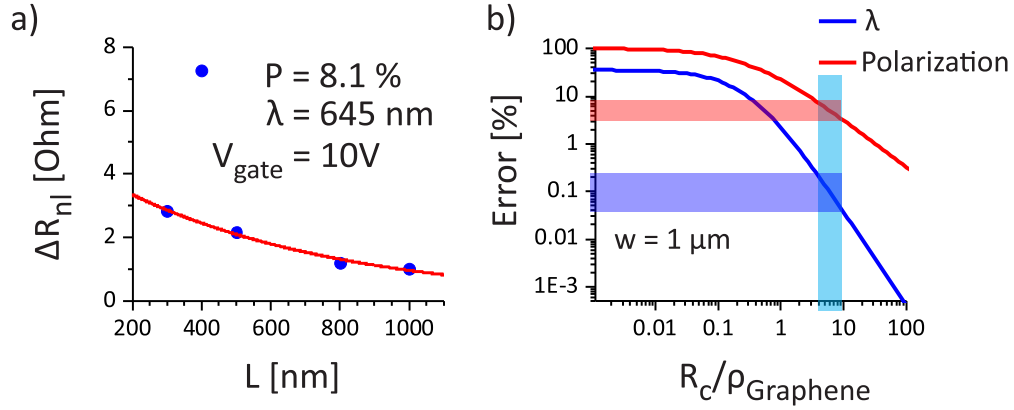**Fig.** *4.16: a) Spin-valve signals for different contact separations in the device of figure 4.15. The data point at 400 nm is excluded from the fit to eq. 2.19. b) Error that arises in the fit in panel a) by neglecting R_C. The vertical blue rectangle highlights the contact resistance range.*

20 %, the polarization can be totally wrong if equation 2.19 is used and the contact resistance neglected.

Due to a voltage pulse in the above device, the graphene flake was partially peeled-off the substrate and also the contact resistance decreased. As a consequence, the magnitude of the spin signal is reduced by one order of magnitude. This behavior can be explained by the reduced contact separation in the current path as the configuration had to be changed, in conjunction with the fact that the drain electrode now also had to be ferromagnetic. The former AuPd drain electrode (Figure 4.15 a) did not interfere with the spin imbalance, while the ferromagnetic drain electrode actively pumps on the spin bath. The back-gate dependence of the spin signal is still flat up to 200 K, signifying the robustness of spin injection in this device (see Figure 4.15 d).

It is concluded that spin transport with decoupled contacts is feasible by the approach described above. A carefully oxidized metal film is sufficient to attain efficient spin injection from cobalt into graphene, so that the additional ALD step can be omitted. However, the oxide barriers turn out to be very sensitive against voltage fluctuations that can appear during thermal cycles, thereby making consecutive measurements difficult to compare. Three-terminal measurements performed at the end of the measurement series yield contact resistances in the range $2\,k\Omega - 11\,k\Omega$, corresponding to almost half of the values extracted from the two-point measurements performed at the beginning.

4.2.1.2 Nonlocal resistance fluctuations

All samples with an oxide tunnel-barrier made of TiO_2, regardless of their structural integrity, displayed a varying background for the R_{nl}, which introduces an offset for

the MR. For the device in Figure 4.15 this offset is on the order of $3\,\Omega$ at the given gate voltage. In the following, the origin of this effect is explained on the basis of complementary data gained from two devices with different contact separations (L = 500 and 600 nm).
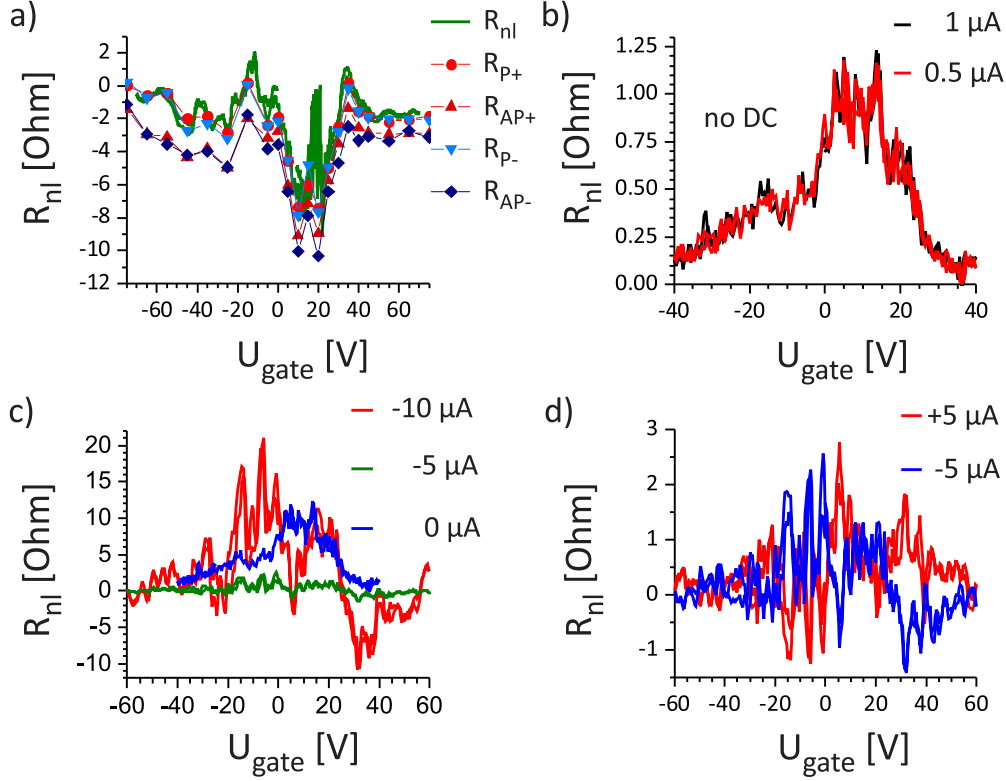
Fig. *4.17: a) Resistance levels defined in Figure 2.9 for the device in Figure 4.15. b) Influence of the AC stimulus on the nonlocal resistance when no DC voltage is applied. c) Effect of the DC offset on R_{nl} while applying 500 nA AC current. d) Effect of reversing the DC-offset on R_{nl}. The data in panels (b-d) are for a device with L = 600 nm.*

The backgate voltage dependent oscillating offset is constant during in-plane B-field sweeps. In Figure 4.17 a) R_{AP} and R_P extracted from the MR[10] are plotted against the applied back-gate voltage together with R_{nl} from a direct back-gate measurement for the device in Figure 4.15 a) (L = 500 nm). Both quantities follow the trend of the black curve, where R_{AP} is offset by ΔR_{nl}. On this basis it can be concluded that it is a charge based phenomenon as both spin orientations are effected the same, while the resistive change is constant (see Fig 4.15).

By applying an AC current on top of the DC current between source and drain, the dependency of the nonlocal signal on the stimulus can be evaluated. While the magnitude of the AC signal has only little influence on the oscillations when no DC

---

[10]Resistance levels are defined in Figure 2.9.
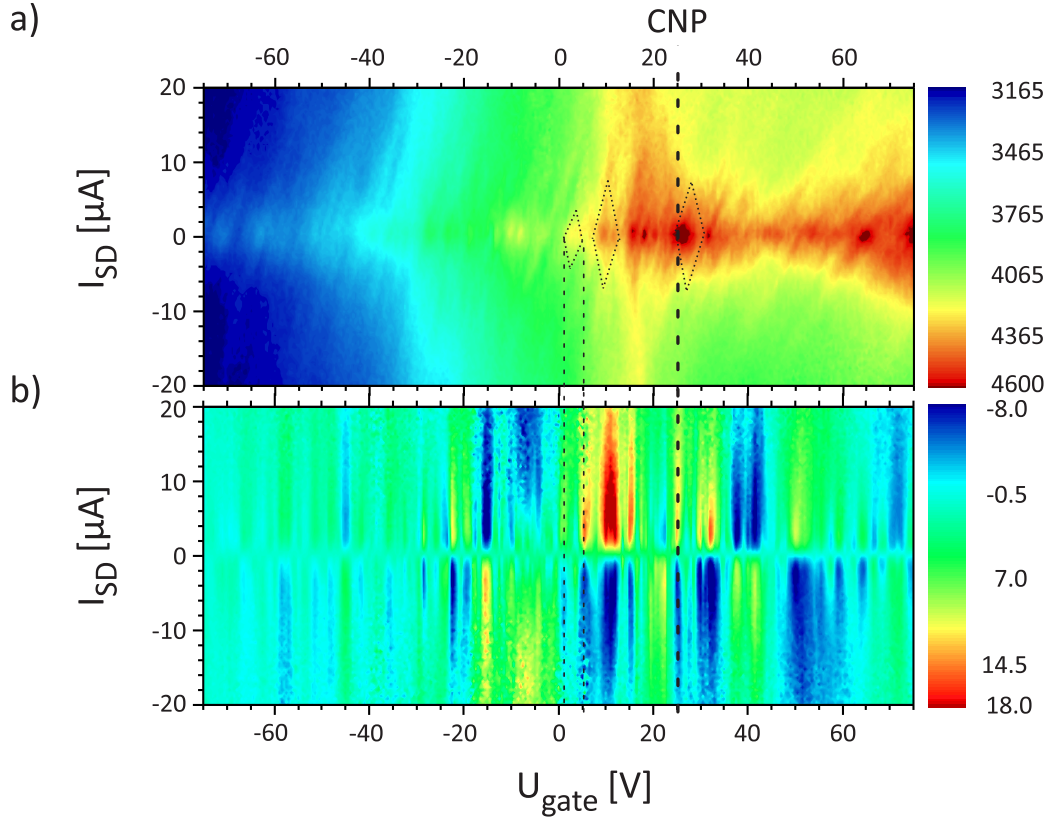
***Fig.** 4.18: a) Local and (b) nonlocal voltage displayed as color-scale dV/dI map involving source-drain current and back-gate voltage dependence (T = 7.6 K). The position of the CNP is indicated by a vertical dashed line in both maps. A possible Coulomb diamond is highlighted in panel a).*

current is applied (Fig. 4.17 b, L = 600 nm), the DC offset strongly enhances and alters the oscillations. The sum of both DC traces (±) in Figure 4.17 d) reproduces well the plain AC-trace in panel c). For this specific curve, the traces appear to be mirrored with respect to the AC-trace, but this symmetry is not always present.

The transfer curves in Figure 4.17 b-c) are in principle horizontal line cuts of Figure 4.18 b), but recorded with a smaller point separation with respect to the gate voltage in order to better resolve the oscillations. As can be seen from Figure 4.18 b), the magnitude of the nonlocal oscillations strongly depends on the applied DC current, with the maximum magnitude of the resonances depending on the gate voltage and the DC current. Interestingly, the local dV/dI signal also shows internal structure in the form of numerous diagonal lines, with some of them producing diamond-like features as indicated in Figure 4.18 a). The back gate voltages at which these diamonds occur closely coincide with the minima and maxima of the oscillations in the nonlocal signal. This indicates that the oscillations in the nonlocal signal are associated with a certain type of resonance along the current path. It should be noted that the poor

a)

b)
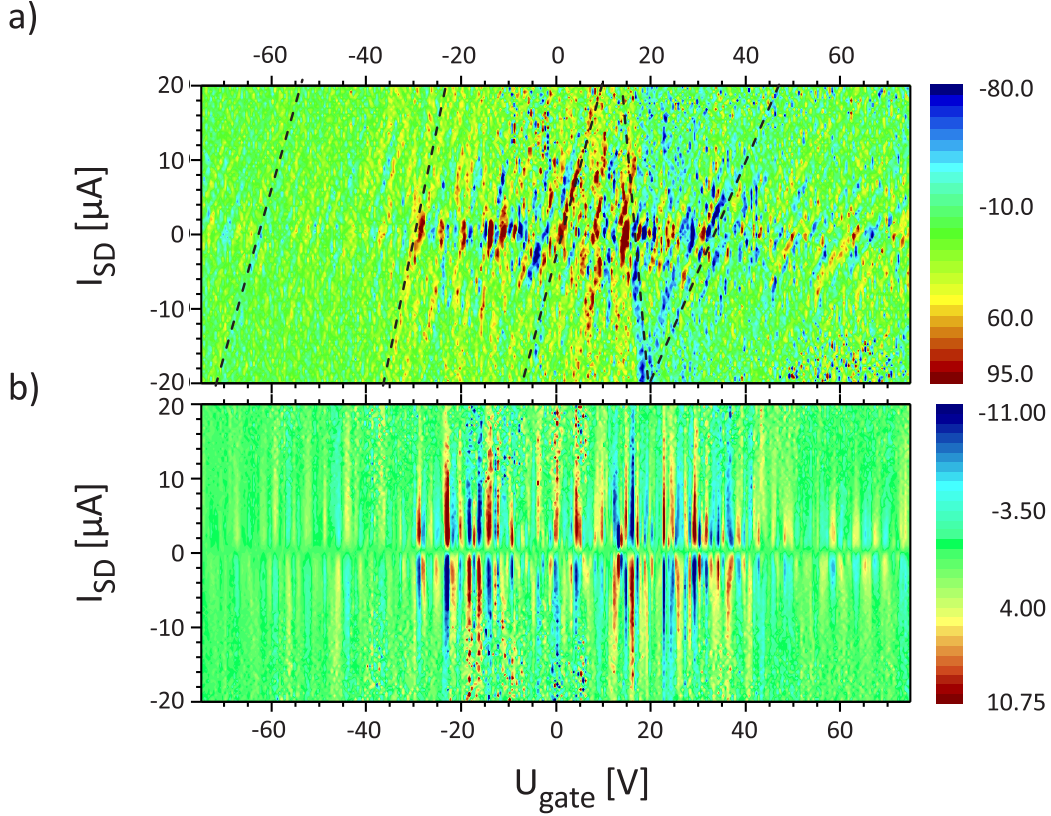
Fig. 4.19: a,b) maps of Figure 4.18 a,b) differentiated with respect to the back-gate voltage.

resolution of the diamonds is due to the fact that the experiment is performed using a constant current rather than constant voltage.

Differentiating the SD current sweeps with respect to the gate voltage removes the background (see Figure 4.19). For the nonlocal signal, the oscillations become more evident due to alternating sign. For the local signal, the diagonal lines are more pronounced, whereas the diamonds seen in Figure 4.18 are less visible.

Figure 4.20 illustrates the influence of an in-plane B-field on both, the local and nonlocal signal, for a single SD current sweep. The resonance features in the nonlocal signal at $-1.4\,\mu$A and $2\,\mu$A are reduced in magnitude when the B-field is increased. In comparison, the features in the local signal get smeared out with raising B-field. Furthermore, in-plane B-field sweeps performed for two inner extrema in Figure 4.20 a) reveal an asymmetric switching behavior. Increasing the DC offset further to $2\,\mu$A leads to a two-step switching behavior. For significantly larger DC offsets ($> 10\,\mu$A), no spin signal could be detected any more. Not all studied contact configurations show the presented asymmetric spin-valve effect. For some devices only one reproducible resistive jump could be seen over a broad range of DC-current.

To unravel the origin of this varying background, the temperature dependency is
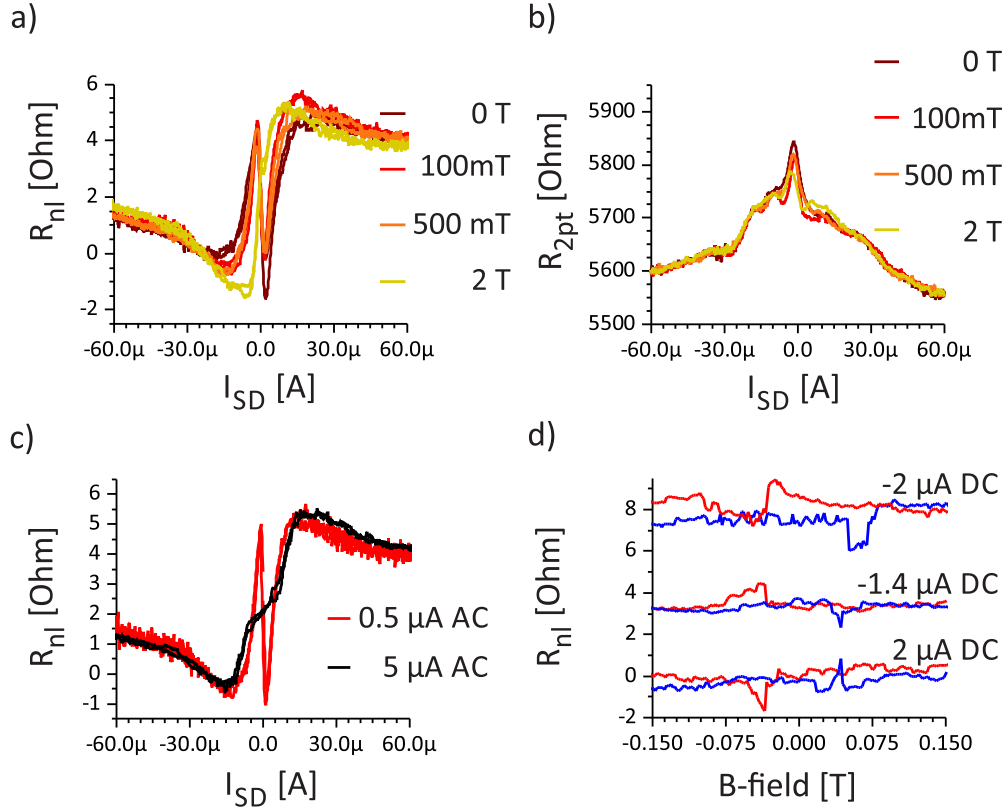
Fig. *4.20: a) R_{nl} of the above device as a function of applied DC current for different in-plane magnetizations and an applied AC current of 500 nA. b) Corresponding local signal to panel a). c) Influence of the AC stimulus on the nonlocal signal. d) In-plane B-field sweeps performed at the two extrema around zero current in panel a). An asymmetric spin-valve effect is clearly visible. A further increased DC current ($-2\mu A$) restores the symmetric two-step switching.*

studied. The following measurements are done with a 4μ AC-current and no DC offset. In Figure 4.21 a), data recorded at four different temperatures using a contact configuration as in Figure 4.15 d) are shown. It can be clearly seen that R_{nl} at 35 K shows less features compared to the 6 K trace, and that the amplitude reduces even further upon heating the sample to 50 K. In a second thermal cycle of the same device, the back-gate dependent behavior has substantially changed (Figure 4.21 b). This is attributed to a resistance change in the circuit, most likely due to a breakdown of the oxide tunnel barrier during the thermal cycle.

Subtracting the R_{nl} values collected above 30 K from the curve acquired at 254 mK removes some background and restores the strong oscillation behavior (Fig. 4.21 c). Extracting the V_{gate} values for the minima and maxima of R_{nl}, converting them into

Fermi energies via

$$E_F = \hbar v_F \sqrt{\pi \left[\frac{\epsilon_r \epsilon_0}{d_{SiO_2} e} (V_{\text{Gate}} - V_{\text{CNP}}) \right]^2 + \pi n_0^2} \qquad (4.4)$$

and plotting the latter values against integers (with zero corresponding to the CNP) yields plots such as in Figure 4.21 d) (lower panel). A similar procedure has previously been followed to evaluate the resistance oscillations for two-terminal measurements in the ballistic regime with graphene as a channel material [184]. In this case, the observed oscillations have been assigned to resonance within a Fabry-Perot cavity formed between the electrical contacts. On this basis, the cavity length could be extracted from the slope of the $E_F(I)$ vs. I plots, given as

$$E_F \propto \frac{\pi N v_F}{L_{\text{cav.}}}. \qquad (4.5)$$

While for larger integers a straight line is observed, a non-linear behavior occurs for integers below 10 (lower panel in Figure 4.17 d). When a residual charge carrier density (n_0) is taken into account for calculating E_F, a linear relationship is imparted over the whole range (Fig. 4.17 d), top panel). Interestingly, the same slope can be extracted from the two successive low-temperature sweeps in Figure 4.21 a) and b), although they display a different pattern. Different electrode configurations of the contacted flake give rise to different slopes. The cavity length extracted with the aid of equation 4.5 from d) has no corresponding geometrical length in the device. Since this equation has been derived for a ballistic junction with a contact separation of tens of nanometers, which is not the case for the studied devices (contact separation well above 300 nm).

Similar nonlocal oscillations have been reported for carbon nanotubes (CNTs) [185] and graphene, both with ferromagnetic contacts [133]. While for the CNTs the observed oscillations had a similar magnitude of R_{nl} like for the presented devices, the situation is different for graphene. For the latter, universal conductance fluctuations (UCFs) or Fabry-Perot resonances (FPRs) [186] have been proposed as origin of the oscillations. Judged from the above data, UCFs are an unlikely cause, as they should change after heating up the sample. Although slight alterations might indeed be visible in Figure 4.21, it is more relevant that after subtracting the background the curves almost match, and in addition the oscillation minima yield the same slope when plotted against integers. At the same time, also no clear signatures for FPRs can be seen in Figure 4.19. In fact, while there appear faint diagonal lines, their intensity is too small to signify FPRs. Moreover, the relatively large contact separations render any ballistic phenomenon unlikely.

A more likely explanation is the magneto-Coulomb effect (MCE), which is often observed for local measurements on CNT and quantum dots (QD) and is manifested by back-gate dependent oscillations [187]. In order to be observable, at least one ferromagnetic lead needs to be capacitively coupled to a QD [188]. The QD for the presented data is assumed to be formed by the graphene underneath the ferromagnetic contact, based upon the following observations. First, it has been concluded that due to local doping by the Co, the Fermi level of the graphene section underneath the Co contacts is shifted with respect to the one of the graphene in the channel [189]. Secondly, Ti strongly interacts with graphene, as evidenced by the emergence of a D-peak in Raman spectra [190]. Although in the present samples, no D-peak is observed for graphene covered by 300 pm Ti, the situation could be different when the Co is deposited on top. The MCE might be further enhanced by the fact that the ϵ_r (TiO$_2$) is
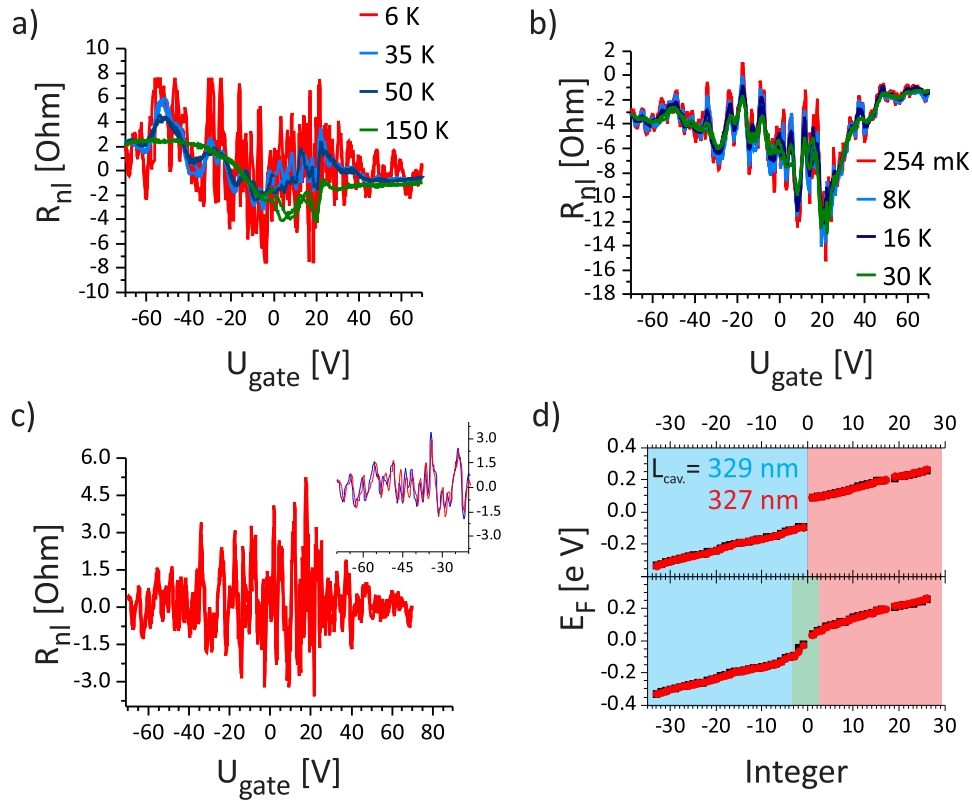
Fig. 4.21: a, b) Nonlocal signal of the above device as a function of back-gate voltage recorded during two consecutive thermal cycles using the same contact configuration. c) Subtracting the 30 K data from the 250 mK curve highlights the oscillations. The insert is a zoom-in, with the sweep directions distinguished by red and blue. d) Extracted Fermi energies for the minima (black) and maxima (red) of the gate sweep in panel c). Considering n_0 in the E_F calculation results in a straight line when plotted against integers (top axis), while neglecting n_0 leaves a nonlinear transition (green) between hole (red) and electron (blue) conduction regime.

nearly an order of magnitude larger than that of alumina[11], which strongly increases the capacitance in the first case. Convincing proof that the MCE is indeed underlying the oscillations is provided by the results in Figure 4.20. Similar MR behavior has been observed for single-electron transistors realized with CNTs [192].

4.2.2 Spin valves comprising graphene stripes
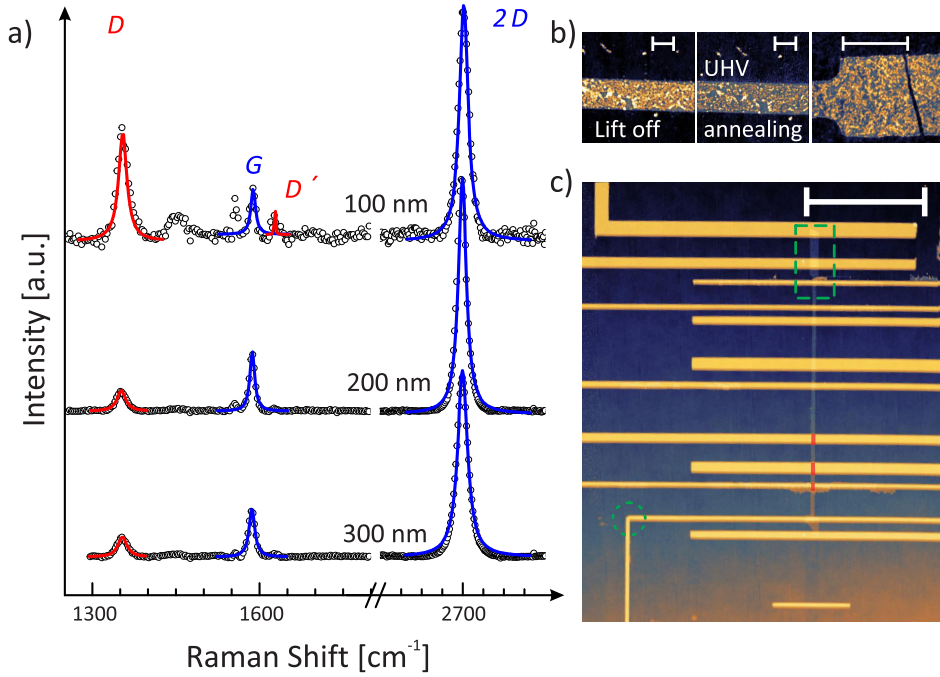
Fig. *4.22: a) Raman spectra of graphene stripes of different width (λ_{exc} = 633 nm). Solid lines are fits to a single Lorentzian. b) AFM images of process residues after the RIE step, which are difficult to remove (left image). Heating the sample to 300°C in reforming gas at 10^{-4} mbar helps to eliminate them partially (middle image). Clean stripes can be obtained by soaking the sample for > 48 h in a 1:1 acetone/NEP mixture, followed by a heating step (right image). c) Typical spin-valve with a channel width of 200 nm. Marked are the larger ends of the stripe (green square), 90° turns (green circles) and the reduced contact area (red square). Scale bar in b) is 500 nm, in c) 5 μm.*

As follows from the previous section, both the composition and structural integrity of the oxide barrier strongly influence the performance of graphene-based spin-valves. Thus, a reproducible protocol is needed that allows precise control of the oxide thickness and chemical composition. This task is, however, rather difficult to achieve by thermal evaporation.

As an alternative to tunneling contacts, the contact resistance can be increased by reducing the contact area [193]. One possibility would be the use of an oxide

---

[11]ϵ_r(TiO$_2$) = 86-170 , ϵ_r(Al$_2$O$_3$) = 9.34-11.54 [191]

barrier that only partially covers the interface between ferromagnetic contact and channel [194]. Another option is to exfoliate graphene stripes with a width below 1 μm, and to contact them without any oxide barrier [133, 195]. For the latter approach applied to metallic spin transport channels, the spin injection efficiency has been found to scale inverse exponentially with the junction area [196].

Here, graphene stripes are patterned into a bone like structure by means of RIE, as detailed in section 3.2. The main challenge is to remove the etching mask completely. The standard lift-off process leaves cross-linked PMMA residues on the stripe (Fig 4.22 b). The cross-linking most likely originates from the RIE step. Heating the sample under UHV is somewhat helpful, although it only partially removes the residues. Better results are achieved by leaving the sample for > 48 h in a 1:1 mixture of NEP and acetone, followed by heating to 140 °C in forming gas atmosphere at 10^{-4} mbar for > 2 h. A disadvantage of this method is that it leads to graphene which is strongly coupled to the SiO_2 on the substrate.

Raman data gained from different graphene stripes indicate that there are only minor edge effects above a width of 200 nm, as reflected by a small D/G peak ratio. Accordingly, stripes of 200 nm width are used for the experiments described below.

4.2.2.1 Etched stripes with transparent contacts

A typical device is shown in Figure 4.22 c). The purpose of the bone shape is to render the terminal regions better visible under the optical microscope. Additional contacts to these regions serve to ensure good electrical contact to the graphene in order to pinpoint a stable electric potential.

MR curves recorded by sweeping the in-plane B-field show a spin-valve effect, with the number of steps depending on the applied gate voltage and contact separation (L) (Fig. 4.23 a). For high negative voltages (strong electrostatic p-doping) up to four resistance levels (R_1-R_4) can be seen. Plotting the corresponding ΔR values against the applied gate voltages reveals that the spin signal decreases as the CNP (U_{gate} = +20.8 V) is approached. In addition, the MR traces get noisy, which obscures the spin-valve effect. This behavior is consistent with theory that predicts for transparent contacts an inverse scaling of the spin signal with the channel resistance (see eq. 2.18). Presumably due to residues from the device fabrication, ρ_{CNP} is only 3.5 kΩ, which still allows to observe a spin signal at the CNP of the device. First contacted stripes showed strong PMMA contaminations in AFM images and an increase of the spin signal as the CNP is approached, rather than an inverse spin signal dependency on the channel resistance as it is expected for transparent contacts. Thoroughly cleaning the stripes after the RIE step greatly eliminated the PMMA residuals and a transparent transfer characteristic could be optioned. The cleaning procedure was the following: the freshly etched device was soaked for at least 48 h in a solution of 1:1 acetone and NEP and afterwards
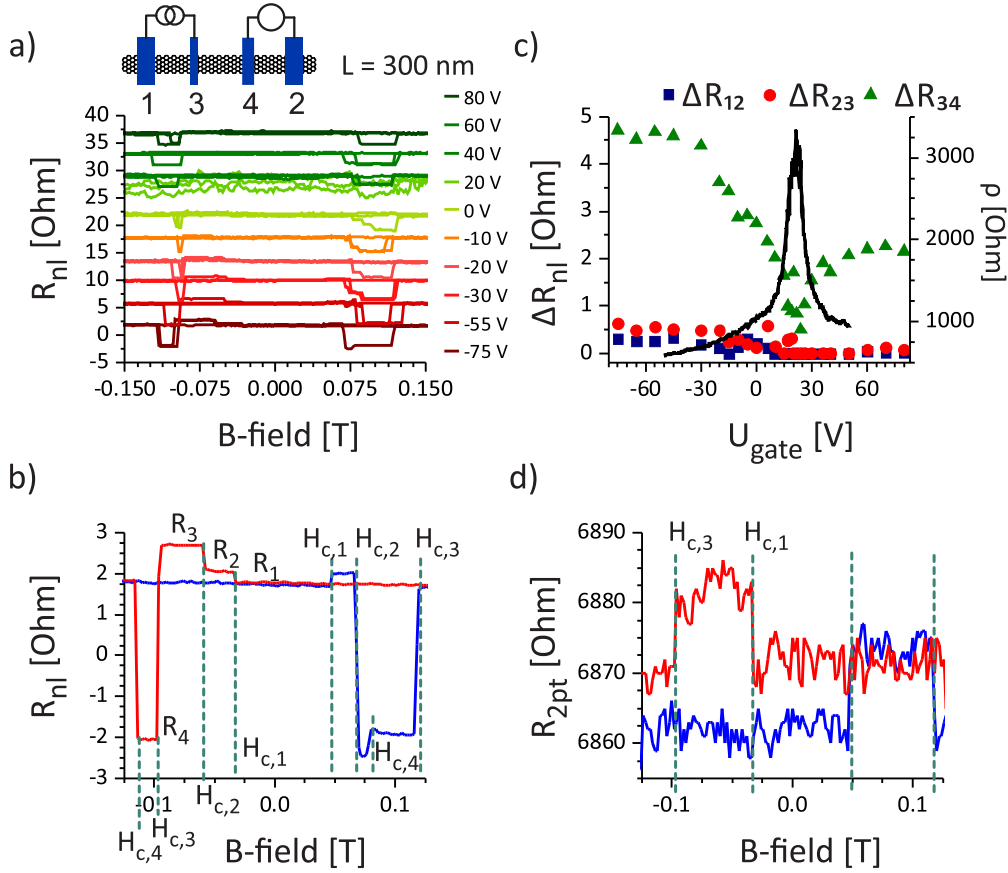
Fig. 4.23: a) Back-gate dependent magnetoresistance (in-plane B-field) of a graphene stripe spin-valve. Two or four resistance levels are observable, depending on the gate voltage. b) Single MR trace from panel a) displaying different coercive fields when sweeping the B-field from +/- or -/+. c) Difference of the resistance levels marked in panel b) for different back-gate voltages. The spin signal decreases as the CNP is approached. d) Two-point MR exhibiting spin-valve behavior.

heated to 120-160 °C under vacuum ($< 1 \cdot 10^{-7}$ mbar). After the vacuum had stabilized, Ar/H_2 (80/20) is introduced at a pressure of $1 \cdot 10^{-4}$ mbar. Owing to the catalytic activity of the Pd in the AuPd marker on the substrate good cleaning results are achievable in this manner.

It is noteworthy that besides the nonlocal spin signal also a spin signal in the current circuit (Fig. 4.23 d) is detectable for this specific device (in contrast to other devices). This signal exhibits the same gate dependence as the nonlocal signal. For both MR traces, the coercive fields can be easily identified. An interesting observation is the change of switching order for the coercive fields for contacts three and four. Specifically, while for positive sweeps the order is as expected according to the contact widths[12], the two contacts with the smallest widths change their switching order for

---

[12] 1 = 360 nm, 2 = 230 nm, 3 = 90 nm, 4 = 110 nm
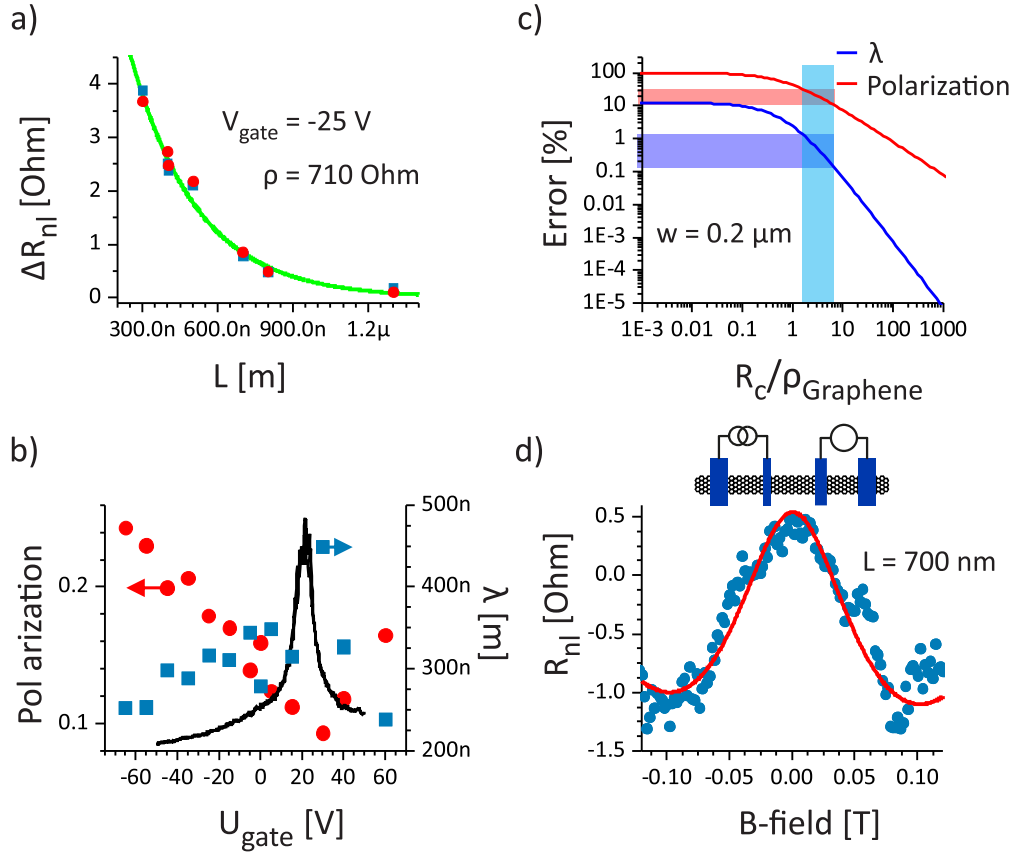
Fig. *4.24: a) Fit of eqn. 2.18 to ΔR_{nl} vs. the contact separation L gives $\lambda = 310\,nm$ and a polarization of 18 %. b) Polarization and spin diffusion length as a function of back-gate voltage. The resistance from Fig. 4.23 c is shown in black without a scale to indicate the CNP. c) Error made in panel a) by underestimating R_C. The horizontal blue rectangle marks the ratio for the device at $U_{gate} = -25\,V$. d) Hanle curve for $U_{gate} = -15\,V$ and $T = 1.6\,K$. The fit of eqn. 2.24 (red line) yields $\lambda = 290\,nm$.*

the negative sweep direction. This observation might be due to the roughness of the contacts which can pin magnetic domains within the electrode material and thus affect the coercive field.

As before the spin signal is evaluated for different contact separation L. Together with the multiple switching behavior the data is fitted to eq. 2.18 and yields the spin polarization P and λ, as plotted in Figure 4.24 a). The contact resistance extracted from transfer curves recorded by two-point measurements falls in the range between 1.3 k and 4.8 kΩ. In comparison, the three-point resistances are independent of the gate voltage. For the fitting an average R_C of 1.3 kΩ is used to account for the transparent interface. Considering a larger R_C significantly reduces the extracted P ($P(1.31\,k\Omega) = 0.18$ to $P(4.8\,k\Omega) = 0.14$ for Fig. 4.24 a)), while leaving λ almost unaffected (for error estimation see Fig. 4.24 c). Over the entire gate voltage range, λ shows no obvious trend and varies between 250 and 350 nm (Fig. 4.24 b).

The extracted spin polarization shows a clear trend with gate voltage, involving a decrease from 24.3 % to 9.3 % as the CNP is approached. This trend is reasonable, based upon the fact that R_N increases upon approaching the CNP, thereby reducing R_C/R_N. The smaller ratio results in a poorer spin injection rate and lowers the polarization. The maximum polarization of 24 % achieved for this device seems surprisingly large in view of the transparent contacts. One plausible explanation for the enhancement relates to the reduced graphene width, which has been documented to increase the spin polarization for the case of metal spin-valves [196].

Hanle measurements are quite difficult for the stripes at low temperatures, as they are obscured by UCFs and the detector acts as a spin sink due to the transparent interface. Another complication in such experiments is that trace and retrace often do not match. In the rare cases where they do match, as exemplified in Figure 4.24 d), the extracted λ_{Hanle} (= 290 nm) is similar to the value of λ derived from in-plane sweeps. Such short spin diffusion length on the order of the stripe width is remarkable in view of the fact that a spin signal can be detected by in-plane measurements for L = 1600 nm. One possible explanation comprises surface residues introduced by the RIE step (as observed by AFM), which could act as scattering sites to reduce λ.

4.2.2.2   Covalently functionalized graphene stripes

In the following, the results of measurements on graphene stripes functionalized by NPD for 90 s (device I) or 900 s (device II) are presented. Device I corresponds to the one from the last section. For the second device (II) the fabrication process was modified to reduce the surface residues on top of the graphene. To this end, the immersion time in the solvent and the heating time in forming gas atmosphere after RIE were extended to 62 h and 6 h, respectively.

Four-point resistivity measurements reveal a shift of the CNP from 21.2 V to 27 V (ΔU = 5.8 V) for I (2.8 V to 33.8 V; ΔU = 31 V for II) as can be seen in Figure 4.25 (b) together with an increased four point resistance. The high U_{CNP} together with the low ρ_{CNP} indicates that the pristine sample I is not as clean as the pristine sample II. Complementary to the CNP shift, there is an increase of ρ_{CNP} for both samples. For sample I ΔR_{nl} changes only little, while the notable increase of R_N (ρ_{graphene}) results in a 30 V gate window around the CNP wherein no spin signal is detectable after the functionalization. In contrast, for sample II the spin-valve effect is strongly amplified. The enhancement in ΔR_{nl} in both cases is stronger for the hole than for electron conduction regime.

The comparison of two- and four-point measurements of sample II demonstrates that the resistance change is mainly due to an increase of ρ_{graphene}, as the two point measurements nearly match each other (Fig. 4.26 a and b). It can be seen that R_C only slightly changed. From the multiple switching behavior of functionalized sample I, λ and P can be calculated and compared to the pristine case. Figure 4.26 d) indicates that
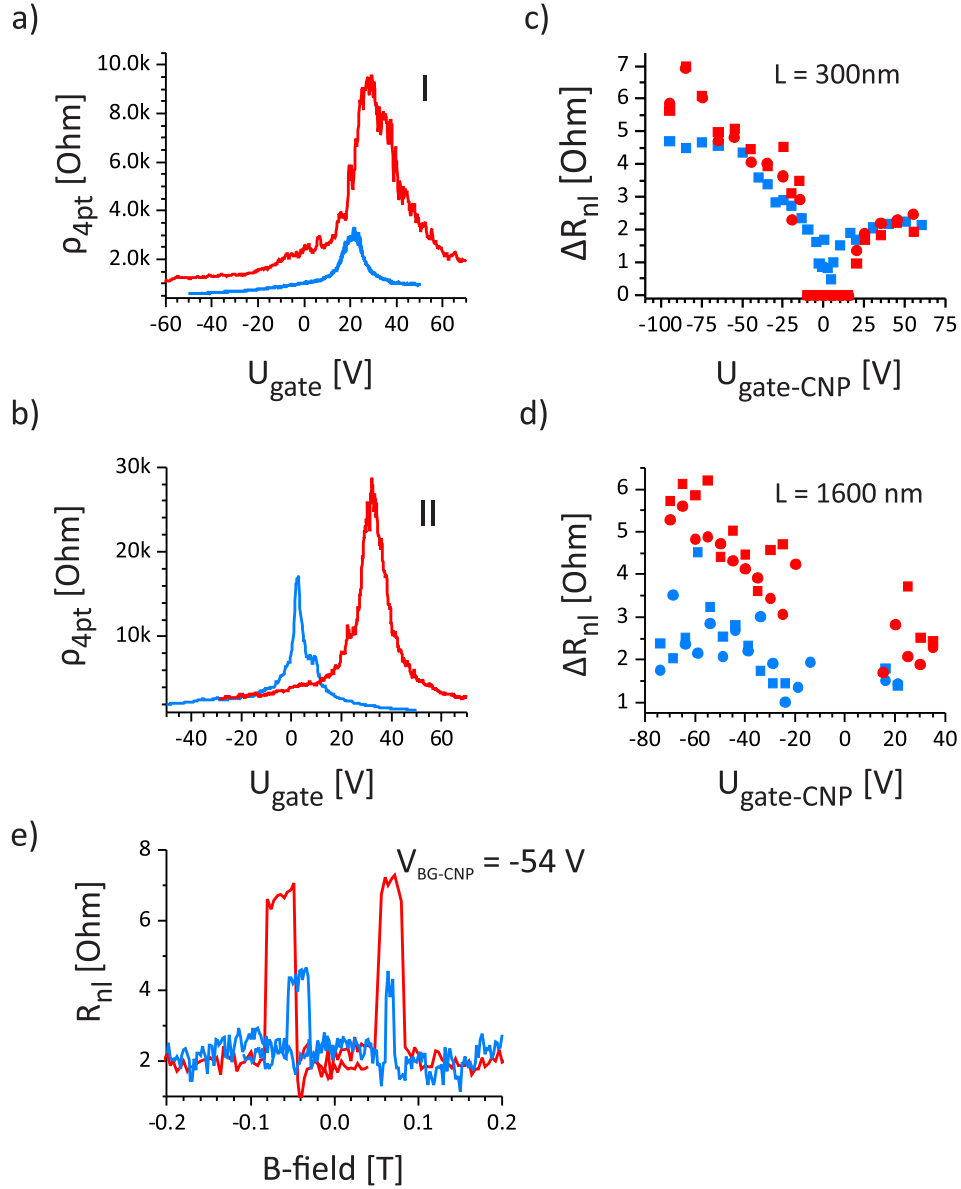
Fig. 4.25: a) Transfer curve for device I before (blue curve) and after (red curve) NPD functionalization of the graphene stripe. b) Same plot as in panel a) for device II. c) Resistive jumps extracted before (blue) and after (red) functionalization of device I. d) Same plot as in panel c) for device II. e) MR-curve for device II befor (blue) and after (red) functionalization. The spin signal is clearly enhanced.

the small enhancement of ΔR_{nl} seen in Figure 4.25 b) causes a polarization increase by roughly 5 %, while λ is reduced. This effect should be even more pronounced for device II; however, this assumption could not be tested because only two contact separations could be investigated after the functionalization.
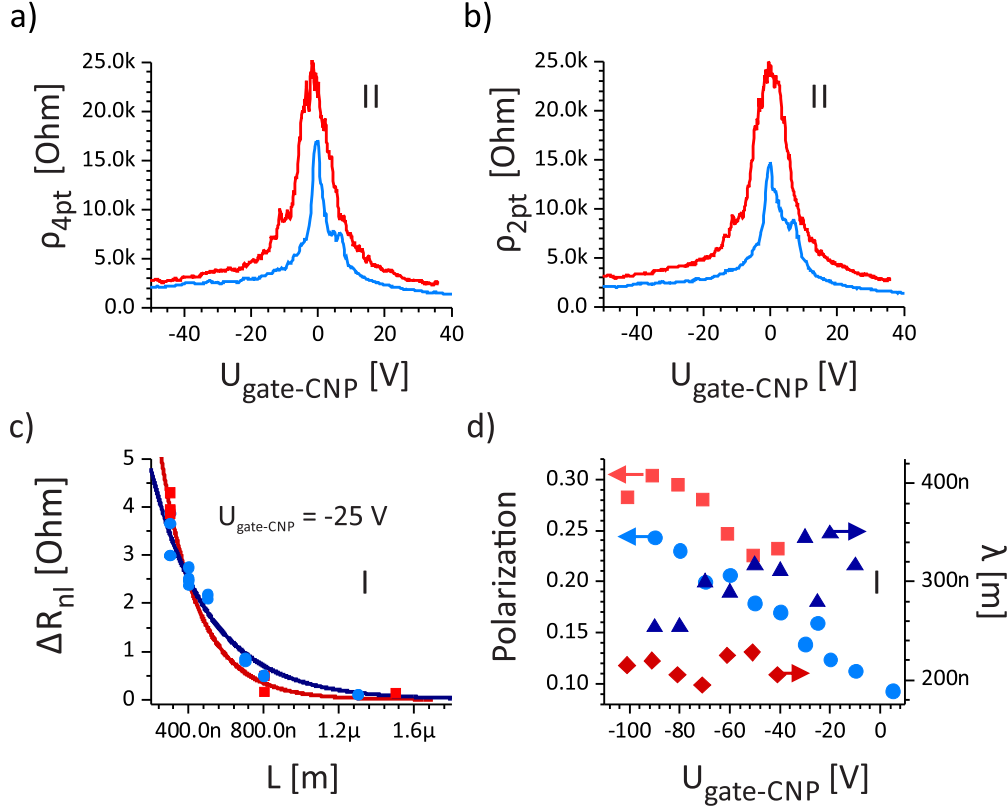
Fig. *4.26: a) Four- and b) two-point resistivity before (blue curve) and after (red curve) NPD functionalization of device II. R_C changes only little after the thermal cycle. c) Fits of eqn. 2.19 (solid line) to ΔR_{nl} values obtained for different L before (blue) and after (red) NPD functionalization of device I. d) Polarization and λ, obtained similar to panel c), in dependence of back-gate voltage.*

4.2.3 Conclusion

A fabrication process has been developed for mixed oxide barriers based on TiO_2/Al_2O_3 that allows for efficient spin injection into graphene. A key step is the treatment of the metal seeding layer by oxygen. It also turned out that the deposition of the ferromagnetic contacts requires special care. In particular, for base pressures of the chamber above 10^{-7} mbar no AMR effect could be observed.

For graphene spin-valves with oxide barriers, gate dependent fluctuations in R_{nl} were observed. Convincing evidence was gained that these oscillations originate from the magneto-Coulomb effect (MCE). While this effect is well documented for CNTs and QDs, it had not been reported for graphene spin-valves yet. Particularly interesting is that the oscillations manifest themselves in the nonlocal signal as this measuring configuration should in principle eliminate such contributions.

Owing to their relatively low stability under applied bias, the oxide tunnel barriers did not allow for consecutive experimental studies of the spin-valve effect. Especially during extended measurements using currents above $1\,\mu A$, significant changes in the

spin signal were encountered with this type of device. Consequently, an alternative spin-valve structure with transparent contacts was devised. The contact resistance imparted by the reduced contact area enabled improved spin injection and thus an enhanced spin signal. The remarkably high spin signals in the pristine graphene stripes are attributed to the reduction of the channel width, which decreases the size of the spin bath, that is manipulated.

Covalent functionalization of graphene within a spin-valve did not change the general transfer characteristics compared to section 4.1. The spin-related switching signal was found to be enhanced by a factor of up to two. The gained data indicate that the functionalization reduces the spin diffusion length, while the current polarization is increased. The observed reduction of λ is reasonable, as the functionalization is known to introduce scattering sites. In contrast, the increased polarization is unexpected, and further experiments are needed to clarify the influence of thermal cycling. Likewise, questions remain with respect to the determined spin diffusion length in comparison to the channel length of the graphene stripes.

5 SnTe nanostructures

5.1 Magnetotransport in SnTe nanostructures

Charge transport studies on SnTe date back to the 1980s, where the samples under study were mostly single/polycrystalline with macroscopic dimensions [197]. Although a lot of effort has been devoted to the sample quality with respect to stoichiometry, only few works have dealt with quantum transport phenomena in SnTe [50, 198]. Only very recently, stimulated by the proposal that SnTe represents a topological crystalline insulator, first electrical data on SnTe nanostructures have been published [199–202]. The aim of the magnetotransport experiments described below was to identify signatures of topological protected surface states in as-grown SnTe nanostructures.
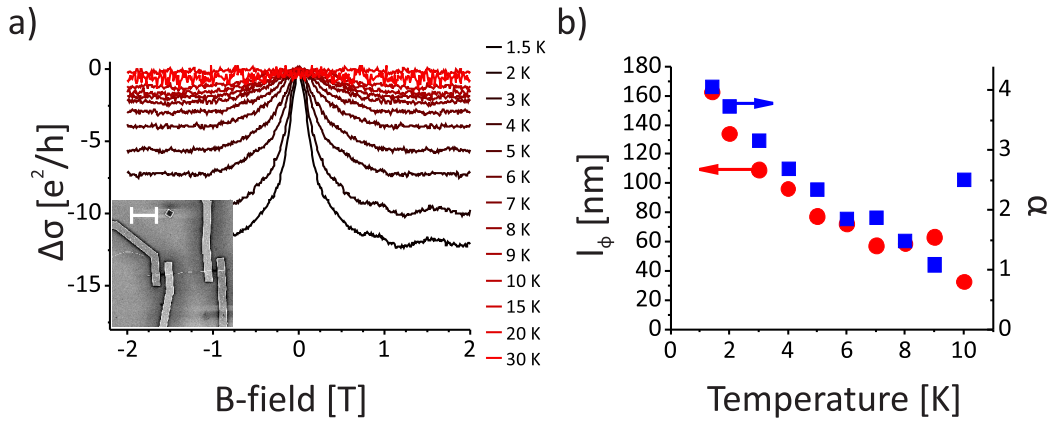
Fig. *5.1: a) Normalized magnetoconductance of a SnTe nanowire for different temperatures (out-of-plane B-field). Insert depicts an electron micrograph of the device. Scale bar is 5 μm. b) Phase coherence length and fitting parameter α derived from fits of eqn. 2.10 to the data in panel a).*

In a typical experiment, the SnTe nanowires are contacted by four AuPd contacts which extend over the entire width of the wires, as shown in the inset of Figure 5.1 a). The overall fabrication process is described in 3.2.1. The exemplified wire has a width of 60 nm, as determined by SEM. Examination of a wide range of wires showed that the SEM-derived width is in good agreement with the height extracted from AFM measurements.

Essential for achieving good electrical contact to SnTe is the argon plasma pretreatment described in section 3.2.1. As the SnTe nanowires are very sensitive, the power of the ultrasound applied during wedge bonding has to be reduced to a minimum. In general, electrically contacted SnTe nanostructures could only be reproducibly measured when a 17 μm diameter gold wire was used for the wedge bonding. In comparison to the 33 μm wire, the smaller diameter allowed for a significant reduction of the ultrasound power.

The electrical resistivity of the SnTe nanowires shows no B-field dependence within

Fig. *5.2: a) Normalized resistance of different SnTe wires as a function of temperature. The residual resistance is reached at ~ 35 K. Inset shows an AFM image of the device. b) Magnetoresistance traces recorded for different angles of the B-field with respect to the surface normal.*

the range of ± 12 T when the field is aligned along the wire long axis. Upon aligning the wire axis orthogonal to the B-field, a weak quadratic transverse magnetoresistance appears, as shown in Figure 5.2. This behavior can be described by Koh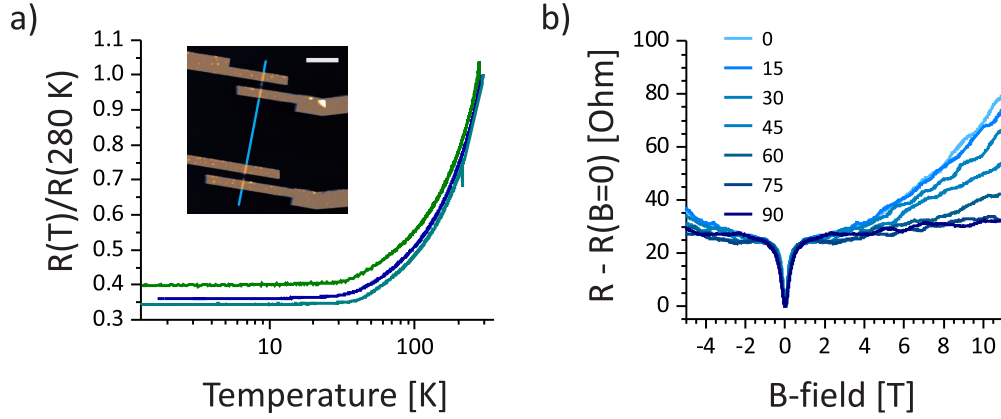ler's rule (see section 2.2.3). At low temperatures, distinct universal conduction fluctuations (UCFs) can be observed for both alignment directions.

The most prominent feature in the MR is a dip at zero magnetic field, which is typical for WAL. Similar to WL, this dip reflects a pronounced conduction modulation at $B = 0$ T. As can be seen in Figure 5.1, this reaches up to 12 G_0[1] at the lowest temperature. Such strong feature is observed for several contacted wires at 1.4 K.

From the WAL, a phase coherence length (l_φ) can be extracted. In the 2 D case, the HNL model (see section 2.2.5) can be used for fitting. It yields $l_\varphi = 160$ nm, which exceeds the width of the sample. The prefactor $\alpha = 4$ points towards eight independent transport channels. For SnTe an even number of Dirac cones has been observed ranging from two to four depending on the crystallographic surface [203]. However, fits at different temperatures show a gradual decrease of both fitting parameters (Figure 5.1 c). This trend is in contrast to theory, which predicts that the number of transport channels should either remain constant or change by an integer number.

By tilting the sample within the B-field, the electronic dimensionality of a WAL-like feature can be tested. All contacted nanowires show no angular dependency of the WAL feature, suggesting that it is not a 2 D effect (Figure 5.2 b) but rather a 3 D effect. In recent transport studies on SnTe nanostructures similar effects have been observed [202], and attributed to a 3 D WAL-effect. However, the temperature behavior of the resistance ($\rho(T)/\rho(300K)$) in Figure 5.2 a) shows no monotonic

---

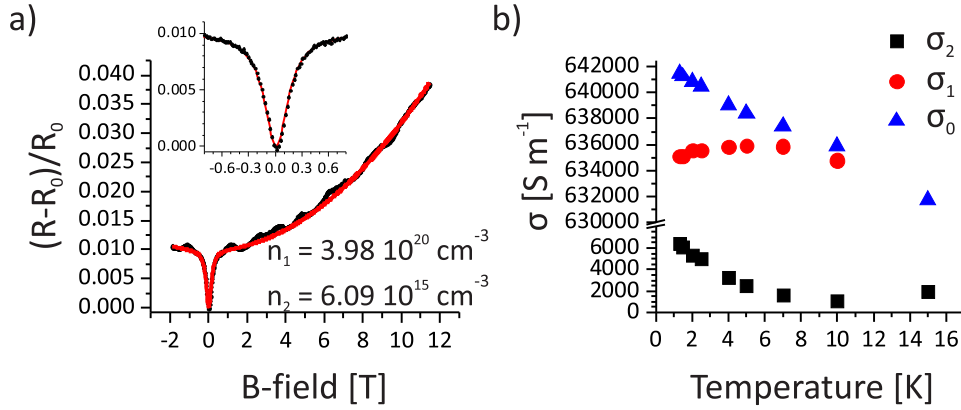[1]one flux correspondence to e^2/h

Fig. *5.3: a) Fit of the magnetoresistance of a SnTe nanowire (T = 1.3 K) to eq. 5.1 with an additional quadratic term to account for the background. b) Conductivities extracted from the fits in panel a) for different temperatures. Here σ_0 denotes the measured total conductivity.*

resistance decrease upon lowering the temperature, as would be expected in the presence of WAL (see Figure 2.4 b). Instead, the resistance follows a straight line between 1.4 K and 30 K when phonons start to be populated. As the resistance should further decrease with decreasing temperature, a WAL contribution can hence be excluded.

The presence of two distinct types of charge carriers cannot only give rise to a quadratic MR, but also causes a WAL-like feature at low B-fields. For heavily p-doped SnTe bulk samples a second valence band contributing to charge transport has been observed [204]. The corresponding correction to ρ is given by

$$\frac{\rho(B) - \rho(B=0)}{\rho(B=0)} = \frac{\sigma_1 \sigma_2 \left(n_1 \sigma_2 + n_2 \sigma_1\right)^2 B^2}{\left[e n_1 n_2 \left(\sigma_1 + \sigma_2\right)\right]^2 + \left(n_1 - n_2\right)^2 \sigma_1^2 \sigma_2^2 B^2} \tag{5.1}$$

which reduces to three independent variables by using $\rho_0 = \frac{1}{\sigma_1 + \sigma_2}$ [29, 205].

Fitting the above equation to the data in Figure 5.2 yields reasonable fits, as demonstrated by Figure 5.3 a). The conductivities associated with two charge carriers differ by two orders of magnitude ($\sigma_1 = 6.3 \cdot 10^5, \sigma_2 = 6.3 \cdot 10^3$ S/m), and can be characterized as metallic for the majority carrier ($\sigma \gtrsim 1 \cdot 10^4$ S/m [33]), in agreement with the observed temperature dependence. The extracted charge carrier densities of $n_1 = 3.98 \cdot 10^{20}$ cm^{-3} ($n_2 = 6.1 \cdot 10^{15}$ cm^{-3}) are in the range of the densities obtained from Hall effect measurements on platelets. These are with $8.5 \cdot 10^{20}$ cm^{-3} only slightly higher and in accordance with previously reported values for SnTe [200, 201]. Contacted platelets did not show any pronounced MR features. Attempts to tune the carrier density via electrostatic gating only showed little response on the resistivity. These findings confirm that the material is heavily p-doped. The phase transition (Fig. 1.4 b) is suppressed by a stabilized cubic crystal structure due to the high

carrier concentration. At the same time, this implies that the Fermi level lies well inside the valence band, rendering the surface states invisible in charge transport experiments.

5.2 Spin transport in SnTe nanowires
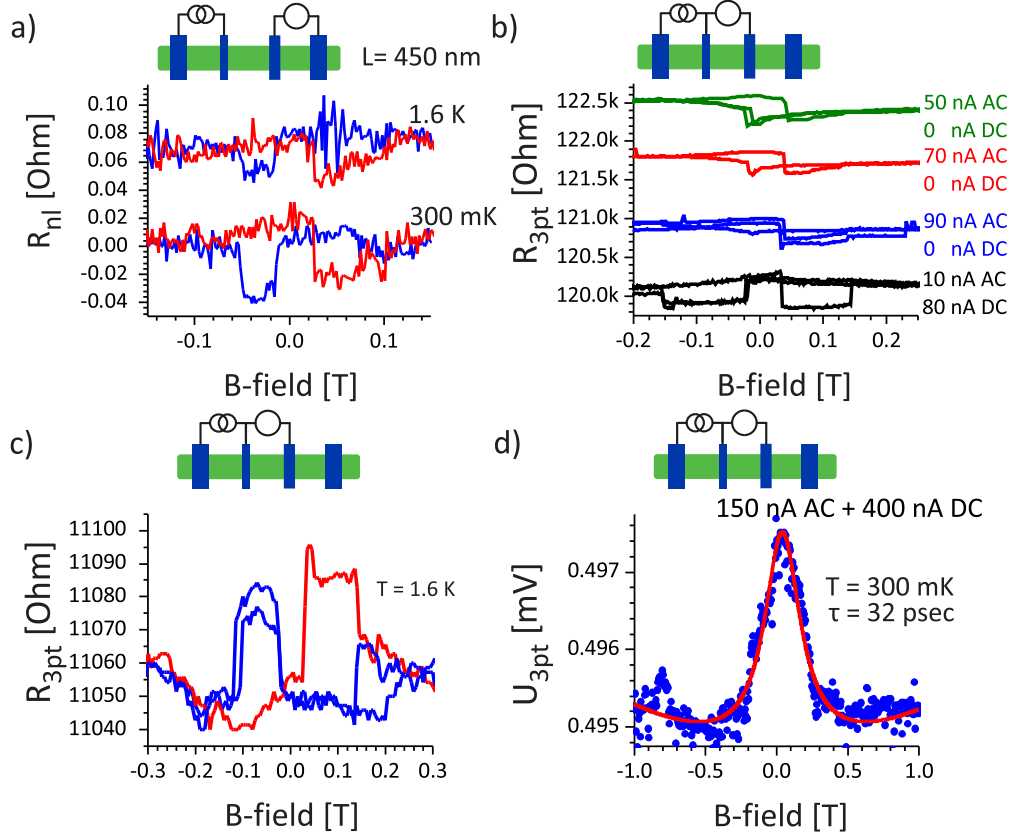
Fig. 5.4: *a) Nonlocal spin-valve effect observed for a SnTe nanowire at two temperatures. b) AC stimulus dependent three-point spin-valve measurements. With a combined AC-DC stimulus a two step switching behavior can be obtained. c) In-plane magnetoresistance showing a two-step switching behavior. d) Hanle curve fitted with eq. 2.25 (red line), yielding a spin life time of 32 ps.*

Encouraged by the results of the graphene stripes, SnTe nanowires with a diameter below 60 nm are contacted with transparent ferromagnetic contacts, following the procedure used for the AuPd contacts. The as-contacted wires display a two-step nonlocal spin valve effect of $20\,\mathrm{m\Omega}$ at 1.6 K on a linear MR background, as exemplified in Figure 5.4 a). Cooling the sample from 1.6 K down to 300 mK doubles ΔR_{nl}. The nonlocal spin signal has been detected with an excitation current of 300 nA, which corresponds to a current density of $8 \cdot 10^7\,\mathrm{A/m}$. Such high density causes the wires to

break easily due to Joule heating. To minimize this effect, three-point measurements are carried out in the following.

Figure 5.4 b) reveals an incomplete three-point spin signal already for an AC bias of 50 nA. Increasing the AC stimulus does not restore the full two level switching. Only with a combined AC/DC stimulus it is possible to observe a clear two-step switching. For three-point measurements performed under out-of-plane B-field sweeps, the Hanle effect is observed. Fitting of the Hanle data by equation 2.25 affords a spin life time of 32 ps. It should be noted that not for all contact configurations that showed a spin-valve effect, a Hanle curve could be recorded. Instead a flat MR trace was obtained.

Spin valve devices fabricated by a two-step process showed a three-point resistance between 18 kΩ and 44 kΩ. During this process, the contact pretreatment by argon plasma is done in a separate chamber, making it necessary to break the vacuum to transfer the sample to the evaporation chamber. This could be managed within 30 s from breaking the vacuum until starting the pumps again.

Improved reproducibility was achieved by a one-step process inside a special chamber allowing for *in-situ* argon plasma treatment. In this case, three-point resistances below 1 kΩ were reached, strongly suggesting that devices fabricated by the two-step process comprised an oxide barrier, which prevents transparent contacts. The oxide most likely consists of SnO_2 and TeO_3, formed upon contact with the ambient. For the one-step process, an increased $R_c > 8$ kΩ could be obtained on purpose by introducing O_2 in the chamber for 15 min at $1 \cdot 10^{-4}$ mbar after plasma treatment. Devices prepared in this manner again displayed the spin-valve effect.

5.3   Conclusion

Two different types of SnTe nanostructures have been grown by PVD and characterized by TEM. In electrical transport measurements on the SnTe nanowires, a distinct feature emerged at low magnetic fields, which could be fitted with the HNL formula describing 2 D WAL. However, the observed temperature dependency is incompatible with the presence of WAL. Data fits with a two band model yielded reasonable conductivities which are in agreement with Hall measurements on SnTe nanoplatelets. Thus derived carrier densities fit well to results that were recently obtained by other groups. These related studies found WAL-like features for nanowires and attributed them to the 3 D WAL effect.

In spin transport experiments using a nonlocal measurement scheme, a spin signal could be detected over a distance of 450 nm. Corresponding Hanle measurements in three-point configuration yielded a spin lifetime of 32 ps, a value falling into the range reported for p-doped Si [206].

6 Summary and outlook

The central focus of this thesis was the study of the low temperature charge and spin transport in Dirac materials. Two members of this intriguing class of materials, namely graphene and Tin(II)telluride (SnTe), were investigated. While both host massless fermions, they differ in several aspects. Graphene is a two-dimensional material, whose electronic properties are well understood these days. In contrast, Tin(II)telluride is considered to be a member of the topological crystalline insulator class, whose existence has until now only been confirmed by ARPES measurements. It is a three-dimensional material possessing two-dimensional states within the band gap.

In the present thesis, the impact of covalent functionalization of graphene on its electronic properties was explored in detail. Upon testing different solvents as reaction medium for the aromatic diazonium salt-based covalent attachment of substituted phenyl groups, ethanol was found to be the best solvent. In particular, it allows for an enhanced reaction rate, which in principle could favor the kinetic reaction path. The kinetically controlled product has been predicted by theory to contain unpaired electrons which are confined to one of the two graphene sublattices. Based upon previously reported SQUID experiments, from which magnetic coupling between the unpaired electrons was concluded [19], the present thesis aimed at gaining a complementary, charge transport-based proof for this phenomenon and to study it in further detail.

As a first step, a relatively short reaction time was used for the graphene functionalization. This caused a deterioration of the charge transport properties that is consistent with the introduction of sp^3 carbon centers and the associated structural disorder. From the thus induced weak localization effect, the phase coherence length of the electrons was extracted. Quantities like the carrier mobility, scattering times and temperature behavior of the resistivity were found to be affected by the functionalization in a similar manner as previously reported.

The use of a tenfold longer reaction time resulted in a pronounced change of the charge transport behavior. Specifically, the electrical resistivity of the strongly

functionalized graphene was found to increase upon cooling, while the mobility saturates at high charge carrier densities. Moreover, the emerging WL has doubled in magnitude compared to the shorter reaction time. At the same time, the dependency of the phase coherence length on the charge carrier density has changed from inverse to direct proportionality. In addition, the dephasing rate of the phase coherence is not any more linearly dependent on temperature, but needs instead to be described by a polynomial of second order. The origin of the saturation of the phase coherence length observed below 2 K needs further clarification. Possible explanations involve zero point fluctuations as an intrinsic property of the system, or a spin-dependent contribution to the phase coherence time which, based upon the observed saturation magnitude, could only be due to magnetic impurities. The situation is complicated by the fact that the functionalization might introduce both disorder and magnetic impurities by the unpaired electrons. Hence, the presently available data do not allow to unequivocally distinguish between these two possibilities. Nonetheless, the observation that the saturation value depends on the charge carrier density, and furthermore that the ratio of mean free path and phase coherence length gives a straight line, speaks in favor of the magnetic impurities as the cause of saturation.

In order to explore the impact of the functionalization on the spin (transport) properties of graphene, first the conventional strategy comprising an inorganic oxide tunneling barrier was followed to overcome the conductivity mismatch problem at the interface between graphene and ferromagnetic metal. For this purpose, a small amount of Ti was initially evaporated, followed by oxidation of the ultrathin metal layer by oxygen exposure. Subsequently, alumina was deposited on top via atomic layer deposition, in order to close residual pinholes in the oxide. Thus obtained spin-valve devices displayed a decoupled switching characteristic for the ferromagnetic contacts. However, as the oxide barriers lacked sufficient stability, an alternative approach had to be followed. This involved reducing the contact area to increase the contact resistance, which enabled spin polarizations of up to 24 %. Covalent functionalization of the stripes led to a notable reduction of the spin diffusion length. The observed increase of spin polarization could be due to the functionalization or, alternatively, the unavoidable thermal cycling of the sample. At the present status, insufficient data is available to exclude the latter possibility.

In case of the SnTe, the major objective was to detect signatures of its surface states. Both, SnTe nanowires and nanoplatelets were obtained through a physical vapor deposition process, where the temperature was used to control the morphology. The chemical composition of the obtained nanostructures was confirmed by electron diffraction and energy dispersive X-ray spectroscopy (EDX). Low temperature magnetotransport studies on nanowires revealed pronounced, weak antilocalization-like

features that were ascribed to the presence of two independent types of carriers contributing to charge transport. The charge carrier densities obtained from fits to a two-band model are in agreement with the values extracted from Hall measurements on the nanoplatelets. They indicate strong intrinsic p-type doping, which drives the Fermi level well into the valence band. Spin transport measurements on SnTe nanowires demonstrated a spin-valve effect similar to observations on semiconductors. The spin lifetime of 32 ps for the SnTe lies within the range reported for silicon under similar doping conditions.

Future experiments could aim at fully characterizing the spin transport characteristics of the covalently functionalized graphene. Further valuable information could be gained by simultaneously applying a constant out-of-plane B-field while sweeping the in-plane B-field. The resulting manipulation of the magnetic moment should alter the saturation behavior of the weak localization. Such experiments would require a cryostat with a variable temperature insert operating below 2 K, equipped with a vector magnet. Furthermore, spin transport experiments could be performed by adding two additional terminals to the stripe, in order to enable determining the mobility from Hall data acquired during the same experimental run. By comparing the spin lifetime with the mobility, a change of the spin dephasing mechanism should be better visible [207]. For the graphene stripes, it would be interesting to further decrease their width to enhance the influence of the edges. In this context, it is relevant that the edge terminations may exert spin polarization effects, as predicted by theory [208, 209]. Regular graphene edges are in principle accessible through anisotropic etching [210]. Moreover, synthetic graphene nanoribbons (GNRs) could be used to explore the ultimately narrow case [211]. Such bottom-up ribbons offer the advantage that the edge configuration is controllable by the synthesis scheme. In preliminary experiments performed in the last stage of this thesis on GNRs, higher harmonic Raman modes have been observed, which might result from the narrow confinement in these ribbons. It was also attempted to electrically contact individual GNRs, which however did not succeed.

Regarding the SnTe, it would be worthwhile to determine the effect of incorporating lead, in order to reduce the intrinsic p-doping. In fact, according to recent ARPES studies on $Pb_{1-x}Sn_xTe$, a lead content of up to $1 - x \approx 0.75$ still leaves the surface states intact while increasing the fermi energy close to the band gap [212]. For higher Pb contents, the band inversion is lifted and a normal semiconductor formed. Once charge transport-based evidence for the surface states of $Pb_{1-x}Sn_xTe$ would have been gained, the spin transport properties could be explored in detail. Here, the ultimate goal would be a high performance spin filter that has a spin polarization close to 100 %, which can be grown by epitaxy on graphene.

Bibliography

[1] Bell Labs, "alcatel-lucent.com,"

[2] "www.heise.de,"

[3] Texas Instruments, "www.ti.com."

[4] "www.nobelprize.org,"

[5] "www.intel.de,"

[6] C. Chappert, A. Fert, and F. N. van Dau, "The emergence of spin electronics in data storage," *Nature Materials*, vol. 6, pp. 813–823, 2007.

[7] "www.ibm.com,"

[8] T. Coughlin *www.forbes.com.*

[9] S. Datta and B. Das, "Electronic analog of the electro-optic modulator," *Applied Physics Letters*, vol. 56, no. 7, pp. 665–667, 1990.

[10] S. A. Wolf, D. D. Awschalom, R. A. Buhrman, J. M. Daughton, S. von Molnár, M. L. Roukes, A. Y. Chtchelkanova, and D. M. Treger, "Spintronics: A Spin-Based Electronics Vision for the Future," *Science*, vol. 294, no. 5546, pp. 1488–1495, 2001.

[11] B. T. Jonker, G. Kioseoglou, A. T. Hanbicki, C. H. Li, and P. E. Thompson, "Electrical spin-injection into silicon from a ferromagnetic metal/tunnel barrier contact," *Nature Physics*, vol. 3, pp. 542–546, Aug. 2007.

[12] K. S. Novoselov, A. K. Geim, S. V. Morozov, D. Jiang, Y. Zhang, S. V. Dubonos, I. V. Grigorieva, and A. A. Firsov, "Electric Field Effect in Atomically Thin Carbon Films," *Science*, vol. 306, no. 5696, pp. 666–669, 2004.

[13] Z. K. Liu, B. Zhou, Y. Zhang, Z. J. Wang, H. M. Weng, D. Prabhakaran, S.-K. Mo, Z. X. Shen, Z. Fang, X. Dai, Z. Hussain, and Y. L. Chen, "Discovery of a Three-Dimensional Topological Dirac Semimetal, Na_3Bi," *Science*, vol. 343, no. 6173, pp. 864–867, 2014.

[14] O. M. J. van 't Erve, A. L. Friedman, E. Cobas, C. H. Li, A. T. Hanbicki, K. M. McCreary, J. T. Robinson, and B. T. Jonker, "A graphene solution to conductivity mismatch: Spin injection from ferromagnetic metal/graphene tunnel contacts into silicon," *Journal of Applied Physics*, vol. 113, no. 17, pp. –, 2013.

[15] W. Han, R. K. Kawakami, M. Gmitra, and J. Fabian, "Graphene spintronics," *Nature Nanotechnology*, vol. 9, pp. 794–807, Oct. 2014.

[16] L. Banszerus, M. Schmitz, S. Engels, M. Goldsche, K. Watanabe, T. Taniguchi, B. Beschoten, and C. Stampfer, "Ballistic transport exceeding 28 μm in CVD grown graphene," *arxiv:1511.08601*.

[17] N. Tombros, C. Jozsa, M. Popinciuc, H. T. Jonkman, and B. J. van Wees, "Electronic spin transport and spin precession in single graphene layers at room temperature," *Nature*, vol. 448, pp. 571–574, 2007.

[18] J. Ingla-Aynés, M. H. D. Guimarães, R. J. Meijerink, P. J. Zomer, and B. J. van Wees, "24-μm spin relaxation length in boron nitride encapsulated bilayer graphene," *Physical Review B*, vol. 92, p. 201410, Nov 2015.

[19] J. Hong, E. Bekyarova, W. A. de Heer, R. C. Haddon, and S. Khizroev, "Chemical Engineered Graphene-Based 2 D Organic Molecular Magnet," *ACS Nano*, vol. 7, no. 111, pp. 10011–10022, 2013.

[20] R. R. Nair, M. Sepioni, I.-L. Tsai, O. Lehtinen, J. Keinonen, A. V. Krasheninnikov, T. Thomson, A. K. Geim, and I. V. Grigorieva, "Spin-half paramagnetism in graphene induced by point defects," *Nature Physics*, vol. 8, pp. 199–202, Mar. 2012.

[21] Z. Wang, C. Tang, R. Sachs, Y. Barlas, and J. Shi, "Proximity-Induced Ferromagnetism in Graphene Revealed by the Anomalous Hall Effect," *Physical Review Letters*, vol. 114, p. 016603, Jan 2015.

[22] A. Avsar, J. Y. Tan, T. Taychatanapat, J. Balakrishnan, G. K. W. Koon, Y. Yeo, J. Lahiri, A. Carvalho, A. Rodin, E. C. T. O'Farrel, G. Eda, and A. H. A. H. C. N. Özyilmaz, "Spin-orbit proximity effect in graphene," *Nature Communications*, vol. 5, no. 4875, 2014.

[23] C. L. Kane and E. J. Mele, "Z_2 Topological Order and the Quantum Spin Hall Effect," *Physical Review Letters*, vol. 95, p. 146802, Sep 2005.

[24] B. A. Bernevig, T. L. Hughes, and S.-C. Zhang, "Quantum Spin Hall Effect and Topological Phase Transition in HgTe Quantum Wells," *Science*, vol. 314, no. 5806, pp. 1757–1761, 2006.

[25] Y. Ando, "Topological Insulator Materials," *Journal of the Physical Society of Japan*, vol. 82, p. 102001, 2013.

[26] D.Kong and Y. Cui, "Opportunities in chemistry and materials science for topological insulators and their nanostructures," *Nature Chemistry*, vol. 3, pp. 845–849, 2011.

[27] L. H., van /'t ErveO. M. J., R. T., LiuY., LiL., and J. T., "Electrical detection of charge-current-induced spin polarization due to spin-momentum locking in Bi_2Se_3," *Nature Nanotechnology*, vol. 9, no. 3, pp. 218–224, 2014.

[28] D. Pesin and A. H. MacDonald, "Spintronics and pseudospintronics in graphene and topological insulators," *Nature Materials*, vol. 11, pp. 409–416, May 2012.

[29] N. W. Ashcroft and D. N. Mermin, *Festkörperphysik.* Oldenbourg Wissenschaftsverlag, 3te ed.

[30] G. Blatter, ed., *Skriptum Festkörperphysik.* 2006.

[31] T. O. Wehling, A. Black-Schaffer, and A. Balatsky, "Dirac materials," *Advances in Physics*, vol. 63, no. 1, pp. 1–76, 2014.

[32] J. Cayssol, "Introduction to Dirac materials and topological insulators," *Comptes Rendus Physique*, vol. 14, pp. 760–778, 2013.

[33] J. Weiss, *Skriptum Halbleiterphysik.* TU Stuttgart, 2013.

[34] F. Schwabl, *Quantenmechanik I.* Springer-Verlag, 6 ed., 2002.

[35] J. Sullivan, "http://torus.math.uiuc.edu/jms/java/dragsphere/."

[36] Y. Ando and L. Fu, "Topological Crystalline Insulator and Topological Superconductors: From Concepts to Materials," *Annual Review of Condensed Matter Physics*, vol. 6, pp. 361–381, 2015.

[37] M. Hasan and C. Kane, "Colloquium: Topological Insulators," *Review of Modern Physics*, vol. 82, p. 3045–3067, 2010.

[38] P. Yu and M. Cardona, *Fundamentals of Semiconductors.* Springer-Verlag Berlin Heidelberg, 4th ed., 2010.

[39] J. E. Avron, D. Osadchy, and R. Seiler, "A topological look at the Quantum Hall effect," *Physics Today*, no. 38-42, 2003.

Bibliography

[40] J. C. Y. Teo, L. Fu, and C. L. Kane, "Surface states and topological invariants in three-dimensional insulators: Aplication to $Bi_{1-X}Sb_x$," *Physical Review B*, vol. 78, p. 045426, 2008.

[41] L. Fu, C. L. Kane, and E. J. Mele, "Topological Insulators in Three Dimensions," *Physical Review Letters*, vol. 98, p. 106803, 2007.

[42] L. Fu and C. L. Kane, "Topological insulators with inversion symmetry," *Physical Review B*, vol. 76, 2007.

[43] J. E. Moore and L. Balents, "Topological invariants of time-reversal-invariant band structures," *Physical Review B*, vol. 75, p. 121306, 2007.

[44] T. H. Hsieh, H. Lin, J. Liu, W. Duan, A. Basil, and L. Fu, "Topological crystalline insulators in the SnTe material class," *Nature Communications*, vol. 3, no. 982, pp. 1–5, 2012.

[45] H. Maier and J. Hessse, *Organic Crystals, Germanates, Semiconductors*. Springer-Verlag, crystals - growth, properties and applications; 4 ed., 1980.

[46] J. O. Dimmock, I. Melngailis, and A. J. Strauss, "Band Structure and Laser Action in $Pb_xSn_{1-X}Te$," *Physical Review Letters*, vol. 16, no. 26, pp. 1193–1196, 1966.

[47] O. A. Pankratov, S. V. Pakhomov, and B. A. Volkov, "Supersymmetry in hetero-junctions: Band-inverting contact on the basis of $Pb_{1-x}Sn_xTe$ and $Hg_{1-x}Cd_xTe$," *Solid State Communications*, vol. 61, no. 2, pp. 93–96, 1987.

[48] Y. Tanaka, Z. Ren, T. Sato, K. Nakayama, S. Souma, T. Takahashi, K. Segawa, and Y. Ando, "Experimental realization of the topological crystalline insulator SnTe," *Nature Physics*, vol. 8, pp. 800–803, 2012.

[49] M. Iizumi, Y. Hamaguchi, K. F. Komatsubara, and Y. Kato, "Phase Transition in SnTe with Low Carrier Concentration," *Journal of the Physical Society of Japan*, vol. 38, no. 2, pp. 443–449, 1975.

[50] Y. Takafuji and S.-I. Narita, "Shubnikov-de Haas Measurements in N-Type $Pb_{1-x}Sn_xTe$," *Japanese Journal of Applied Physics*, vol. 21, no. 9, pp. 1315–1322, 1982.

[51] D. L. Mitchell and R. F. Wallice, "Theoretical Energy-Band Parameters for the Lead Salts," *Physical Review*, vol. 151, p. 581, 1966.

[52] S. Xu, C. Liu, N. Alidoust, M. Neupane, D. Qian, I. Belopolski, J. D. Denlinger, Y. J. Wang, H. Lin, L. A. Wray, G. Landolt, B. Slmoski, J. H. Dill, A. Marcinkova,

E. Morosan, Q. Gibson, R. Sankar, F. C. Chou, R. J. Cava, A. Bansil, and M. Z. Hasan, "Observation of a topological crystalline insulator phase and topological phase transition in $Pb_{1-x}Sn_xTe$," *Nature Communications*, vol. 3, no. 1192, 2012.

[53] L. J. Brillson, E. Burstein, and L. Muldawer, "Raman Observation of the ferroelectric phase transition in SnTe," *Physical Review B*, vol. 9, no. 4, pp. 1547–1551, 1974.

[54] S. Sugai, K. Murase, and H. Kawamura, "Observation of soft TO-phonon in SnTe by Raman scattering," *Solid State Communications*, vol. 23, no. 2, pp. 127–129, 1977.

[55] W. Richter, H. Koehler, and C. R. Becker, "A Raman and far-infrared investigation of phonons in the rhombohedral V_2-VI_3 compounds Bi_2Te_3, Bi_2Se_3, Sb_2Te_3 and $Bi_2(Te_{1-x}Se_x)_3$ ($0 < x < 1$), $(Bi_{1-y}Sb_y)_2Te_3$ ($0 < y < 1$)," *Physica Status Solidi B: Basic Solid State Physics*, vol. 84, no. 2, pp. 619–628, 1977.

[56] A. H. C. Neto, F. Guinea, N. M. R. Peres, K. S. Novoselov, and K. Geim, "The electronic properties of graphene," *Reviews of Modern physics*, vol. 81, pp. 109–162, 2009.

[57] L. E. F. F. Torres, S. Roche, and J.-C. Charlier, *Introduction to Graphene-Based Nanomaterials: From Electronic Structure to Quantum Transport.* Cambridge University Press, 2014.

[58] C. Lee, X. Wei, J. W. Kysar, and J. Hone, "Measurements of the Elastic Properties and Intrinsic Strength of Monolayer Graphene," *Sciene*, vol. 321, no. 5887, pp. 385–388, 2008.

[59] P. R. Wallace, "The Band Theory of Graphite," *Physical Review*, vol. 71, pp. 622–634, 1947.

[60] J. Mañes, F. Guinea, and M. Vozmediano, "Existence and topological stability of Fermi points in multilayered graphene," *Physical Review B*, vol. 75, p. 155424, 2007.

[61] P. L. McEuen, M. Bockrath, D. H. Cobden, Y.-G. Yoon, and S. G. Louie, "Disorder, Pseudospins and Backscattering in Carbon Nanotubes," *Physical Review Letters*, vol. 83, pp. 5098–6001, 1999.

[62] J. Mannhart, "Quantum Heterostructures 2," University of Stuttgart, Summerterm 2013.

[63] M. S. Fuhrer, "Diffusive Charge Transport in Graphene,"

Bibliography

[64] J. Martin, N. Akerman, G. Ulbricht, T. Lohmanm, J. H. S. ad K. von Klitzing, and A. Yacoby, "Observation of electron-hole puddles in graphene using a scanning single-electron transistor," *Nature Physics*, vol. 4, no. 2, pp. 144–148, 2008.

[65] M. Oksanen, A. Uppstu, A. Laitinen, D. J. Cox, M. F. M. F. C. Russo, A. Harju, and P. Hakonen, "Single-mode and multimode Fabry-Pérot interference in suspended graphene," *Physical Review B*, vol. 89, p. 121414, 2012.

[66] C. W. J. Beenakker, "Colloquium: Andreev reflection and Klein tunneling in graphene," *Review of Modern Physics*, vol. 80, pp. 1337–1354, 2008.

[67] A. C. Ferrari, "Raman spectroscopy of graphene and graphite: Disorder, electron-phonon coupling, doping and nonadiabatic effects," *Solid State Communications*, vol. 143, pp. 47–57, 2007.

[68] L. G. Cancado, A. Reina, J. Kong, and M. S. Dresselhaus, "Geometrical appproach for the study of the G' band in the Raman spectrum of monolayer graphene, bilayer graphene and bulk graphite," *Physical Review B: Condensed Matter and Materials Physics*, vol. 77, p. 245408, 2008.

[69] C. Cervetti, E. Heintze, B. Gorshunov, E. Zhukova, S. Lobanov, A. Hoyer, M. Burghard, K. Kern, M. Dressel, and L. Bogani, "Sub-Terahertz Frequency-Domain Spectroscopy Reveals Single-Grain Mobility and Scatter Influence of Large-Area Graphene," *Advanced Materials*, vol. 27, no. 16, pp. 2635–41, 2015.

[70] A. Das, S. Pisana, B. Chakraborty, S. Piscanec, S. K. Saha, U. V. Waghmare, K. S. K. S. N. R. Krishnamurthy, A. K. A. K. G. C. Ferrari, and A. K. Sood, "Monitoring dopands by Raman scattering in an electrochemically top-gated graphene transistor," *Nature Nanotechnology*, vol. 3, pp. 210–215, 2008.

[71] L. M. Malard, M. A. Pimenta, G. Dresselhaus, and M. S. Dresselhaus, "Raman spectroscopy in graphene," *Physics Reports*, vol. 473, pp. 51–87, 2009.

[72] L. G. Cançado, A. Jorio, E. H. M. Ferreira, F. Stavale, C. A. Achete, R. B. Capaz, M. V. O. Moutinho, A. Lombardo, T. S. Kulmala, , and A. C. Ferrari, "Quantifying Defects in Graphene via Raman Spectroscopy at Different Excitation Energies.," *Nano Letters*, vol. 11, no. 8, pp. 3190–3196, 2011.

[73] R. Konnerth, C. Cervetti, A. Narita, X. Feng, K. Muellen, A. Hoyer, M. Burghard, K. Kern, M. Dressel, and L. Bogani, "Tuning the deposition of molecular graphene nanoribbons by surface functionalization," *Nanoscale*, vol. 7, pp. 12807–12811, 2015.

[74] M. M. Lucchese, F. S. S. H. M. Ferreira, C. Vilani, M. V. O. Moutinho, R. B. Capaz, C. A. Achete, and A. Jorio, "Quantifying ion-induced defects and Raman relaxation length in graphene," *Carbon*, vol. 48, pp. 1592–1597, 2010.

[75] A. Eckmann, A. Felten, I. Verzhbitskiy, R. Davey, and C. Casiraghi, "Raman study on defective graphene: Effect of the excitation energy, type and amount of defects," *Physical Review B*, vol. 88, p. 035426, 2013.

[76] A. Eckmann, A. Felten, A. Mishchenko, L. Britnell, R. Krupke, K. S. Novoselov, and C. Casiraghi, "Probing the Nature of Defects in Graphene by Raman Spectroscopy," *Nano Letters*, vol. 12, no. 8, pp. 3925–3930, 2012.

[77] J. Cayssol, *Various probes of Dirac matter: from graphene to topological insulators.* PhD thesis, Bordeaux 1, 2012.

[78] J. Eroms and D. Weiss, "Weak localization and transport gap in graphene antidot lattices," *New Journal of Physics*, vol. 11, no. 9, p. 095021, 2009.

[79] M. Y. Han, B. Özyilmaz, Y. Zhang, and P. Kim, "Energy Band-Gap Engineering of Graphene Nanoribbons," *Physical Review Letters*, vol. 98, p. 206805, 2007.

[80] E. Bekyarova, S. Sarkar, F. Wang, M. E. Itkis, I. Kalinina, X. Tian, and R. C. Haddon, "Effect of Covalent Chemistry on the Electronic Structure and Properties of Carbon Nanotubes and Graphene," *Accounts of Chemical Research*, vol. 46, no. 1, pp. 65–76, 2012.

[81] A. G. Swartz, J. Chen, K. M. McCreary, P. M. Odenthal, W. Han, and R. K. Kawakami, "Effect of in situ deposition of Mg adatoms on spin relaxation in graphene," *Physical Review B*, vol. 87, p. 075455, 2013.

[82] K. M. McCreary, A. G. Swartz, W. Han, J. Fabian, and R. K. Kawakami, "Magnetic Moment Formation in Graphene Detected by Scattering of Pure Spin Currents," *Physical Review Letters*, vol. 109, p. 186604, 2012.

[83] L. Kou, F. Hu, B. Yan, T. Frauenheim, and C. Chen, "Opening a band gap with breaking lattice symmetry: a new route towards robust graphene-based nanoelectronics," *Nanoscale*, vol. 6, pp. 7474–7479, 2014.

[84] A. K. Geim and I. V. Grigorieva, "Van der Waals heterostructures," *Nature*, vol. 499, pp. 419–425, 2013.

[85] G. L. C. Paulus, Q. H. Wang, and M. S. Strano, "Covalent Electron Transfer Chemistry of Graphene with Diazonium Salts," *Accounts of Chemical Research*, vol. 46, no. 1, pp. 160–170, 2012.

Bibliography

[86] X. Hong, K. Zou, B. Wang, S.-H. Cheng, and J. Zhu, "Evidence for Spin-Flip Scattering and Local Moments in Dilute Fluorinated Graphene," *Physical Review Letters*, vol. 108, p. 226602, 2012.

[87] M. S. S. Peng and Z. Liu, "Chemistry makes Graphene beyond Graphene," *Journal of the American chemical society*, vol. 136, pp. 12194–12200, 2014.

[88] S. Sarkar, E. Bekyarova, and R. C. Haddon, "Chemistry at the Dirac Point: Diels-Alder Reactivity of Graphene," *Accounts of Chemical Research*, vol. 45, no. 4, pp. 673–682, 2011.

[89] E. Bekyarova, M. E. Itkis, P. Ramesh, C. Berger, M. Sprinkle, W. A. de Heer, and R. C. Haddon, "Chemical Modification of Epitaxial Graphene: Spontaneous Grafting of Aryl Groups," *Journal of the American Chemical Society*, vol. 131, pp. 1336–1337, 2009.

[90] J. Park and M. Yan, "Covalent Functionalization of Graphene with Reactive Intermediates," *Accounts of Chemical Research*, vol. 46, no. 1, pp. 181–189, 2012.

[91] F. M. Koehler and W. J. Stark, "Organic Synthesis on Graphene," *Accounts of Chemical Research*, vol. 46, no. 10, pp. 2297–2306, 2013.

[92] H. Zhang, E. Bekyarova, J. W. Huang, Z. Zhao, W. Bao, F. Wang, R. C. Haddon, and C. N. Lau, "Aryl Functionalization as a Route to Band Gap Engineering in Single Layer Graphene Devices," *Nano Letters*, vol. 11, pp. 4047–4051, 2011.

[93] F. M. Koehler, A. Jacobsen, T. Ihn, K. Ensslin, and W. J. Stark, "Chemical modification of graphene characterized by Raman and transport experiments," *Nanoscale*, vol. 4, pp. 3781–3785, 2012.

[94] D. A. Abanin and L. S. Levitov, "Conformal invariance and shape-dependent conductance of graphene samples," *Physical Review B*, vol. 78, p. 035416, 2008.

[95] I. Meric, M. Y. Han, A. F. Young, B. Ozyilmaz, P. Kim, and K. L. Shepard, "Current saturation in zero-bandgap, top-gated graphene field effect transistors," *Nature Communications*, vol. 3, pp. 654–659, 2008.

[96] T. Ihn, *Semiconductor Nanostructure*. Oxford University Press, 2011.

[97] Lake shore, *Appendix: A Hall Effect measurements*, 7500/9500 series hall systems ed.

[98] B. Huard, N. Stander, J. A. Sulpizio, and D. Goldhaber-Gordon, "Evidence of the role of contact on the observed electron-hole asymmetry in graphene," *Physical Review B*, vol. 78, p. 121402, 2008.

[99] H.-Z. Lu and S.-Q. Shen, "Weak localization and weak anti-localization in topological insulators," *Proc. Spie*, vol. Spintronics VII, 2014.

[100] S. Datta, *Electronic Transport in Mesoscopic Systems*. Cambridge University Press, 9th ed., 2009.

[101] S. Datta, *Lessons from Nanoelectronics*. World Scientific, 2012.

[102] G. Czycholl, *Theoretische Festkörperphysik*. Springer, 3rd ed., 2008.

[103] C. Kittel and C. Y. Fong, *Quantum Theory of Solids*. Wiley, 2nd ed., 1986.

[104] M. Monteverde, C. Ojeda-Aristizabal, K. B. R. Weil, M. Ferrier, S. Guron, C. Glattli, H. Bouchiat, J. N. Fuchs, and D. L. Maslov, "Transport and Elastic Scattering Times as Probes of the Nature of Impurity Scattering in Single-Layer and Bilayer Graphene," *Physical Review Letters*, 2010.

[105] E. H. Hwang and S. D. Sarma, "Single-particle relaxation time versus transport scattering time in a two-dimensional graphene layer," *Physical Review B*, vol. 77, p. 195412, 2008.

[106] X. Hong, K. Zou, and J. Zhu, "Quantum scattering time and its implications on scattering sources in graphene," *Physical Review B*, vol. 80, p. 241415, 2009.

[107] S. Hikami, A. I. Larkin, and Y. Nagaoka, "Spin-Orbit Interaction and Magnetoresistance in the Two Dimensional Random System," *Progress of Theoretical Physics*, vol. 63, no. 2, 1979.

[108] G. Bergmann, "Weak anti-localization - An experimental proof for the destructive interference of rotated spin 1/2 ," *Solid State Communications*, vol. 42, no. 11, pp. 815 – 817, 1982.

[109] E. McCann, K. Kechedzhi, V. I. Fal'ko, H. Suzuura, T. Ando, and B. L. Altshuler, "Weak-Localization Magnetoresistance and Valley Symmetry in Graphene," *Physical Review Letters*, 2006.

[110] F. V. Tikhonenko, A. A. Kozikov, A. K. Savchenko, and R. V. Gorbachev, "Transition between Electron Localization and Antilocalization in Graphene," *Physical Review Letters*, vol. 103, p. 226801, 2009.

[111] E. R. Mucciolo and C. H. Lewenkopf, "Disorder and electronic transport in graphene," *Journal of Physics: Condensed Matter*, vol. 22, no. 27, pp. 273201–273213, 2010.

Bibliography

[112] J. J. Lin and J. P. Bird, "Recent experimental studies of electron dephasing in metal and semiconductor mesoscopic structures," *Journal of Physics: Condensed Matter*, vol. 14, pp. 501–596, 2002.

[113] A. A. Kozikov, D. W. Horsell, E. McCann, and V. I. Fal'ko, "Evidence for spin memory in the electron phase coherence in graphene," *Physical Review B*, vol. 86, p. 045436, 2012.

[114] P. Mohanty, E. M. Q. Jariwala, and R. A. Webb, "Intrinsic Decoherence in Mesoscopic Systems," *Physical Review Letters*, vol. 78, pp. 3366–3369, Apr 1997.

[115] E. Y. Tsymbal and I. Zutic, *Handbook of Spin Transport and Magnetism*. CRC Press, 2012.

[116] I. Zutic, J. Fabian, and S. D. Sarma, "Spintronics: Fundamentals and applications," *Review of Modern Physics*, vol. 76, pp. 323–386, 2004.

[117] F. J. Jedema, M. S. Nijboer, A. T. Filip, and B. J. van Wees, "Spin injection and spin accumulation in all-metal mesoscopic spin valves," *Physical Review B*, vol. 67, p. 085319, 2003.

[118] S. P. Dash, S. Sharma, R. S. Patel, M. P. de Jong, and R. Jansen, "Electrical creation of spin polarization in silicon at room temperature," *Nature*, vol. 462, pp. 491–494, 2009.

[119] J. Nickel, "Magnetoresistance Overview," tech. rep., Hewlett Packard, 1995.

[120] B. Hausmanns, T. Krome, G. Dumpich, E. Wassermann, D. Hinzke, U. Nowak, and K. Usadel, "Magnetization reversal process in thin Co nanowires," *Journal of Magnetism and Magnetic Materials*, vol. 240, pp. 297–300, 2002.

[121] G. Schmidt, "Concepts for spin injection into semiconductors - a review," *Journal of Physics D: Applied Physics*, vol. 38, 2005.

[122] M. Brands, B. Leven, and G. Dumpich, "Influence of thickness and cap layer on the switching behavior of single Co nanowires," *Journal of Applied Physics*, vol. 97, p. 114311, 2005.

[123] M. Brands and G. Dumpich, "Multiple switching fields and domain wall pinning in single Co nanowires," *Journal of Physics D: Applied Physics*, vol. 38, pp. 822–826, 2005.

[124] M. Brands, R. Wieser, C. Hassel, D. Hinzke, and G. Dumpich, "Reversal processes and domain wall pinning in polycrystalline Co-nanowires," *Physical Review B*, vol. 74, p. 174411, 2006.

[125] G. Sarau and C. M. Schneider, "Magnetoresistance response of cobalt nanocontacts between extended magnetic electrodes," *Journal of Applied Physics*, vol. 102, p. 083907, 2007.

[126] J. S. Moodera and P. Leclair, "Spin electronics: A quantum leaps," *Nature Materials*, vol. 2, pp. 707–708, 2003.

[127] S. Takahashi and S. Maekawa, "Spin current, spin accumulation and spin Hall effect," *Science and Technology of Advanced Materials*, vol. 9, p. 014105, 2008.

[128] E. Villamor, M. Isasa, L. Hueso, and F. Casanova, "Temperature dependence of spin polarization in ferromagnetic metals using lateral spin valves," *Physical Review B*, vol. 88, p. 184411, 2013.

[129] G. Schmidt, D. Ferrand, L. W. Molenkamp, A. T. Filip, and B. J. van Wees, "Fundamental obstacle for electrical spin injection from a ferromagnetic metal into a diffusive semiconductor," *Physical Review B*, vol. 62, no. 8, pp. 4790–4793, 2000.

[130] E. I. Rashba, "Theory of electrical spin injection: Tunnel contacts as a solution of the conductivity mismatch problem," *Physical Review B*, vol. 62, no. 24, p. 16267, 2000.

[131] M. Johnson and R. H. Silsbee, "Interfacial charge-spin coupling: Injection and detection of spin magnetization in metals," *Physical Review Letters*, vol. 55, p. 1790, 1985.

[132] N. Tombros, S. J. van der Molen, and B. J. van Wees, "Separating spin and charge transport in single-wall carbon nanotubes," *Physical Review B*, vol. 73, p. 233403, 2006.

[133] S. Cho, Y.-F. Chen, and M. S. Fuhrer, "Gate-tunable graphene spin valve," *Applied Physics Letters*, vol. 91, no. 12, pp. –, 2007.

[134] M. Popinciuc, C. Józsa, P. J. Zomer, N. Tombros, A. Veligura, H. T. Jonkman, and B. J. van Wees, "Electronic spin transport in graphene field-effect transistors," *Physical Review B*, vol. 80, no. 21, pp. 214427–214440, 2009.

[135] F. Volmer, M. Drögeler, T. Pohlmann, G. Güntherodt, C. Stampfer, and B. Beschoten, "Contact-induced charge contributions to non-local spin transport measurements in co/mgo/graphene devices," *2D Materials*, vol. 2, no. 2, p. 024001, 2015.

Bibliography

[136] M. H. D. Buimaraes, J. J. van den Berg, I. J. Vera-Marun, P. J. Zomer, and B. J. van Wees, "Spin transport in graphene nanostructures," *Physical Review B*, vol. 90, p. 235428, 2014.

[137] J. Wu, H. Li, Z. Yin, H. Li, J. Liu, X. Cao, Q. Zhang, and H. Zhang, "Layer Thinning and Etching of Mechanically Exfoliated MoS_2 Nanosheets by Thermal Annealing in Air," *Small*, vol. 9, no. 19, pp. 3314–3319, 2013.

[138] Y. Liu, H. Nan, X. Wu, W. Pan, W. Wang, J. Bai, W. Zhao, L. Sun, X. Wang, and Z. Ni, "Layer-by-Layer Thinning of MoS_2 by Plasma," *ACS Nano*, vol. 7, no. 5, pp. 4202–4209, 2013.

[139] M. N. Ali, L. Schoop, J. Xiong, S. Flynn, Q. Gibson, M. Hirschberger, N. P. Ong, and R. J. Cava, "Correlation of Crystal Quality and Extreme Magnetoresistance of WTe_2," *arxiv:1506.04823*, 2015.

[140] C. Wongchoosuk, K. Subanajui, A. Menzel, I. A. Burshtein, S. T. ad Y. Lifshitz, and M. Zacharias, "Controlled Synthesis of ZnO Nanostructures: The Role of Source and Substrate Temperatures," *Journal of Physical Chemistry C*, vol. 115, pp. 757–761, 2011.

[141] A. Fasoli, A. Colli, S. Hofmann, C. Ducati, J. Robertson, and A. C. Ferrari, "Shape-selective synthesis of II–VI semiconductor nanowires," *Physica Status Solidi B*, vol. 243, no. 13, pp. 3301–3305, 2006.

[142] F. C. Meldrum and H. Cölfen, "Controlling Mineral Morphologies and Structures in Biological and Synthetic Systems," *Chemical Reviews*, vol. 108, pp. 4332–4432, 2008.

[143] D. P. Wei and Q. Chen, "Metal-Catalyzed CVD Method to Synthesize Silicon Nanobelts," *Journal of Physical Chemistry C*, vol. 112, pp. 15129–15133, 2008.

[144] R. S. Wagner and W. C. Ellis, "VAPORLIQUIDSOLID MECHANISM OF SINGLE CRYSTAL GROWTH," *Applied Physics Letters*, vol. 4, no. 5, pp. 89–90, 1964.

[145] V. A. C. F. V. Wittemann and U. Gösele, "Growth, Thermodynamics, and Electrical Properties of Silicon Nanowires," *Chemical Reviews*, vol. 110, pp. 361–388, 2010.

[146] P. Gehring, "private communication."

[147] P. Blake, E. W. Hill, A. H. C. Neto, K. S. Novoselov, D. Jiang, R. Yang, T. J. Booth, and A. K. Geim, "Making graphene visible," *Applied Physics Letters*, vol. 91, p. 063124, 2007.

[148] T. H. P. Chang, "Proximity effect in electron-beam lithography," *Journal of Vacuum Science and Technology*, vol. 12, p. 1271, 1975.

[149] M. A. Mohammad, M. Muhammad, S. K. Dew, and M. Stepanova, *Fundamentals of Electron Beam Exposure and Development*. Nanofabrication, Springer, 2012.

[150] S. Russo, M. F. Craciun, M. Yamamoto, A. F. Morpurgo, and S. Tarucha, "Contact resistance in graphene-base devices," *Physica E: Low-dimensional Systems and Nanostructures*, vol. 42, no. 4, pp. 677–679, 2010. 18th International Conference on Electron Properties of Two-Dimensional Systems.

[151] J. N. Longchamp, C. Escher, and H. W. Fink, "Ultraclean freestanding graphene by platinum-metal catalysis," *Journal of Vacuum Science & Technology, B*, vol. 31, p. 020605, 2013.

[152] H. W. Ott, *Noise Reduction techniques in electronic systems*. Wiley, 2nd ed., 1988.

[153] F. Fischer and M. Grayson, "Influence of voltmeter impedance on quantum Hall measurements," *Journal of Applied Physics*, vol. 98, p. 013710, 2005.

[154] "National Instruments LabVIEW: A Programming Environment for Laboratory Automation and Measurement," *Version 13.0*, 2013.

[155] P. Huang, L. Jing, H. R. Zhu, and X. Y. Gao, "Transport properties of diazonium functionalized graphene: chiral two-dimensional hole gases," *Journal of Physics: Condensed Matter*, 2012.

[156] S. D. D. S. Adam, E. H. Hwang, and E. Rossi, "Electronic transport in two-dimensional graphene," *Rev. Mod. Phys.*, vol. 83, no. 2, pp. 407–470, 2011.

[157] W. Zhu, J. Zhang, and Z. Yu, "Simulation study of channel mobility and device performance dependence on gate stack in graphene field-effect transistors," *Applied Physics Letters*, vol. 100, p. 112104, 2012.

[158] E. H. Hwang and S. D. Sarma, "Acoustic phonon scattering limited carrier mobility in two-dimensional extrinsic graphene," *Physical Review B*, vol. 77, no. 11, p. 115449, 2008.

[159] K. M. Burson, W. G. Cullen, S. Adam, C. R. Dean, K. Watanabe, T. Taniguchi, P. Kim, and M. S. Fuhrer, "Direct Imaging of Charged Impurity Density in Common Graphene Substrates," *Nano Letters*, vol. 13, no. 8, pp. 3576–3580, 2013.

[160] *Mathematic 10.2.0.0 for linux*.

Bibliography

[161] *Matlab 8.3.0.532 (R2014a) for linux.*

[162] F. V. Tikhonenko, D. W. Horsell, R. V. Gorbachev, and A. K. Savchenko, "Weak Localization in Graphene Flakes," *Physical Review Letters*, vol. 100, no. 5, p. 056802, 2008.

[163] D. Ki, D. Jeong, J. Choi, and H. Lee, "Inelastic scattering in a monolayer graphene sheet: A weak-localization study," *Physical Review B*, vol. 78, p. 125409, 2008.

[164] A. H. C. Neto and F. Guinea, "Impurity-Induced Spin-Orbit Coupling in Graphene," *Physical Review Letters*, vol. 103, no. 2, p. 026804, 2009.

[165] J. Chen, W. G. Cullen, C. Jang, M. S. Fuhrer, and E. D. Williams, "Defect Scattering in Graphene," *Physical Review Letters*, vol. 102, p. 236805, 2009.

[166] A. M. R. Baker, J. A. Alexander-Webber, T. Altebaeumer, T. J. B. M. Janssen, A. Tzalenchuk, S. Lara-Avila, S. Kubatkin, R. Yakimova, C.-T. Lin, L.-J. Li, and R. J. Nicholas, "Weak localization scattering lengths in epitaxial and CVD graphene," *Physical Review B*, vol. 86, no. 23, p. 235441, 2012.

[167] E. McCann and V. I. Fal'ko, "$z \to -z$ Symmetry of Spin-Orbit Coupling and Weak Localization in Graphene," *Physical Review Letters*, vol. 108, p. 166606, 2012.

[168] D. Ferry, S. Goodnick, and J. Bird, eds., *Transport in Nanostructures.* Cambridge, 2nd ed., 2009.

[169] Y. Qin, J. Han, G. Guo, Y. Du, Z. Li, Y. Song, L. Pi, X. Wang, X. Wan, M. Han, and F. Song, "Enhanced quantum coherence in graphene caused by Pd cluster deposition," *Applied Physics Letters*, vol. 106, no. 2, pp. –, 2015.

[170] L. Saminadayar, P. Mohanty, R. A. Webb, P. Degiovanni, and C. Bäuerle, "Electron coherence at low temperatures: The role of magnetic impurities," *Physica E: Low-dimensional Systems and Nanostructures*, vol. 40, no. 1, pp. 12–24, 2007. Proceedings of the International Workshop on Quantum Coherence, Noise and Decoherence in Nanostructures.

[171] B. Dlubak, M. Martin, C. Deranlot, B. Servet, S. Xavier, R. Mattana, M. Sprinkle, C. Berger, W. A. D. Heer, F. Petroff, A. Anane, P. Seneor, and A. Fert, "Highly efficient spin transport in epitaxial graphene on SiC," *Nature Physics*, vol. 8, pp. 557–561, 2012.

[172] S. Jandhyala, G. Mordi, B. Lee, G. Lee, C. Floresca, P.-R. Cha, J. Ahn, R. M. Wallace, Y. J. Chabal, M. J. Kim, L. Colombo, K. Cho, and J. Kim, "Atomic Layer Deposition of Dielectrics on Graphene Using Reversibly Physisorbed Ozone," *ACS Nano*, vol. 6, no. 3, pp. 2722–2730, 2012. PMID: 22352388.

[173] D. B. Farmer and G. Gordon, "Atomic Layer Deposition on Suspended Single-Walled Carbon Nanotubes via Gas-Phase Noncovalent Functionalization," *Nano Letters*, vol. 6, no. 4, pp. 699–703, 2006.

[174] X. Wang, S. M. Tabakman, and H. Dai, "Atomic Layer Deposition of Metal Oxides on Pristine and Functionalized Graphene," *Journal of American Chemical Society*, vol. 130, no. 26, pp. 8152–8153, 2008.

[175] B. Fallahazad, K. Lee, G. Lian, S. Kim, and C. M. Corbet, "Scaling of Al_2O_3 dielectric for graphene field-effect transistors," *Applied Physics Letters*, vol. 100, p. 093112, 2012.

[176] W. H. Wang, W. Han, K. Pi, K. M. McCreary, F. Miao, W. Bao, C. N. Lau, and R. K. Kawakami, "Growth of atomically smooth MgO films on graphene by molecular beam epitaxy," *Applied Physics Letters*, vol. 93, p. 183107, 2008.

[177] N. Y. Garces, V. D. Wheeler, and D. K. Gaskill, "Graphene functionalization and seeding for dielectric deposition and device integration," *Journal of Vacuum Science & Technology B*, vol. 30, p. 030801, 2012.

[178] C. A. Wilson, R. K. Grubbs, and S. M. George, "Nucleation and Growth during Al_2O_3 Atomic Layer Deposition on Polymers," *Chemistry of Materials*, vol. 17, no. 23, pp. 5625–5634, 2005.

[179] J. G. Simmons, "Electric Tunnel Effect between Dissimilar Electrodes Separated by a Thin Insulating Film," *Journal of Applied Physics*, vol. 34, no. 9, pp. 2581–2590, 1963.

[180] N. A. Tuan, P. L. Minh, and T. T. Dung, "Determination of the barrier parameters of Al_2O_3 layer in MTJs by Simmons and Brinkmans models," *Communications in Physics*, vol. 16, no. 1, pp. 7–11, 2006.

[181] I. Vaquila, M. P. Jr., and J. Ferrón, "Oxide stoichiometry in the early stages of titanium oxidation," *Surface Science*, vol. 292, no. 1–2, pp. L795 – L800, 1993.

[182] I. Vaquila, L. Vergara, M. P. Jr., R. Vidal, and J. Ferrón, "Chemical reactions at surfaces: titanium oxidation," *Surface and Coatings Technology*, vol. 122, no. 1, pp. 67 – 71, 1999.

[183] "http://www.keithley.com/products/dcac/sensitive/acdc/?mn=62212182A,"

[184] Y. Wu, V. Perebeinos, Y. ming Lin, T. Low, F. Xia, and P. Avouris, "Quantum Behavior of Graphene Transistors near the Scaling Limit," *Nano Letters*, vol. 12, no. 3, pp. 1417–1423, 2012. PMID: 22316333.

Bibliography

[185] H. T. Man, I. J. W. Wever, and A. F. Morpurgo, "Spin-dependent quantum interference in single-wall carbon nanotubes with ferromagnetic contacts," *Phys. Rev. B*, vol. 73, p. 241401, Jun 2006.

[186] M. H. D. Guimarães, P. J. Zomer, I. J. Vera-Marun, and B. J. van Wees, "Spin-Dependent Quantum Interference in Nonlocal Graphene Spin Valves," *Nano Letters*, vol. 14, no. 5, pp. 2952–2956, 2014. PMID: 24762101.

[187] K. Ono, H. Shimada, and Y. Ootuka, "Spin Polarization and Magneto-Coulomb Oscillations in Ferromagnetic Single Electron Devices," *Journal of the Physical Society of Japan*, vol. 67, no. 8, pp. 2852–2856, 1998.

[188] S. J. van der Molen, N. Tombros, and B. J. van Wees, "Magneto-Coulomb effect in spin-valve devices," *Phys. Rev. B*, vol. 73, p. 220406, Jun 2006.

[189] F. Volmer, M. Drögeler, E. Maynicke, N. von den Driesch, M. L. Boschen, G. Güntherodt, and B. Beschoten, "Role of MgO barriers for spin and charge transport in Co/MgO/graphene nonlocal spin-valve devices," *Phys. Rev. B*, vol. 88, p. 161405, Oct 2013.

[190] M. W. Iqbal, A. K. Singh, M. Z. Iqbal, and J. Eom, "Raman fingerprint of doping due to metal adsorbates on graphene," *Journal of Physics: Condensed Matter*, vol. 24, no. 33, p. 335301, 2012.

[191] D. Lide, *CRC Handbook of Chemistry and Physics, 89th Edition.* CRC Handbook of Chemistry and Physics, Taylor & Francis, 2003.

[192] J. S. Lee, J.-W. Park, J. Y. Song, and J. Kim, "Asymmetric magnetoconductance and magneto-Coulomb effect in a carbon nanotube single electron transistor," *Nanotechnology*, vol. 24, no. 19, p. 195201, 2013.

[193] J. T. Smith, A. D. Franklin, D. B. Farmer, and C. D. Dimitrakopoulus, "Reducing Contact Resistance in Graphene Devices through Contact Area Patterning," *ACS Nano*, vol. 7, no. 4, pp. 3361–3667, 2013.

[194] W. Han, K. Pi, W. Bao, K. M. McCreary, Y. Li, W. H. Wang, C. N. Lau, and R. K. Kawakami, "Electrical detection of spin precession in single layer graphene spin valves with transparent contacts," *Applied Physics Letters*, vol. 94, p. 222109, 2009.

[195] S. Jo, D. K. Ki, D. Jeong, H. J. Lee, and S. Kettemann, "Spin relaxation properties in graphene due to its linear dispersion," *Physical Review B*, vol. 84, p. 075453, 2011.

[196] T. K. T. Otani and J. Hamrle, "Enhancement of spin accumulation in a non-magnetic layer by reducing junction size," *Physical Review B*, vol. 73, p. 132405, 2006.

[197] D. H. Damon, C. R. Martin, and R. C. Miller, "Evidence for the Existence of Overlapping Valence and Conduction Bands in SnTe," *Journal of Applied Physics*, vol. 34, p. 3083, 1963.

[198] J. R. Dixon and R. F. Bis, "Band Inversion and the Electrical Properties of $Pb_x Sn_{1-x} Te$," *Physical Review*, vol. 176, no. 3, pp. 942–949, 1968.

[199] M. Safdar, Q. Wang, M. Mirza, Z. Wang, K. Xu, and J. He, "Topological Surface Transport Properties of Single-Crystalline SnTe Nanowire," *Nano Letters*, vol. 13, no. 11, pp. 5344–5349, 2013. PMID: 24175637.

[200] J. Shen, Y. Jung, A. S. Disa, F. J. Walker, C. H. Ahn, and J. J. Cha, "Synthesis of SnTe Nanoplates with (100) and (111) Surfaces," *Nano Letters*, vol. 14, no. 7, pp. 4183–4188, 2014. PMID: 24910959.

[201] B. A. Assaf, F. Katmis, P. Wei, B. Satpati, Z. Zhang, S. P. Bennett, V. G. Harris, J. S. Moodera, and D. Heiman, "Quantum coherent transport in SnTe topological crystalline insulator thin films," *Applied Physics Letters*, vol. 105, p. 102108, 2014.

[202] J. Shen, Y. Xie, and J. J. Cha, "Revealing Surface States in In-Doped SnTe Nanoplates with Low Bulk Mobility," *Nano Letters*, vol. 15, no. 6, pp. 3827–3832, 2015.

[203] Y. Tanaka, T. Shoman, K. Nakayama, S. Souma, T. Sato, T. Takahashi, M. Novak, K. Segawa, and Y. Ando, "Two types of Dirac-cone surface states on the (111) surface of the topological crystalline insulator SnTe," *Physical Review B*, vol. 88, p. 235126, Dec 2013.

[204] J. R. Burke, R. S. Allgaier, B. B. Houston, J. Babiskin, and P. G. Siebenmann, "Shubnikov-de Haas Effect in SnTe," *Phys. Rev. Lett.*, vol. 14, pp. 360–361, Mar 1965.

[205] M. Hilke, M. Massicotte, E. Whiteway, and V. Yu, "Weak Localization in Graphene: Theory, Simulations, and Experiments," *The Scientific World Journal*, vol. 2014, no. 737296, pp. 1–8, 2014.

[206] A. Spiesser, S. Sharma, H. Saito, R. Jansen, S. Yuasa, and K. Ando, "Electrical spin injection in p-type Si using Fe/Mgo contacts," *Proceeding SPIE*, vol. 8461, pp. 84610K–84610K–9, 2012.

Bibliography

[207] C. Józsa, T. Maassen, M. Popinciuc, P. J. Zomer, A. Veligura, H. T. Jonkman, and B. J. van Wees, "Linear scaling between momentum and spin scattering in graphene," *Phys. Rev. B*, vol. 80, p. 241403, Dec 2009.

[208] R. Farghadan and E. Saievar-Iranizad, "Spin-polarized transport in zigzag-edge graphene nanoribbon junctions," *Journal of Applied Physics*, vol. 111, no. 1, 2012.

[209] A. Saffarzadeh and R. Farghadan, "A spin-filter device based on armchair graphene nanoribbons," *Applied Physics Letters*, vol. 98, no. 2, 2011.

[210] F. Oberhuber, S. Blien, S. Heydrich, F. Yaghobian, T. Korn, C. Schüller, C. Strunk, D. Weiss, and J. Eroms, "Weak localization and Raman study of anisotropically etched graphene antidots," *Applied Physics Letters*, vol. 103, no. 14, 2013.

[211] J. Cai, P. Ruffieux, R. Jaafar, M. Bieri, T. Braun, S. Blankenburg, M. Muoth, A. P. Seitsonen, M. Saleh, X. Feng, K. Mullen, and R. Fasel, "Atomically precise bottom-up fabrication of graphene nanoribbons," *Nature*, vol. 466, pp. 470–473, July 2010.

[212] Y. Tanaka, T. Sato, K. Nakayama, S. Souma, T. Takahashi, Z. Ren, M. Novak, K. Segawa, and Y. Ando, "Tunability of the k-space location of the Dirac cones in the topological crystalline insulator $Pb_{1-x}Sn_xTe$," *Physical Review B*, vol. 87, no. 15, p. 155105, 2013.
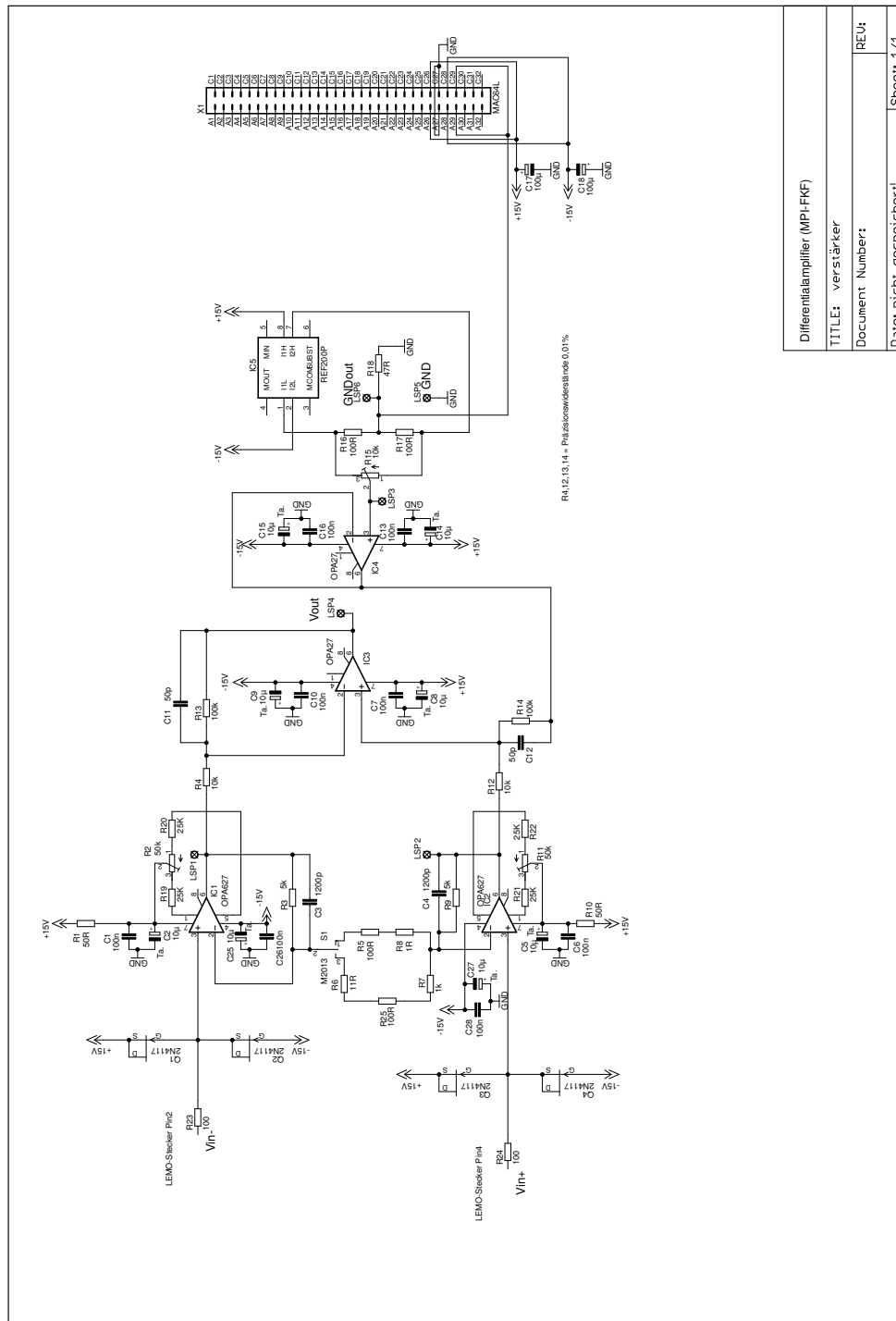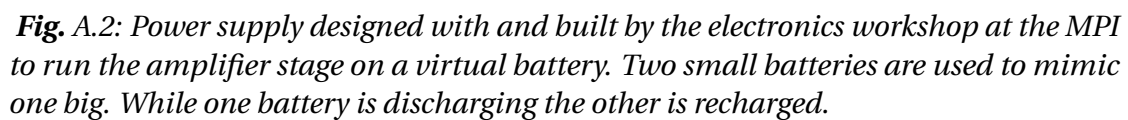
A Appendix

Fig. A.1: Schematics of the home build high impedance differential amplifier plug-in board to go with the amplifier stage from JÜLICH. *Entrances are protected by diodes to prevent voltage shocks to the Op-amps. Amplification can be changed between 10/100/1000 by a toggle switch. Information was obtained from the technical data sheets of the Op-amps from Ti [3].*

Fig. A.2: Power supply designed with and built by the electronics workshop at the MPI to run the amplifier stage on a virtual battery. Two small batteries are used to mimic one big. While one battery is discharging the other is recharged.

Publications

- P. Gehring; K. Vaklinova; A. Hoyer; H. M. Benia; V. Skakalova; G. Argentero; F. Eder; J. C. Meyer; M. Burghard; K. Kern
  Dimensional crossover in the quantum transport behaviour of the natural topological insulator Aleksite
  Scientific Reports **5**, 11691 (2015); doi:10.1038/srep11691
- C. Cervetti; E. Heintze; B. Gorshunov; E. Zhukova; S. Lobanov; A. Hoyer; M. Burghard; K. Kern; M. Dressel; L. Bogani
  Sub-Terahertz Frequency-Domain Spectroscopy Reveals Single-Grain Mobility and Scatter Influence of Large-Area Graphene
  Advanced Materials **27** (16), 2635-2641 (2015);doi: 10.1002/adma.201500599
- R. Konnerth; C. Cervetti; A. Narita; X. Feng; K. Mullen; A. Hoyer; M. Burghard; K. Kern; M. Dressel; L. Bogani
  Tuning the deposition of molecular graphene nanoribbons by surface functionalization
  Nanoscale **7**, 12807-12811 (2015);doi: 10.1039/C4NR07378A
- K. Vaklinova; A. Hoyer; M. Burghard; K. Kern
  Topological insulator-based spin injection into graphene
  NanoLetters accepted; doi: 10.1021/acs.nanolett.6b00167
- Devender; P. Gehring; R. J. Mehta; A. Hoyer; A. Gaul; M. Burghard; T. Borca-Tasciuc; K. Kern; D. J. Singh; G. Ramanath
  Harnessing topological insulator features in bismuth chalcogenide to enhance thermoelectric properties via sulfur doping
  Advanced Materials accepted

Curriculum Vitae

Personal Information

Date of birth   25.08.1985
Place of birht   Dresden, Germany
Nationality   German
Children   three

Education

2012	**Research staff** at the Max-Planck Institute for Solid State Research Stuttgart, Germany, Nanoscale Science Department of Prof. Klaus Kern, Dr. Marko Burghard (Quantum Materials group)
	PhD student at the Ecole Polytechnique Federale de Lausanne, Switzerland
2011	**Master Thesis**
	Fehlerabschätzung bei der Messung von skalaren und restlichen dipolaren Kopplungen im ABX-Spinsystem
	Prof. Burkhard Luy, Institute für Organische Chemie, KIT
2009-2011	**Master of Science** in Chemistry
	Karlsruher Institut für Technologie, Karlsruhe, Germany
2009	**Bachelor Thesis**
	Synthese und Charakterisierung von Koordinationsverbindungen der Bis-(2H-isoindolyl)-azamethine
	Dr. Markus Hummert & Dr. Roland Gresser, Institut für Angewandte Photophysik, TU Dresden
2006-2009	**Bachelor of Science** in Chemistry
	Technical University of Dresden, Germany
Juli 2005	**Abitur** (university entrance diploma)
	Gymnasium Dresden-Plauen, Dresden, Germany